Granular materials can be encountered everywhere and are very important in industry. The first step in understanding these materials is normally to focus upon gravity and mechanical contact forces only. While this is a valid approximation when the particles are large, for smaller particles also the ambient air has a pronounced influence and must be taken into account. In this thesis we focus on particles where the "Stokesian" forces (drag, air pressure) and the "Newtonian" forces (from collisions and gravity) compete for dominance. Two examples that illustrate this in a particularly clear manner are the formation and coarsening of Faraday heaps (see pictures below) and the appearance of Chladni patterns on a resonating plate (see front cover): When the Newtonian forces dominate the particles accumulate at the nodal lines (left column), whereas when the Stokesian forces dominate they move to the anti-nodes (right column).

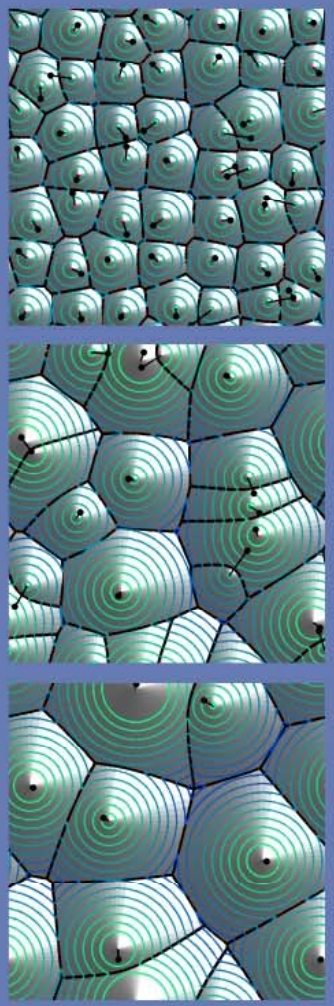

ISBN: 978-90-365-2800-9 (2009)

NEWTON VS STOKES: COMPETING FORCES IN GRANULAR MATTER

HENK JAN VAN GERNER

# NEWTON VS STOKES: COMPETING FORCES IN GRANULAR MATTER

HENK JAN VAN GERNER

# NEWTON VS STOKES:

## COMPETING FORCES IN GRANULAR MATTER

**Samenstelling promotiecommissie**

| | |
|---|---|
| Prof. dr. ir. L. van Wijngaarden, voorzitter | Universiteit Twente |
| Prof. dr. ir. J.A.M Kuipers, promotor | Universiteit Twente |
| Prof. dr. J.P. van der Weele, promotor | University of Patras |
| Dr. ir. M.A. van der Hoef, assistent-promotor | Universiteit Twente |
| Dr. R.M. van der Meer, assistent-promotor | Universiteit Twente |
| Prof. dr. M. van Hecke | Universiteit Leiden |
| Prof. dr. H.-J. Stöckmann | Universität Marburg |
| Dr. ir. R. Hagmeijer | Universiteit Twente |
| Prof. dr. rer. nat. S. Luding | Universiteit Twente |
| Prof. dr. rer. nat. D. Lohse | Universiteit Twente |

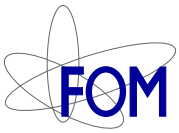


The work described in this thesis is part of the research program of the "Stichting voor Fundamenteel Onderzoek der Materie" (FOM), which is financially supported by the "Nederlandse Organisatie voor Wetenschappelijk Onderzoek" (NWO). It was carried out in the Physics of Fluids group and the Fundamentals of Chemical Reaction Engineering group, both at the Faculty of Science and Technology of the University of Twente.

Nederlandse titel:
*Newton vs Stokes — Concurrerende krachten in granulaire materie*

Publisher:
Henk Jan van Gerner,
Physics of Fluids group, Fundamentals of Chemical Reaction Engineering group,
University of Twente, P.O. Box 217, 7500 AE Enschede, The Netherlands

Cover design: Henk Jan van Gerner
Front cover illustration: Chladni patterning on a resonating plate, see chapter 5.
Back cover illustration: Coarsening of Faraday heaps, see chapter 4.
Print: Gildeprint B.V., Enschede



ISBN: 978-90-365-2800-9

# NEWTON VS STOKES:

## COMPETING FORCES IN GRANULAR MATTER

PROEFSCHRIFT

ter verkrijging van
de graad van doctor aan de Universiteit Twente,
op gezag van de rector magnificus,
prof. dr. H. Brinksma,
volgens besluit van het College voor Promoties
in het openbaar te verdedigen
op vrijdag 17 april 2009 om 15.00 uur

door

Henk Jan van Gerner

geboren op 2 juli 1977

te Harderwijk

Dit proefschrift is goedgekeurd door de promotoren:

Prof. dr. ir. J.A.M Kuipers
Prof. dr. J.P. van der Weele

en de assistent-promotoren:

Dr. ir. M.A. van der Hoef
Dr. R.M. van der Meer

# Contents

# 1 General introduction

*This thesis focuses on the behavior of vibrated granular matter when the effect of the ambient air is included. Granular matter is any material that consists of many grains, such as sand or flour. In many phenomena, the "Stokesian" forces (drag, air pressure) on the particles and the "Newtonian" forces (from collisions and gravity) compete for dominance, resulting in interesting collective behavior.*

## 1.1 Sir Isaac Newton and Sir George Gabriel Stokes

Sir Isaac Newton (1643-1727) was apart from one of the greatest physicists and mathematicians of all times, also an astronomer, natural philosopher,

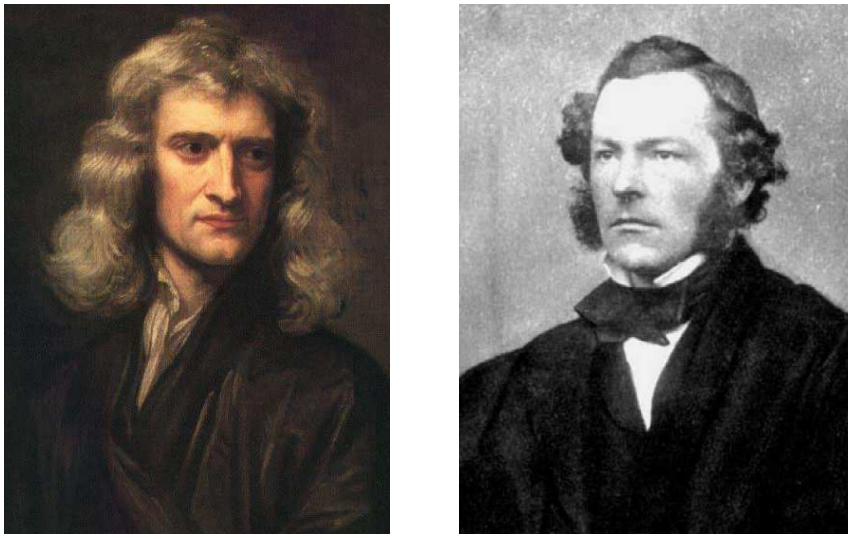

*Figure 1.1: Sir Isaac Newton and Sir George Gabriel Stokes.*

alchemist and theologian [1]. In June 1661, he was admitted to Trinity College, Cambridge. His Philosophiæ Naturalis Principia Mathematica, published in 1687, is considered to be the most influential book in the history of science. In this work, Newton described universal gravitation and the three laws of motion, laying the foundation for classical mechanics, which dominated the scientific view of the physical universe for the next three centuries and is the basis for modern engineering. Newton showed that the motions of objects on Earth and of celestial bodies are governed by the same set of natural laws. These laws also determine the motion of the particles in granular matter. For this reason, we refer to the forces on the particles from collisions and gravity as the "Newtonian" forces.

Sir George Gabriel Stokes, (1819-1903), was a mathematician and physicist, who at Cambridge made important contributions to fluid dynamics (including the Navier-Stokes equations), optics, and mathematical physics (including Stokes' theorem) [2]. In 1851, George Gabriel Stokes derived an expression, now known as Stokes' law, for the frictional force - also called drag force - exerted on spherical objects with very small Reynolds numbers (e.g., very small particles) in a viscous medium. For this reason, we refer to the forces that that are exerted on the particles by the ambient air as the "Stokesian" forces.

## 1.2 Granular matter

Granular materials can be encountered everywhere in everyday life, for example sand, sugar, or rice, and in natural processes such as avalanching and desert formation. Also in industry granular materials are abundant, since most raw materials are supplied in the form of grains, and a thorough understanding of granular matter is essential in order to efficiently handle these materials. Estimates are that we waste 40 % of the capacity of our industrial plants because of problems related to the transport of granular materials [3]. Producing homogeneous mixtures - very important in e.g. the pharmaceutical industry - is surprisingly difficult due to the tendency of granular materials to segregate [4–6].

The particles in granular matter interact with each other through dissipative contact forces; without an external driving their kinetic energy is rapidly lost. Depending on the amount of energy that is present in the system, granular matter can appear to behave like a solid, fluid or gas (see Fig. 1.2). However, granular matter exhibits phenomena that are not present in any of these familiar forms of matter (see Fig. 1.3), and should

*Figure 1.2: Granular matter can behave like either a solid (sand castle), a liquid (hourglass), or a gas (sandstorm).*

therefore be considered an additional state of matter in its own right [7, 8].

A great deal of progress has been made in the last few decades in explaining the rich and complex behavior of granular matter. However, the recent boom of papers on the subject has dealt almost exclusively with systems in which the effect of the ambient air is ignored, assuming that the motion of the particles is governed by gravity and mechanical contact forces only. While this is a valid approximation when the particles are large (diameter > 1 mm), for smaller particles the air actually has a pronounced influence and must be taken into account.

In this thesis we focus on particles of intermediate size, where the "Stokesian" forces (drag, air pressure) and the "Newtonian" forces (from collisions and gravity) compete for dominance. Striking examples are Faraday heaping, where the Newtonian forces drive the particles outward while the Stokesian forces drive the particle to the center of the heap (see Fig. 3.6), and Chladni patterns, which are formed by the Newtonian forces while inverse Chladni patterns are formed by the Stokesian forces (see Fig. 5.2).

## 1.3 A guide through the thesis

In chapter 2, the numerical model to calculate the motion of all individual particles in the granular material is presented, together with the model for the calculation of the gas flow. In chapter 3, the numerical model is used to simulate the motion of particles on a vibrating *rigid* plate, resulting in - thanks to the ambient air - the Faraday heaps known from experiment.

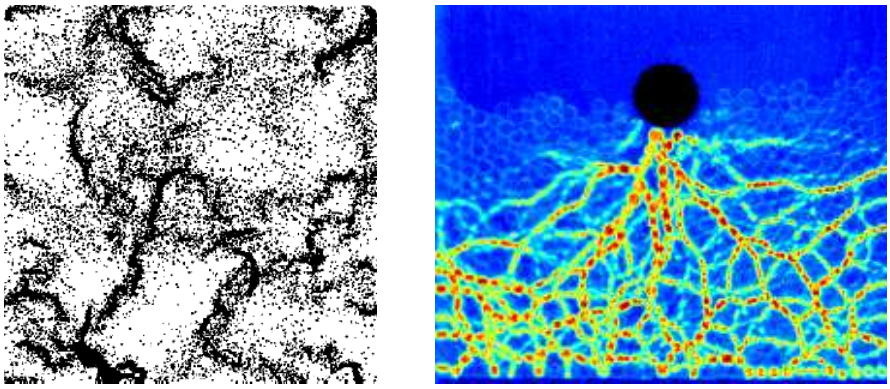

*Figure 1.3: Granular matter can appear to behave like a normal gas, fluid, or solid. However, it exhibits behavior not found in ordinary matter: In a granular gas, clusters of particles are spontaneously formed due to inelastic collisions [9]. In a granular liquid or solid, a load is not transmitted uniformly, but along a network of force chains, due to friction between the particles [10].*

These heaps merge into larger heaps on an ever increasing timescale and this coarsening behavior is studied in chapter 4.

In chapter 5, the motion of particles on a vibrating *flexible* plate is simulated, resulting in the famous Chladni patterns due to the Newtonian forces and inverse Chladni pattern due to the Stokesian forces. Surprisingly, the Newtonian forces can also form inverse Chladni patterns at very mild shaking conditions. This is discussed in chapter 6.

In chapter 7, the discharge of a granular fluid through an orifice is investigated. The outflow velocity is independent of the height of the granular column, even when the walls of the column are horizontally vibrated. Only when the wall induced shear rate is very high, the granular fluid behaves like an ordinary fluid.

The general conclusion of this thesis and an outlook for future work are provided in chapter 8.

## References

[1] R. S. Westfall, *The Life of Isaac Newton* (Cambridge Univ. Press, Cambridge, 1994). See also http://en.wikipedia.org/wiki/Isaac_Newton

[2] A very informative biographical sketch of George Gabriel Stokes can be found on http://en.wikipedia.org/wiki/George_Gabriel_Stokes

[3] T.M. Knowlton, G.E. Klinzing, W.C. Yang, J.W. Carson, *The importance of storage, transfer, and collection*, Chem. Eng. Prog. **90**, 44 (1994).

[4] A. Rosato, K.J. Strandburg, F. Prinz, and R.H. Swendsen, *Why the Brazil nuts are on top: Size segregation of particulate matter by shaking*, Phys. Rev. Lett. **58**, 1038 (1987).

[5] N. Burtally, P.J. King, and M.R. Swift, *Spontaneous Air-Driven Separation in Vertically Vibrated Fine Granular Mixtures*, Science **295**, 1877 (2002).

[6] C. Zeilstra, M.A. van der Hoef, and J.A.M. Kuipers, *Simulation study of air-induced segregation of equal-sized bronze and glass particles*, Phys. Rev. E **74**, 010302(R) (2006).

[7] H.M. Jaeger, S.R. Nagel, and R.P. Behringer, *Granular solids, liquids, and gases*, Rev. Mod. Phys. **68**, 1259 (1996).

[8] T. Shinbrot and F.J. Muzzio, *Nonequilibrium patterns in granular mixing and segregation*, Phys. Today **53**, 25 (2000).

[9] I. Goldhirsch and G. Zanetti, *Clustering instability in dissipative gases*, Phys. Rev. Lett. **70**, 1619 (1993).

[10] image taken from http://www.phy.duke.edu/research/cm/behringer/

# 2
# Numerical model

*In this chapter, the hybrid granular dynamics (GD)-computational fluid dynamics (CFD) code is presented that is used in the simulations described in the next chapters. The GD code calculates the trajectories of the spherical particles from Newton's law, with the particle-particle interactions being given by a 3D soft sphere collision model including tangential friction. The CFD code calculates the gas phase by evaluating the full Navier-Stokes equations by a finite difference method. The interaction between small particles and gas is two-way and handled via (empirical) drag relations. The interaction of large objects with the gas phase is implemented in two ways, via the cell cut method and the immersed boundary method (IBM). The immersed boundary method is validated with three different test cases, showing that IBM is a versatile and flexible method to fully resolve the flow around a large object.*

## 2.1 Introduction

In this research, we focus on systems of particles where the "Newtonian" (from collisions and gravity) and the "Stokesian" forces (drag, air pressure) compete for dominance. For this reason, an accurate model for the collision between the particles, the surrounding gas phase, and the particle-gas interaction is required.

Two types of collision model are widely used, namely the hard sphere model and the soft sphere model. The hard sphere model is event driven and allows only for binary, instantaneous collisions. The resulting particle velocities are obtained from an impulse balance, which can be solved analytically. The soft sphere model is time driven and multiple particle contacts are possible, where the particle velocities are calculated from contact forces via numerical integration. The hard sphere model is often

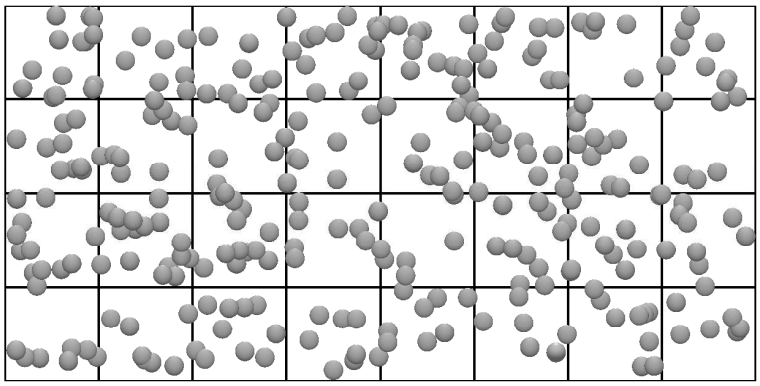

*Figure 2.1: Schematic representation of the unresolved flow method; the gas phase is solved on a computational mesh with a length scale larger than the size of the particles. The gas-particle interaction is calculated by an empirical model.*

used in dilute granular flows, but is less efficient when a dense region of particles impacts on a boundary. By contrast, the soft sphere model is less efficient in dilute granular systems but is very suitable for dense granular systems since multiple particle contacts are possible. Therefore, the soft sphere model is used in this research.

There are several options for the description of the gas phase in the presence of particles, but all of these can be traced back to two types, namely fully resolved and unresolved gas flow. For fully resolved flow (e.g., Lattice Boltzmann Simulations [1] or the Immersed Boundary methods [2]), the gas phase is solved on a length scale that is much smaller than the size of the particles. Fully resolved flow computations, however, are expensive from CPU and computer memory point of view and therefore the size of the systems that can be studied is limited to typically a few thousand particles on modern day computers. For unresolved flow, the gas phase is solved on length scales larger than the particles (see Fig. 2.1) and therefore the computational effort is much smaller. Since we are interested in systems larger than ten thousand particles, we use the unresolved gas flow. In that case, it is necessary to introduce empirical drag relations in order to take the gas-particle interaction into account.

The dynamics of large bodies present in the system (such as the moving boundary or intruder) is modelled fully resolved by either the IBM or cell cut method, which is described in section 2.6.

## 2.2 Equations of motion for the particles

The linear motion of a single spherical particle $a$ with mass $m_a$ and coordinate $\mathbf{r}_a$ can be described by Newton's equations:

$$m_a \frac{\mathrm{d}^2 \mathbf{r}_a}{\mathrm{d}t^2} = \mathbf{F}_{\mathrm{grav},a} + \mathbf{F}_{\mathrm{drag},a} + \mathbf{F}_{\nabla p,a} + \mathbf{F}_{\mathrm{contact},a} \ , \tag{2.1}$$

where $\mathbf{F}_{\mathrm{grav},a} = m_a \mathbf{g}$ is the gravitational force, $\mathbf{F}_{\mathrm{drag},i}$ is the gas drag force, and $\mathbf{F}_{\nabla p,a} = -V_a \nabla p$ is the force due to pressure gradients in the gas phase, with $V_a$ the volume of particle $a$. Furthermore, $\mathbf{F}_{\mathrm{contact},a}$ is the sum of the individual contact forces exerted by all other particles in contact with the particle $a$, which is divided into a normal and a tangential component:

$$\mathbf{F}_{\mathrm{contact},a} = \sum_{b \in \mathrm{contactlist}} \left( \mathbf{F}_{n,ab} + \mathbf{F}_{t,ab} \right) . \tag{2.2}$$

The rotational velocity of a particle is given by:

$$I_a \frac{\mathrm{d}\boldsymbol{\omega}_a}{\mathrm{d}t} = \mathbf{T}_a \ , \tag{2.3}$$

where $I_a = \frac{2}{5} m_a R_a^2$ is the moment of inertia (with $R_a$ the radius of particle $a$), $\boldsymbol{\omega}_a$ the angular velocity, and $\mathbf{T}_a$ the torque, which depends only on the tangential component of the individual contact forces:

$$\mathbf{T}_a = \sum_{b \in \mathrm{contactlist}} \left( R_a \mathbf{n}_{ab} \times \mathbf{F}_{t,ab} \right) , \tag{2.4}$$

where $\mathbf{n}_{ab}$ is the normal unit vector from particle $a$ to $b$.

We will next give a description of the normal and tangential component of the contact forces. The description of the force resulting from drag with the gas phase is given in section 2.4, whereas the dynamics of the gas phase itself is described in section 2.5.

## 2.3 Contact force

For the calculation of $\mathbf{F}_{n,ab}$ and $\mathbf{F}_{t,ab}$, we use a 3D linear spring/dashpot type of soft sphere collision model [3] along the lines of Cundall and Strack [4]. From this model, it follows that the force in the normal direction between two particles $a$ and $b$ which are in contact is equal to:

$$\mathbf{F}_{n,ab} = -k_n \delta_n \mathbf{n}_{ab} - \eta_n \mathbf{v}_{n,ab} \ , \tag{2.5}$$

where $k_n$ is the normal spring stiffness, $\delta_n$ the normal overlap between the particles, $\eta_n$ the normal damping coefficient, and $\mathbf{v}_{ab,n}$ the velocity difference in the normal direction. The force in the tangential direction has a similar form

$$\mathbf{F}_{t,ab} = -k_t \delta_t \mathbf{t}_{ab} - \eta_t \mathbf{v}_{t,ab} \ , \tag{2.6}$$

where the variables have the same meaning as in Eq. (2.5), but now for the tangential direction. Equation (2.6) is only valid when $|\mathbf{F}_{t,ab}| \leq \mu_{pp} |\mathbf{F}_{n,ab}|$, where $\mu_{pp}$ is the Coulomb friction coefficient of particle-particle contact. If the tangential force is larger, then frictional sliding occurs, resulting in a force

$$\mathbf{F}_{t,ab} = -\mu_{pp} |\mathbf{F}_{n,ab}| \, \mathbf{t}_{ab} \ . \tag{2.7}$$

### 2.3.1 Collision parameters

In order to solve Eqns. (2.5) and (2.6)/(2.7), we have to specify five parameters: the normal and tangential spring stiffness $k_n$ and $k_t$, the friction coefficient $\mu_{pp}$, and the normal and tangential damping coefficients $\eta_n$ and $\eta_t$. However, instead of specifying the normal and tangential damping coefficients, it is more convenient to specify the coefficients of normal and tangential restitution $e_n$ and $e_t$, which are defined as the relative velocity of two colliding particles after the collision divided by the velocity before the collision. These restitution coefficients determine the amount of energy that is lost in a collision, independent of the mass and spring stiffness of a particle. The values for the damping coefficients can be calculated from the restitution coefficients, the spring stiffness and the mass of the particles taking part in the collision [3].

In principle, $k_n$ and $k_t$ are related to the Young modulus and Poisson ratio of the solid material; however, in practice their value must be chosen much smaller, otherwise the time step of the integration needs to become impractically small. Therefore, the spring stiffness is chosen as low as possible while ensuring that using a different spring stiffness does not have a significant influence on the phenomena observed. In practice, the maximum overlap between the particles must be smaller than 5 %. The values for $k_n$ and $k_t$ are thus mainly determined by computational efficiency and not by the material properties. So, finally we are left with three collision parameters $e_n$, $e_t$ and $\mu_{pp}$. The precise values for these parameters can vary drastically and experimental data are scarce in the literature. For this reason, the influence of varying the values of the parameters is investigated for all the cases discussed in this thesis.

## 2.4 Air drag force

An empirical relation has to be used for the gas drag force $\mathbf{F}_{\mathrm{drag},a}$ on a particle in the presence of neighboring particles. It is convenient to write these relations in terms of the drag force on a single particle at low Reynolds number (the Stokes drag), multiplied by a correction function F to account for higher Reynolds number and the presence of neighboring particles:

$$\mathbf{F}_{\mathrm{drag},a} = 6\pi\mu_g R_a \left(\mathbf{u} - \mathbf{v}_a\right) \cdot \mathrm{F}(\mathrm{Re},\varepsilon) \,, \tag{2.8}$$

where $\mu_g$ is the dynamic gas viscosity and $\mathbf{u}$ is the local flow velocity of the gas phase. A widely used relation for the function F are the Ergun [5] and Wen&Yu [6] correlations:

$$\mathrm{F}(\mathrm{Re},\varepsilon) = \begin{cases} \varepsilon^{-2.65} \left(1 + 0.15\,\mathrm{Re}^{0.687}\right) & \text{for} \quad \varepsilon > 0.8 \\ \dfrac{150}{18}\dfrac{1-\varepsilon}{\varepsilon} + \dfrac{1.75}{18}\dfrac{\mathrm{Re}}{\varepsilon} & \text{for} \quad \varepsilon < 0.8 \end{cases} \tag{2.9}$$

where $\mathrm{Re} = 2R_a\rho_g\varepsilon\left|\mathbf{u} - \mathbf{v}_a\right| / \mu_g$ is the particle Reynolds number, with $\rho_g$ the density of the gas phase and $\varepsilon$ the local volume fraction of the gas phase. The local flow velocity, volume fraction and density of the gas phase are obtained by a linear (volume weighting) interpolation from the nearest eight nodes of the computational mesh for the gas phase.

More recently, improved drag relations, obtained from fully resolved simulations such as the Lattice Boltzmann Model have been proposed, such as the correlation by Beetstra *et al.* [1]:

$$\begin{aligned} \mathrm{F}(\mathrm{Re},\varepsilon) \;=\; & \frac{10\,(1-\varepsilon)}{\varepsilon} \;+\; \varepsilon^3 \left(1 + 1.5\,(1-\varepsilon)^{1/2}\right) \\ & + \frac{0.413\,\mathrm{Re}}{24\varepsilon} \left[\frac{\varepsilon^{-1} + 3\varepsilon(1-\varepsilon) + 8.4\,\mathrm{Re}^{-0.343}}{1 + 10^{3(1-\varepsilon)}\mathrm{Re}^{-(1+4(1-\varepsilon))/2}}\right] . \end{aligned} \tag{2.10}$$

This correlation can also be extended to include for the effect of polydispersity. However, such systems are not considered in this thesis.

## 2.5 Governing equations for the gas phase

The gas flow is governed by the conservation equations for mass and momentum:

$$\frac{\partial\left(\varepsilon\rho_g\right)}{\partial t} + \nabla\cdot\varepsilon\rho_g\mathbf{u} = 0 \,, \tag{2.11}$$

$$\frac{\partial\left(\varepsilon\rho_g\mathbf{u}\right)}{\partial t}+\nabla\cdot\varepsilon\rho_g\mathbf{u}\mathbf{u}=-\varepsilon\nabla p-\mathbf{s}_p-\nabla\cdot\varepsilon\boldsymbol{\tau}+\varepsilon\rho_g\mathbf{g}+\mathbf{s}_{\mathrm{ibm}}\ , \tag{2.12}$$

where $p$ is the gas phase pressure, $\boldsymbol{\tau}$ the viscous stress tensor, $\mathbf{s}_{\mathrm{ibm}}$ the source term for the momentum exchange with large bodies (discussed in section 2.6.2), and $\mathbf{s}_p$ a source term that describes the momentum exchange with the solid particles:

$$\mathbf{s}_p=\sum_{a=1}^{N_{part}}\mathbf{F}_{\mathrm{drag},a}\delta\left(\mathbf{r}-\mathbf{r}_a\right)\ , \tag{2.13}$$

where the summation is over all particles and the drag force $\mathbf{F}_{\mathrm{drag},a}$ is identical to what is used in the equation of motion of the particles (Eq. 2.1). The gas phase density $\rho_g$ is calculated from the ideal gas law:

$$\rho_g=\frac{pM_g}{RT}\ , \tag{2.14}$$

with $M_g$ the molecular mass of the gas, $R$ the universal gas constant (8.314 J/(mol.K)) and $T$ the temperature.

Note that no turbulence modelling is taken into account. For dense granular beds, this can be justified since the turbulence is completely suppressed in the particle bed due to the high volume fraction of the solid phase.

### 2.5.1 Discretization of gas phase equations

A first-order-accurate semi-implicit method is used to discretize the momentum equations in time. The pressure and the particle force contribution are treated implicitly, while the viscosity and convection contribution are treated explicitly. In Eq. (2.8) we observe that the particle drag contribution can be split into a part proportional to $\mathbf{u}$ and a part proportional to the particle velocity $\mathbf{v}_a$. We therefore write $\mathbf{s}_p$ as $\beta\mathbf{u}-\alpha$. With this, we write Eq. (2.11) as:

$$\frac{\partial\left(\varepsilon\rho_g\mathbf{u}\right)}{\partial t}=-\left[\varepsilon\nabla p+\beta\mathbf{u}\right]-\left[\nabla\cdot\varepsilon\rho_g\mathbf{u}\mathbf{u}+\nabla\cdot\varepsilon\boldsymbol{\tau}-\alpha-\varepsilon\rho_g\mathbf{g}-\mathbf{s}_{\mathrm{ibm}}\right]\ . \tag{2.15}$$

We now discretize this equation in time*:

$$\left[\varepsilon\rho_g\mathbf{u}\right]^{n+1}=-\Delta t\left[\varepsilon\nabla p\right]^{n+1}-\Delta t\beta^n\mathbf{u}^{n+1}+A^n+\Delta t\mathbf{s}_{\mathrm{ibm}}^n\ , \tag{2.16}$$

*The porosity $\varepsilon$ only depends on the particle positions. $\varepsilon^{n+1}$ is therefore available explicitly by using the latest available particle positions. This data is stored to become $\varepsilon^n$ in the next time step. The latest available particle velocities $\mathbf{v}_a$ are used for $\alpha^n$

with

$$A^n = [\varepsilon\rho_g \mathbf{u}]^n - \Delta t[\nabla \cdot \varepsilon\rho_g \mathbf{u}\mathbf{u} + \nabla \cdot \varepsilon\boldsymbol{\tau} - \alpha - \varepsilon\rho_g \mathbf{g}]^n \ . \tag{2.17}$$

The time step $\Delta t$ for the flow solver can be taken larger than the time step required for the integration of the equations of motion of the particles. We now collect $\mathbf{u}^{n+1}$ at the LHS of the equation, yielding the final expression for the velocity:

$$\mathbf{u}^{n+1} = \frac{-\Delta t[\varepsilon\nabla p]^{n+1} + A^n + \Delta t \mathbf{s}^n_{\mathrm{ibm}}}{[\varepsilon\rho_g]^{n+1} + \Delta t\beta^n} \ , \tag{2.18}$$

The velocity and density can be substituted in the discretized continuity equation:

$$\frac{[\varepsilon\rho_g]^{n+1} - [\varepsilon\rho_g]^n}{\Delta t} + [\nabla \cdot \varepsilon\rho_g \mathbf{u}]^{n+1} = D \ , \tag{2.19}$$

where $D$ is the mass deficit which should be zero. Naturally, $\nabla p^{n+1}$ and $\rho_g^{n+1}$ (related to $\nabla p^{n+1}$ by Eq. (2.14)) in Eq. (2.18) are not explicitly available. We therefore resort to an iterative procedure at each time level which goes as follows (see also Fig. 2.2);

- Solve Eq. (2.18) using an initial estimated value $p^*$ for the pressure at time level $n+1$,
- Calculate the mass deficit $D$ with Eq. (2.19),
- If the mass deficit $D$ is not sufficiently close to zero, we use this value to calculate a new estimation for the pressure $p^*_{new}$ and return to the first item.

The new value for $p^*_{new}$ is $p^* + \delta p$, where $\delta p$ is obtained from a Taylor expansion of the mass deficit $D$;

$$D(p^*_{new}) = D(p^* + \delta p) = D(p^*) + \frac{\mathrm{d}D}{\mathrm{d}p^*}\delta p + O(\delta p^2) \ . \tag{2.20}$$

Neglecting higher order terms and taking the desired mass deficit $D(p^*_{new})$ to be zero, this can be written as:

$$J\delta p = -D(p^*) \ , \text{ with } J = \frac{\mathrm{d}D}{\mathrm{d}p^*} \tag{2.21}$$

Due to the spatial discretization of the Navier Stokes equations, $p^*$ and $D$ are vectors with length $NX \times NY \times NZ$ and the Jacobian $J$ is a square

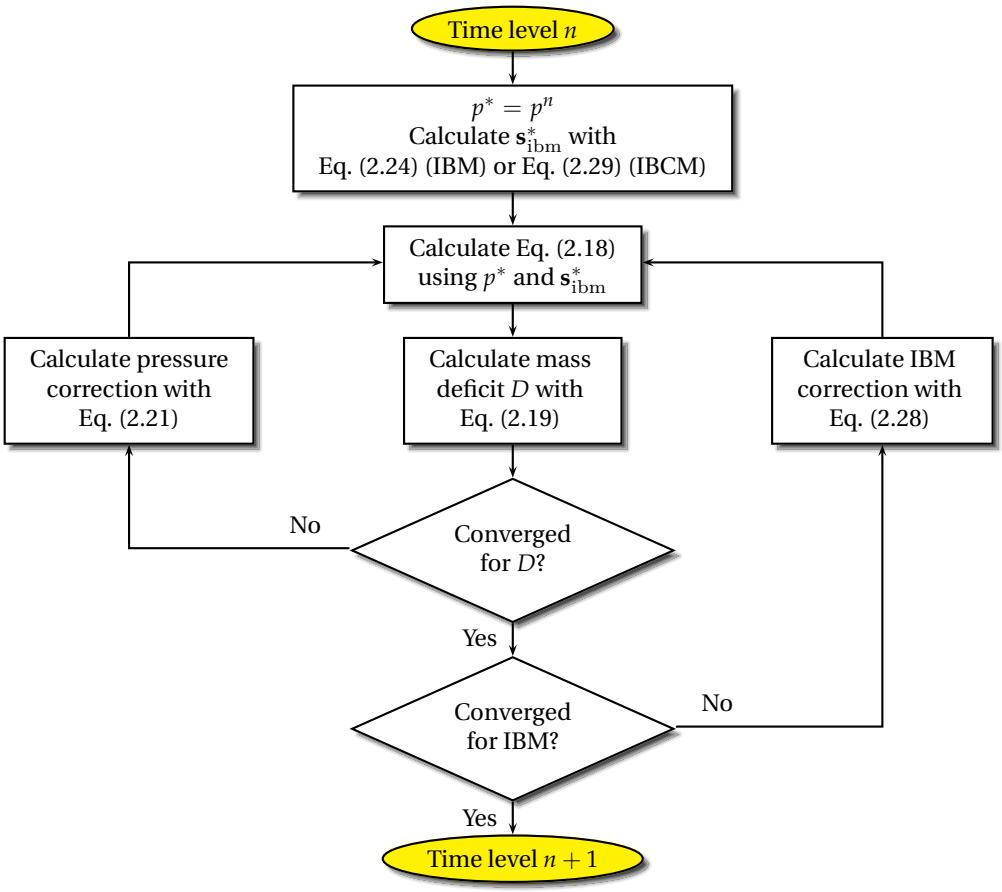


*Figure 2.2: Flow chart for the flow solver including the IBM iteration procedure.*

sparse matrix. The solution for the vector $\delta p$ is found by applying an ICCG sparse matrix solver. In principle, the matrix $J$ must be built at each iteration. However, since it only changes a little, the matrix $J$ is only constructed at the first iteration step.

A staggered Cartesian 3D grid is used for the spatial discretization. The scalar variables ($p$, $\rho_g$, and $\varepsilon$) are defined at the cell center, whereas the velocity components are defined at the cell faces. The convective terms in $A^n$ are computed using a second order flux delimited Barton scheme [8, 9], where the viscous and pressure terms are calculated by a central difference representation.

## 2.6 Interaction with large bodies

The interaction of the gas phase with an intruder larger than the size of the CFD cells is modelled with the immersed boundary method (IBM). The interaction of the gas phase with a vibrating boundary is modelled by either the cell cut method or the immersed boundary method, which are discussed in the next sections.

### 2.6.1 The cell cut method

The cell cut method was developed by Zeilstra [10]. In this method, the vibrating boundary moves through a fixed computational grid for the gas phase. This means that computational cells are 'cut' by the vibrating boundary. The movement of the boundary changes the volume available for the gas in the Cartesian cells, generating the wall-induced gas flow in a natural way. When the vibration amplitude of a boundary is larger than the size of the cells, computational cells can even find themselves outside the computational domain. A detailed description of the method is provided by Zeilstra [10]. To allow for simulations with a *resonating* plate (see chapter 5), the method has been modified in order to be able to model curved vibrating walls instead of rigid horizontal walls. A disadvantage of the method is that computational cells can become very small, which can lead to numerical instability of the flow solver.

An alternative, more flexible method to model the interaction with large bodies is provided by the immersed boundary method, which is described in the next section.

### 2.6.2 The immersed boundary method

The immersed boundary method (IBM) makes use of a fixed Eulerian grid to solve for the flow field of the gas phase and Lagrangian marker points situated on the boundary or large immersed body (see Fig. 2.3). Each marker exerts a force on the gas phase such that the local velocity of the gas is equal to the velocity of that marker. IBM has been widely used to study fluid-structure interaction and was pioneered by Peskin [11] to investigate cardiac flow problems. Subsequently, the method has been extended to the flow around rigid bodies. The implementation that we adopt is along the lines of Uhlmann [2]. The force term $\mathbf{s}_{\mathrm{ibm}}$, which gives the desired velocity $\mathbf{u}^d$ at time level $n+1$, can be derived simply from

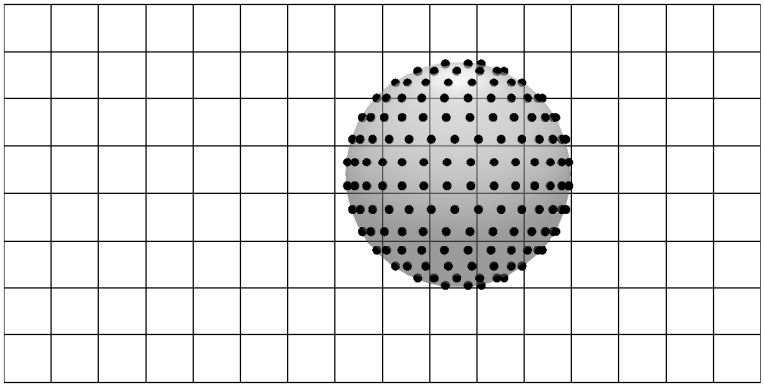

*Figure 2.3: Schematic representation of the IBM method; the gas phase is solved on an Eulerian mesh with a length scale smaller than the size of an intruder. Lagrangian markers (or force points) are located on the surface of the intruder.*

rearranging Eq. (2.16):

$$\Delta t \mathbf{s}_{\mathrm{ibm}}^{n} = \left([\varepsilon\rho_g]^{n+1} + \Delta t\beta^n\right)\mathbf{u}^d + \Delta t[\varepsilon\nabla p]^{n+1} - A^n \ . \tag{2.22}$$

We now introduce a preliminary velocity without applying a force term[†]:

$$\mathbf{u}^p = \frac{-\Delta t\varepsilon^{n+1}\nabla p^n + A^n}{\varepsilon^{n+1}\rho_g^n + \Delta t\beta^n} \ , \tag{2.23}$$

If we take the values for the pressure and density at time level $n$ instead of $n+1$ in Eq. (2.22), we can replace the last two terms in this equation by the preliminary velocity times $(\varepsilon^{n+1}\rho_g^n + \Delta t\beta^n)$ :

$$\Delta t \mathbf{s}_{\mathrm{ibm}}^{n} = (\varepsilon^{n+1}\rho_g^n + \Delta t\beta^n)(\mathbf{u}^d - \mathbf{u}^p) \ , \tag{2.24}$$

i.e., the IBM force source term is proportional to the difference between the desired velocity and the velocity of the fluid without any IBM forcing term. We now evaluate this IBM force term at the Lagrangian force points. The source term is calculated by summing the contribution of all Lagrangian force points:

$$\mathbf{s}_{\mathrm{ibm}}^{n} = \sum_{a=1}^{N_{\mathrm{langr}}} \mathbf{F}_{\mathrm{langr},a}\delta\left(\mathbf{r} - \mathbf{r}_a\right) \ . \tag{2.25}$$

[†]We calculate this preliminary velocity in the flow solver using Eq. (2.18), where the IBM force term is omitted and the pressure and density at time level $n$ are used.

The contribution of each Lagrangian force point to the IBM source term is then simply:

$$\mathbf{F}_{\text{langr},a} = n(\text{EP} + \Delta t\text{B})(\mathbf{U}^d - \mathbf{U}^p) \ , \tag{2.26}$$

where E, P, B, $\mathbf{U}^d$, and $\mathbf{U}^p$ are the gas volume fraction, gas density, $\beta$, desired gas velocity, and preliminary velocity at the Lagrangian force point and $n$ is a normalization factor. The values for E, P, B, and $\mathbf{U}^p$ are obtained by a linear (volume weighting) or a $4^{th}$ order polynomial interpolation [12] from the neighboring Eulerian gas phase cells. $\mathbf{U}^d$ is simply the velocity of the Lagrangian force point. The force of each Lagrangian force point is distributed to the nearest-neighboring Eulerian flow cell again by either a linear (volume weighting) or a $4^{th}$ order polynomial interpolation.

To each force point, a volume can be assigned signifying its range of influence. The normalization factor $n$ is then the volume per force point divided by the total volume of a CFD cell. For a flat surface, and cubic CFD elements, $n$ is simply $1/N_{\text{fp}}$, with $N_{\text{fp}}$ the number of force points on the surface per CFD cell. For a sphere, the range of influence of the force points perpendicular to the surface is equal to the typical height $h$ of a CFD cell. The factor $n$ for a sphere is then the surface area of the sphere times the typical height $h$ of a CFD cell, divided by the volume of a CFD cell and the total number of force points on the sphere:

$$n = \frac{4\pi R^2 h}{h^3 N_{\text{langr}}} \ , \tag{2.27}$$

where $h$ is $\sqrt[3]{\Delta x \Delta y \Delta z}$. If the factor $n$ is taken to be constant, it is important that the force points are distributed uniformly over the surface. For a flat surface, this is straightforward. However, for a sphere there is no analytical expression to distribute the force points uniformly over the surface, so we have to resort to approximate methods to distribute the force points over the surface. Small deviations in the calculated flow field can occur due to a slight heterogeneity in the distribution of the force points, however, this has no significant influence on our results (see Fig. 2.8). For arbitrary shaped surfaces, the factor $n$ can usually not be treated as a constant but becomes a function of the location. The iteration procedure described below can be used to decrease the difference between the desired and the actual velocity of the gas phase when the factor $n$ is not chosen entirely correctly.

Although the difference in the obtained flow velocity and the desired velocity $\mathbf{u}^d$ can be made smaller by decreasing the value of the time step, it is sometimes convenient to correct the IBM force such that

the difference becomes small while using a relative large time step. The most straightforward implementation is that the IBM force can be corrected using the difference between the obtained and desired velocity: $\mathbf{s}^*_{\text{ibm, new}} = \mathbf{s}^*_{\text{ibm}} + \delta\mathbf{s}_{\text{ibm}}$, with:

$$\delta\mathbf{s}_{\text{ibm}} = \frac{(\varepsilon^{n+1}\rho^*_g + \Delta t\beta^n)(\mathbf{u}^d - \mathbf{u}^*)}{\Delta t} , \tag{2.28}$$

where $\mathbf{u}^*$ and $\rho^*_g$ indicate the flow velocity and density after a converged pressure correction. The correction force is evaluated at the Lagrangian force points as in Eqs. (2.25) and (2.26). The correction can be repeated until $\delta\mathbf{s}_{\text{ibm}}$ is sufficiently small. The correction could be multiplied by a factor smaller or larger than unity (i.e., under/over relaxation), but this is not further investigated. The flowchart of the semi-implicit method for the time discretization including the IBM iteration procedure is shown in Fig. 2.2.

### 2.6.3 The immersed boundary correction method

IBM is a versatile and flexible method to fully resolve the flow around a large object. However, it was found in a previous study [10] that very small time steps are required to resolve the flow around a large sphere which is pulled through a granular bed of small particles (see also section 2.6.6). The time step can be increased by using the iteration procedure discussed above. However, a relative large number of iterations must be employed to obtain a satisfying solution. Inspired by the IBM iteration procedure, we developed an immersed boundary method which does not calculate an entirely new IBM force each time step (Eq. 2.24), but a *correction* to the IBM force obtained in the previous time step:

$$\Delta t\mathbf{s}^n_{\text{ibm}} = \Delta t\mathbf{s}^n_{\text{ibm, old}} + (\varepsilon^{n+1}\rho^n_g + \Delta t\beta^n)(\mathbf{u}^d - \mathbf{u}^{p*}) , \tag{2.29}$$

where the preliminary velocity is calculated by:

$$\mathbf{u}^{p*} = \frac{-\Delta t\varepsilon^{n+1}\nabla p^n + A^n + \Delta t\mathbf{s}^n_{\text{ibm, old}}}{\varepsilon^{n+1}\rho^n_g + \Delta t\beta^n} = \mathbf{u}^p + \frac{\Delta t\mathbf{s}^n_{\text{ibm, old}}}{\varepsilon^{n+1}\rho^n_g + \Delta t\beta^n} , \tag{2.30}$$

i.e., $\mathbf{u}^{p*}$ is equal to $\mathbf{u}^p$ except that the IBM force term obtained in the previous time step is now included. The correction to the IBM force is evaluated at the Lagrangian force points as in Eqs. (2.25) and (2.26). Note that the IBM force term in the preliminary velocity appears to cancel with

$\mathbf{s}^n_{\text{ibm, old}}$ in Eq. (2.29), yielding the ordinary immersed boundary method. However, there is a difference between these two terms: The force correction is calculated by summing the contribution of all Lagrangian force points, which requires mapping from the Eulerian mesh to the Lagrangian markers and vice versa. The first term on the RHS in Eq. (2.29) is just the IBM forcing obtained in the previous time step and requires no mapping. When the gradient of the flow field variables perpendicular to the immersed boundary is large, for example due to the presence of particles, the immersed boundary *correction* method gives more accurate results than the immersed boundary method.

Since the immersed boundary correction method calculates a correction to the IBM force, the possibility arises that an IBM force is still present in an Eulerian cell, even when no Lagrangian force point is within the range of influence of this cell. For this reason, $\mathbf{s}^n_{\text{ibm, old}}$ is multiplied by a factor slightly smaller than unity before each time step. We use a factor of $m = \sigma^{|\mathbf{u}^d|\Delta t/h}$, with $\sigma$ a small number e.g. $1 \cdot 10^{-6}$. This guarantees that the IBM forcing only has one millionth of its original value when no correction is applied and the force points have shifted the typical distance of a CFD cell $h$. For the simulation of the air flow around a sphere (see Fig. 2.7), $\sigma = 1 \cdot 10^{-6}$ which results in $m = 0.983$. Using a different value for $\sigma$ does not give different results.

In order to assure that the implementation of the interaction with large bodies gives realistic results, it is necessary to first compare the obtained results for the flow field with analytical or verified experimental/numerical results for some well-defined systems. Three test cases are used for this validation:

- *A vertically vibrating box* - Containers with vertically vibrating rigid walls are used extensively in the research presented in this thesis (see chapters 3, 4, and 7). The velocity and the pressure gradient can be calculated analytically.
- *Flexible bottom plate* - The airflow between a flexible vibrating bottom plate and a rigid cover is a very interesting test case, since the vertical motion of the bottom plate results in both a vertical *and* horizontal airflow over the bottom plate. Furthermore, an analytical solution for the flow field can be derived. A vibrating flexible bottom plate is used in chapter 5.
- *Flow around a sphere* - The flow around a sphere is important if one

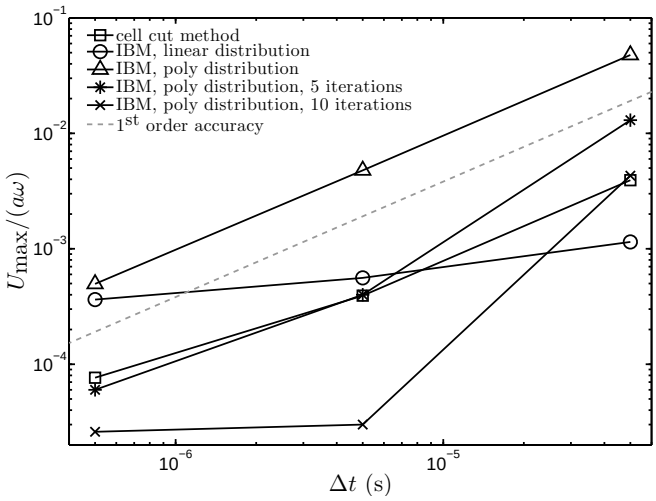


*Figure 2.4: Normalized maximum velocity in the box as a function of $\Delta t$. The cell cut method and the immersed boundary method with polynomial force distribution show an error proportional to the time step $\Delta t$, as expected from a $1^{st}$ order in time discretization scheme. The error obtained by IBM with linear distribution does not show a proportional decrease with $\Delta t$. The IBM iteration procedure can greatly reduce the error.*

investigates e.g. the role of air in granular jet formation [13] or the Brazil Nut effect [14] by numerical simulations. Experimentally obtained relations for the drag force on the sphere are widely available.

In the next sections, these three test cases are discussed in more detail. The immersed boundary correction method is only used for the flow around a sphere.

### 2.6.4 Vibrating box

We use a vibrating container with dimensions $5 \times 5 \times 50$ mm$^3$ which is divided in $5 \times 5 \times 20$ CFD cells ($W \times D \times H$)[‡]. The container is vibrated vertically using a sinusoidal driving with frequency $f = 25$ Hz and amplitude $a = 10$ mm (corresponding to a dimensionless acceleration $\Gamma = a\omega^2/g = 25$, with $\omega = 2\pi f$). We use both the cell cut method and

[‡]Using only one CFD cell in each horizontal direction would be sufficient, since there are no horizontal gradients. However, the minimum number of CFD cells in the numerical code is five in each direction.

the immersed boundary method to solve this test case. Note that for this simple test case, it is also possible to move the CFD cells with the vibrating box and simply add a source term of $\varepsilon\rho_g a\omega^2 \sin(\omega t)$ to the $z$-momentum equation. However, this is not implemented in the code. At $1/4^{\text{th}}$ and $3/4^{\text{th}}$ of a vibration cycle, the acceleration is at a maximum while the velocity of the box is zero. The velocity of the gas should therefore be zero everywhere in the container at these time instants[§]. For this reason, we compare the highest velocity of the gas phase in the box (normalized with $a\omega$) at $t = \frac{3}{4}/f$ s for a number of cases for different values of the time step $\Delta t$ (Fig. 2.4). When we use a linear (volume weighting) mapping between the Eulerian grid and the Lagrangian force points, we do not observe a first-order accurate in time behavior (circles in Fig. 2.4). This is most likely due to oscillatory behavior induced when an IBM force point moves to a next CFD cell. This is a well known phenomenon [11], and the conclusion is that this mapping method produces unsatisfactorily results in this case. By contrast, the $4^{th}$ order polynomial mapping [12] provides a smoother distribution of the forces when an IBM force point moves to a next CFD cell. We see indeed that in the case where this mapping is applied, first-order accurate in time behavior is obtained (i.e., the error is proportional to the time step, see triangles in Fig. 2.4). The IBM iteration procedure can greatly reduce the difference between the desired and obtained velocity, see the asterisks and crosses in Fig. 2.4.

### 2.6.5 Flexible bottom plate

We use a container with dimensions $150 \times 150 \times 5\,\text{mm}^3$ which is divided in $30 \times 30 \times 50$ CFD cells ($L \times L \times H$). For the top of the container, a no-slip boundary is used while periodic boundaries are used for all the vertical walls. The vertical position $z$ of the bottom plate at any point $(x, y)$ is given by:

$$z(x, y, t) = a \sin(\omega t) \sin \frac{2\pi x}{L} \sin \frac{2\pi y}{L} , \tag{2.31}$$

with $\omega = 2\pi f = 2\pi\ 200\ \text{rad/s}$ and $a = 2.5 \cdot 10^{-5}$ m (corresponding to a dimensionless acceleration $\Gamma = 4$). The horizontal velocity of the gas, averaged over the height $H$, can be evaluated analytically and is equal to

[§]This is only strictly true in the case of an incompressible fluid. However, the acceleration and velocity of the box are small so compressibility effects have a negligible influence on the velocity of the gas.

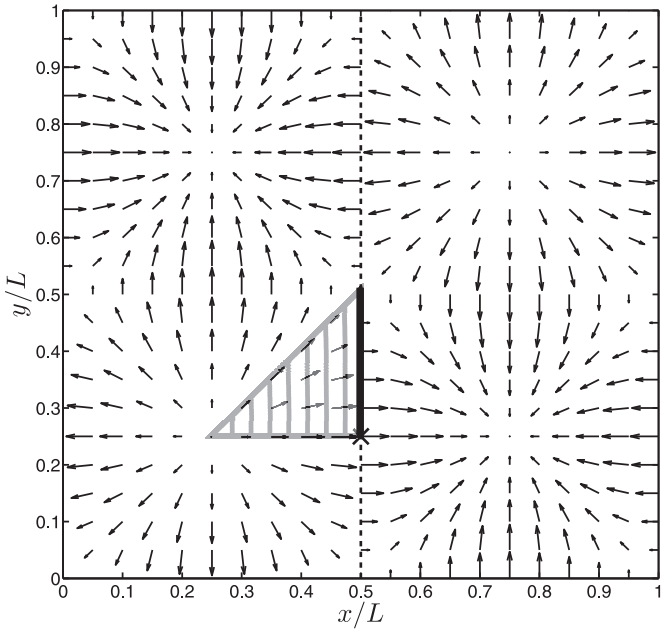


*Figure 2.5: Horizontal flow field at $t = \frac{1}{2}/f$ s over a vertically vibrating flexible bottom plate.*

(see Fig. 2.5):

$$\bar{u}_x = R\,a\omega\cos(\omega t)\cos\frac{2\pi x}{L}\sin\frac{2\pi y}{L}, \tag{2.32}$$

$$\bar{u}_y = R\,a\omega\cos(\omega t)\sin\frac{2\pi x}{L}\cos\frac{2\pi y}{L}\,, \tag{2.33}$$

where the amplitude $R$ has yet to be determined. This amplitude can be derived with a continuum and symmetry consideration: All the air that is displaced vertically by the resonating plate within the hatched area in Fig. 2.5, must flow horizontally through the area indicated by the thick black line:

$$\int_{L/4}^{x}\int_{L/4}^{L/2} a\omega\cos(\omega t)\sin\frac{2\pi x}{L}\sin\frac{2\pi y}{L}\mathrm{d}x\mathrm{d}y = \int_{L/4}^{L/2} h\,R\,a\omega\cos(\omega t)\sin\frac{2\pi y}{L}\mathrm{d}y\,, \tag{2.34}$$

which results in $R = L/(4\pi H)$. Figure 2.6(a) shows the analytical and simulated velocity $\bar{u}_x$ at $x = L/2$ (dashed line in Fig. 2.5). For the cell

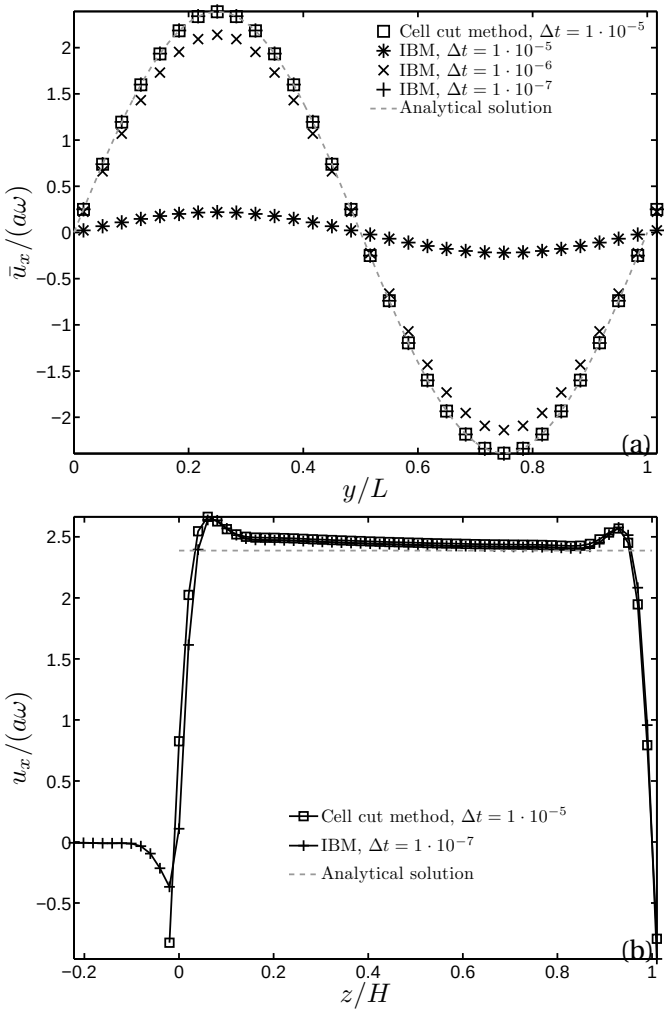


*Figure 2.6: (a) Analytical and simulated velocity $\bar{u}_x$ at $x = L/2$ (dashed line in Fig. 2.5). (b) Simulated velocity $u_x$ at $x = L/2$ and $y = L/4$ (indicated by the black X in Fig. 2.5). For both numerical methods, the no slip condition is used at the top and bottom boundary, resulting in a thin boundary layer. With IBM, the flow field is also calculated underneath the vibrating bottom plate, indicated by the plus markers located at $z < 0$.*

cut method, the agreement with the analytical solution is excellent. For the immersed boundary method, the agreement using a $\Delta t$ of $1 \cdot 10^{-5}$ s is very poor. Decreasing the time step to $1 \cdot 10^{-7}$ s greatly improves the agreement. However, a similar agreement can also be obtained by using a $\Delta t$ of $1 \cdot 10^{-6}$ s and 4 IBM iterations or a $\Delta t$ of $1 \cdot 10^{-5}$ s and 25 IBM iterations (not shown in Fig. 2.6). The simulated velocity $u_x$ as a function of $z$ at $x = L/2$ and $y = L/4$ (black X in Fig. 2.5) is shown in Fig. 2.6(b). For both numerical methods, the no slip condition is used at the top and bottom boundary, resulting in a thin boundary layer. With IBM, the flow field is also calculated in a small region underneath the vibrating bottom plate, indicated by the cross markers located at $z < 0$.

### 2.6.6 Flow around a sphere

The interaction between the interstitial air and granular systems with many small particles can be modelled accurately using empirical drag relations (see chapters 3 to 6). However, difficulties arise when the granular system consists of many small particles and a large sphere (an 'intruder'). Examples of such systems are granular jet formation, for which it has been shown that the height of the jet and the penetration depth of the intruder depend on the ambient air pressure [13], and the Brazil Nut effect, where the rise velocity of the intruder depends on the air pressure [14]. The difficulty in modelling such systems is that the size of the intruder is typically much larger than the size of the CFD cells (at least when the flow around the intruder has to be calculated accurately). For this reason, we use empirical drag relations for the interaction with the small particles, while the interaction of the gas with the large intruder is handled by the immersed boundary method.

For the test case, we use a container with dimensions $6 \times 6 \times 12$ $\mathrm{cm}^3$ ($W \times D \times H$). At the bottom of the container, the vertical air velocity is 0.19 m/s. A spherical intruder with a diameter $d_i$ of 10 mm is pulled through the container with a constant velocity[¶] of -0.05 m/s. The Reynolds number of the gas phase, calculated in a frame of reference where the intruder is static, is equal to $\mathrm{Re} = 160$. In some test cases, the container is also filled with 1.4 million spherical particles ($\rho = 2500$ kg/m$^3$) of average diameter 0.5 mm, with a Gaussian size distribution ($\sigma = 0.02$ mm) to avoid excessive ordering of the bed. The minimum fluidization velocity of these

[¶]A non-zero velocity for the intruder is used to investigate the effect of CFD cell transitions of the intruder.

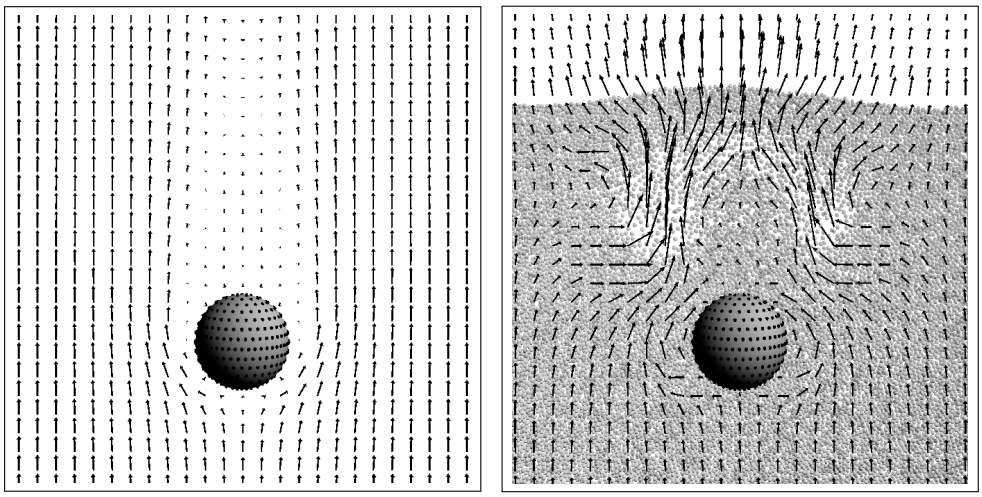

*Figure 2.7: Cross section of the gas velocities around a sphere that is pulled with a velocity of -0.05 m/s through a vertical gas flow of 0.19 m/s (resulting in a Reynolds number of Re=160 without particles). Both results are obtained with IBCM with* $\Delta t = 5 \cdot 10^{-5}$ *and only part of the container is shown. On the left hand side, no small particles are present, while on the right side, the container contains 1.4 million small particles. The black dots on the large sphere indicate the Lagrangian force points. Without particles, a large wake behind the sphere can be identified, which is typical for a flow around a sphere at this Re number. In the presence of particles, there is a wake present immediately behind the intruder. However, it is only a small wake because the particle density is lower behind the intruder and the gas flows more easily here. This results in large gas velocities behind the intruder and a reduced size of the wake.*

particles is around 0.16 m/s (calculated with Eq. (2.9) using a solid fraction $\varepsilon$ of 0.5), so the bed is in a fluidized state. The restitution coefficient has a relative high value of 0.99 and the friction coefficient a low value of 0.05 to ensure low energy dissipation and thereby a homogenous granular bed. The simulations are started with the intruder at half the height of the container. After 0.5 seconds, the intruder is at $3/10^{\text{th}}$ of the height of the container and the wake behind the intruder is fully developed. Figure 2.7 shows a cross section of the flow around a intruder at this time instant without and with small particles. The size of the CFD elements is $2 \times 2 \times 2$ $\text{mm}^3$ (i.e., the height $h$ of a CFD cell is $d_i/5$ mm).

Figure 2.8 shows the absolute value of the difference between the velocity of a IBM force point and the local vertical air velocity at that point (averaged over all the force points), normalized by the velocity

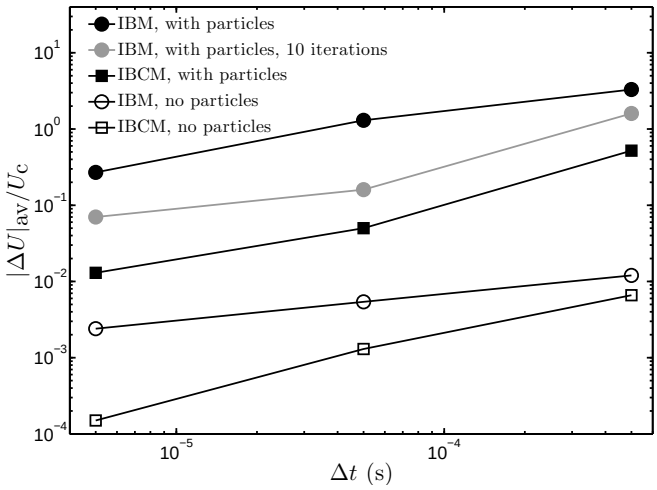


*Figure 2.8: Normalized averaged vertical velocity difference in the box as a function of* $\Delta t$.

of the intruder relative to the gas flow, as a function of the time step. With IBM, the velocity difference is greater than 100% for $\Delta t \geq 5 \cdot 10^{-5}$ s when particles are present, i.e. the no-slip condition on the surface of the intruder is not nearly satisfied. This leads to an unrealistic flow field in which the gas is flowing towards the intruder instead of around it, which was also found in [10]. Using 10 iterations decreases the error significantly, resulting in a more realistic flow field. However, a much smaller velocity difference ($\approx$ 4% with $\Delta t = 5 \cdot 10^{-5}$ s) is found using IBCM, i.e. the no-slip condition on the surface of the sphere is satisfied. Without particles, the error is smaller than 1% for both IBM and IBCM.

In order to investigate the mesh size dependency, we compare the numerically obtained drag force on the intruder $F_{\mathrm{drag}}$ (without small particles) for different mesh sizes (see Fig. 2.9), with the experimentally obtained drag force relation found by Schiller & Naumann [15]:

$$F_{\mathrm{exp}} = c_d \left(\frac{1}{4}\pi d_i^2\right)\left(\frac{1}{2}\rho_g U_c^2\right) \text{ with } c_d = \frac{24}{\mathrm{Re}}(1 + 0.15\mathrm{Re}^{0.687}) \,. \qquad (2.35)$$

For the simulations, we use IBM with a time step of $5 \cdot 10^{-4}$ s. Using a smaller time step or IBCM does not influence the results. The simulation with the linear mapping shows periodic oscillatory behavior with a frequency equal to the frequency of cell changes of the intruder. If

the time step is decreased, the oscillations *increase* in strength and the difference between the experimental and simulated drag force increases, demonstrating again that this mapping method is not very suitable for moving objects. For $h = d_i/5$ mm, the boundary layer around the sphere is too large (see Fig. 2.7), resulting in an overestimation of the drag force on the intruder. Decreasing the mesh size leads to a better correspondence to the experimental result. However, even with a grid size of $d_i/20$ mm, the numerically obtained drag force is 11% larger than the drag force obtained by the empirical drag relation. There is an error margin in empirical drag relations[‖], however Magnaudet *et al.* [17] found in numerical simulations a drag force equal to the empirical drag force at Re=100 and and a slightly lower drag force at Re=200. In their simulations, an axisymmetric body-conforming mesh is used, which enables them to use a much smaller mesh size perpendicular to the intruder surface ($\approx d_i/50$ mm) and a much larger container size ($80d_i$). Using such a large container and small mesh size would require 64 billion CFD cells in our fully 3D model with Cartesian mesh, which is unfeasible on modern day computers. In order to compensate for this overestimation of the drag, one can define the diameter of the intruder slightly smaller than the actual diameter in the flow field calculation.

### 2.6.7 Discussion

There is a large similarity to the way in which the immersed boundary (correction) method and the interaction of small particles with the gas phase, are handled in our numerical model: In both cases, the force on a Lagrangian point is proportional to the difference in velocity between the Lagrangian point and the local (preliminary) gas velocity of the gas phase. Subsequently, this force is mapped to the Eulerian mesh. However, the preliminary velocity used in the immersed boundary method is not equal to the local gas velocity. Furthermore, IBM iterations are sometimes required to obtain a satisfying solution. For this reason, it is not practical to integrate the treatment of small particles and IBM. In case of the immersed boundary *correction* method however, the preliminary velocity is virtually equal to the local flow velocity, so the only significant difference between the treatment of small particles and IBCM is the difference in the "drag" relation. This opens the possibility to integrate the treatment

[‖]For example, the White empirical drag relation [16] ($c_d = \frac{24}{\mathrm{Re}}(1 + \frac{0.25\mathrm{Re}^{0.5}}{1+\mathrm{Re}^{-0.5}} + \frac{0.4}{24}\mathrm{Re})$), yields a drag force 11% higher than than the Schiller & Naumann drag relation at Re=160.

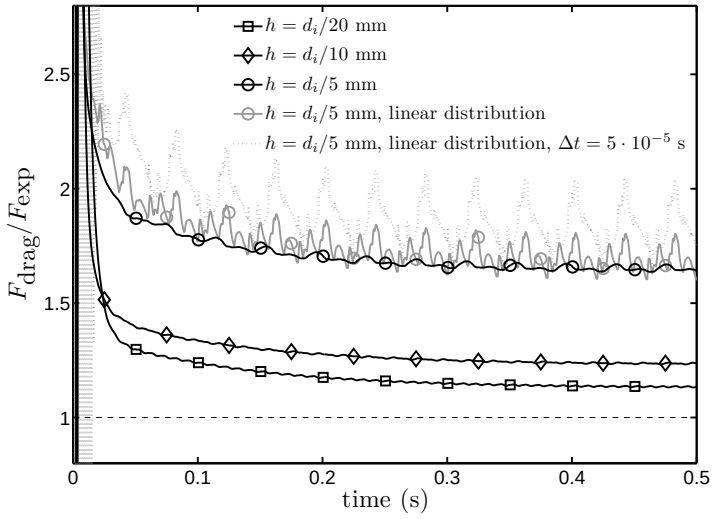


*Figure 2.9: Drag force on the intruder normalized by the empirical drag relation from Schiller & Naumann [15]. In all simulations except one, $\Delta t = 5 \cdot 10^{-4}$ s.*

of small particles and IBCM in the numerical model.

Two methods were tested to further improve the immersed boundary method. First, an extra layer of Lagrangian markers was used at a distance $h$ below the immersed boundary. Second, small particles were placed inside the intruder. Both methods slightly improve the results, but not as much to justify the effort.

## References

[1] M.A. van der Hoef, R. Beetstra, J.A.M. Kuipers, *Lattice-Boltzmann simulations of low-Reynolds-number flow past mono- and bidisperse arrays of spheres: results for the permeability and drag force*, J. Fluid Mech. **528**, p. 233 (2005).

[2] M. Uhlmann, *An immersed boundary method with direct forcing for the simulation of particulate flows*, J. Comp. Phys. **209**, p. 448 (2005).

[3] M.A. van der Hoef, M. Ye, M. van Sint Annaland, A.T. Andrews IV, S. Sundaresan, J.A.M. Kuipers, *Multi-scale modeling of gas-fluidized beds*, Adv. Chem. Eng. **31**, p. 65 (2006).

[4] P.A. Cundall, O.D.L. Strack, *A discrete numerical model for granular assemblies*, Géotechnique **29**, p. 47 (1979).

[5] S. Ergun, *Fluid flow through packed columns*, Chem. Engng. Progs. **48**, p. 89 (1954).

[6] C.Y. Wen, Y.H. Yu, *Mechanics of fluidization*, Chem. Engng. Progs. Symp. Ser. **62**, p. 100 (1966).

[7] B.P.B. Hoomans, J.A.M. Kuipers, W.J. Briels, W.P.M. van Swaaij, *Discrete particle simulation of bubble and slug formation in a two-dimensional gas-fluidised bed: a hard-sphere approach*, Chem. Eng. Sci. **51**, p. 99 (1996).

[8] J. Centrella, J.R. Wilson, *Planar numerical cosmology. II. The difference equations and numerical tests*, Astrophys. J. Suppl. Ser. **54**, 229 (1984).

[9] J.F. Hawley, L.L. Smarr, J.R. Wilson, *A numerical study of nonspherical black hole accretion. II. Finite differencing and code calibration*, Astrophys. J. Suppl. Ser. **55**, 211 (1984).

[10] C. Zeilstra, *Granular Dynamics in Vibrated Beds*, Ph.D. Thesis University of Twente (2007).

[11] C.S. Peskin, *The immersed boundary method*, Acta Numerica **11**, p. 480 (2002).

[12] N.G. Deen, M. Van Sint Annaland and J.A.M. Kuipers, *Multi-scale Modeling of Dispersed Gas-Liquid Two-Phase Flow*, Chem. Eng. Sc. **59**, No. 8-9, pp. 1853-1861 (2004).

[13] Gabriel Caballero, Raymond Bergmann, Devaraj van der Meer, Andrea Prosperetti, and Detlef Lohse, *Role of Air in Granular Jet Formation*, Phys. Rev. Lett. **99**, 018001 (2007).

[14] M.E. Möbius, B.E. Lauderdale, S.R. Nagel, H.M. Jaeger, *Size separation of granular particles*, Nature **414**, p. 270 (2001).

[15] R. Clift and J. R. Grace and M. E. Weber, *Bubbles, drops and particles*, Academics Press, New York (1978).

[16] F.M. White, *Viscous fluid flow*, pp 206-210, (McGraw-Hill, New York, 1997).

[17] J. Magnaudet, M. Rivero, J. Fabre, *Accelerated flows past a rigid sphere or a spherical bubble. Part 1. Steady straining flow*, J. Fluid Mech. **284**, 97 (1995).

# 3

# Faraday heaping: The interplay of air and sand[§]

*In this chapter, numerical simulations are presented of a vibrated granular bed including the effect of the ambient air, generating the famous Faraday heaps known from experiment. A detailed analysis of the forces shows that the heaps are formed and stabilized by the airflow through the bed while the gap between bed and vibrating bottom is growing. Importantly, the simulations also explain the heaping instability of the initially flat surface.*

## 3.1 Introduction

Faraday heaping is one of the most celebrated and beautiful examples of the effect of air on granular matter. When a box with fine dry sand is vertically vibrated or tapped, its initially flat surface turns into a landscape of small heaps, which in the course of time tend to coarsen into larger heaps [1–5]. At very low pressure, when the air drag on the particles can be ignored, no heaping of any kind is observed, implying that the ambient air plays a crucial part in the heaping instability, as was already noted by Faraday [6]. The subject has received considerable attention since its discovery by Chladni and Faraday, especially in recent years with the increased interest in granular matter. These studies - all experimental - have led to several explanations as to *why* the heaps keep a stable shape, including internal avalanches [1], horizontal pressure gradients [3], and the stability of inclined surfaces [7]. In this chapter we present numerical simulations of the Faraday heaping effect, including the coarsening process of the small heaps into larger heaps. Although numerical simulations

[§]Published as: H.J. van Gerner, M.A. van der Hoef, D. van der Meer, and K. van der Weele, *Interplay of air and sand: Faraday heaping unravelled*, Phys. Rev. E **76**, 051305 (2007).

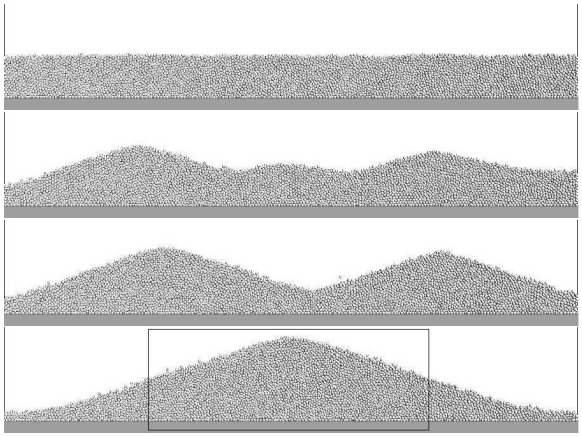

*Figure 3.1: Numerically simulated Faraday heaping in a vibrated granular bed after 0, 30, 55 and 240 driving cycles. After a few cycles, some slight surface ripples start to grow into small heaps, which coarsen into larger heaps until a steady state with a single Faraday heap is reached.*

of tilting in a water-immersed granular bed have been reported earlier [8], this is the first time, to our knowledge, that a genuine Faraday heap is simulated. The simulations allow us to obtain a detailed insight into the physical mechanism at work, elucidating the role of the ambient air, and discriminating between the previously proposed explanations of the heaping effect.

## 3.2 Numerical model

For the simulation we use the hybrid Granular Dynamics (GD) Computational Fluid Dynamics (CFD) code described in chapter 2. The GD code calculates the particle trajectories from Newton's law, with the particle-particle interactions being given by a 3D soft sphere collision model including tangential friction. The CFD code evaluates the full Navier-Stokes equations by a finite difference method. For the two-way coupling between the particles and the gas phase, the drag force relations described by Eq. 2.10 are used*. The simulated system, Fig. 3.1, contains 13,500 spherical particles ($\rho = 2500$ kg/m$^3$) of average diameter 0.5 mm, with a Gaussian size distribution ($\sigma = 0.055$ mm) to avoid excessive

*Our simulations show that the precise form of the drag force is not very critical: Simulation carried out with the Ergun drag force relation (Eq. 2.9) led to similar results.

ordering of the bed. In all simulations the coefficient of restitution is set to 0.90 for the normal direction, and to 0.33 for the tangential direction. For the particle-wall interaction the same collision parameters are used as for the particle-particle interaction. The friction coefficient is set to 0.2. All these parameters are typical for glass spheres in a glass box. The dimensions of the box are $100\times50\times2.1$ mm$^3$ ($W \times H \times D$), i.e., four particles fit in the depth direction and the mean height of the granular bed in rest is about fourteen particle diameters. The box is closed airtight (which is modelled using the cell-cut method, see section 2.6.1), containing air at atmospheric pressure without gas leaving or entering the system. For the numerical simulations, the box is divided in $80\times60\times1$ ($W \times H \times D$) CFD cells. It was found that using more CFD cells did not produce different results.

## 3.3 Steady state heap

Starting with a flat bed, and vertically vibrating it using a sinusoidal driving with frequency $f = 6.25$ Hz and amplitude $a = 10$ mm (corresponding to a dimensionless acceleration $\Gamma = a(2\pi f)^2/g = 1.6$), we typically observe the following series of events (Fig. 3.1): Already after a few cycles, some random surface fluctuations are seen to grow into small heaps. After this, on a much longer time scale, the small heaps merge together into larger heaps until finally a steady state with a single heap is reached. Under vacuum conditions (i.e., if we turn off the gas-particle interaction in the simulations) no heap is formed, in accordance with the experimental findings [2, 6]. Also, if we remove the air once a heap is formed, it disappears within 15 cycles.

We first focus on the steady state with one heap and address the question how the heap keeps its stable shape. A good starting point is given by Fig. 3.2, which shows the dynamical equilibrium that is present within the heap. The particles are seen to be in constant motion, following a circulation pattern that consists of two convection rolls, in which the outward avalanche in the upper surface layers is balanced by a collective inward motion of the particles in the interior of the heap. This pattern confirms the circulation proposed by Faraday [6] and found experimentally by Behringer *et al.* [4]; half of the pattern (one convection roll) was found numerically for water-immersed beds by Milburn *et al.* [8].

How is the circulation sustained? To reveal and understand the mechanism, we follow the heap during a complete vibration cycle, see

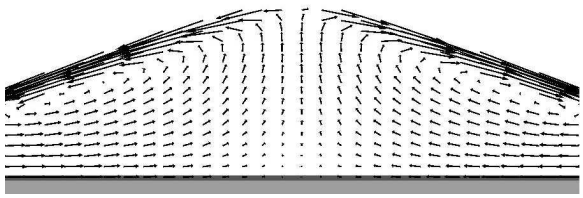

*Figure 3.2: Circulation in the Faraday heap: The arrows indicate the particle displacement (multiplied by two for clarity) during one driving cycle, averaged over* 25 *cycles. The part of the heap shown here corresponds to the black box in Fig. 3.1.*

the snapshots at phase angles 90 °, 171 °, 234 ° and 360 ° in Fig. 3.3. The vertical bands of grey marker particles illustrate again the circulation of Fig. 3.2, the black arrows indicate the drag force of the air on the particles. Initially, the bottom plate and bed are moving upwards together. The first snapshot in Fig. 3.3 is taken at 90 °, when the bed has already detached from the bottom and a gap has started to grow between bottom and bed, causing a region of low pressure underneath the heap. The isobars are indicated with black lines in this figure. The pressure above the heap is approximately constant, because the air resistance in the heap is much higher than above the heap. For this reason, the isobars run parallel to the surface of the heap, resulting in a airflow perpendicular to this surface. Furthermore, the pressure is lowest underneath the center of the heap because the air enters more easily through the sides than through the center. This generates a downward airflow through the heap (strong at the sides where the heap is thin, weaker in the center), with a noticeable inward component. The air drag thus accelerates the particles down and inwards.

At 171 °, the heap is in free flight. The contact forces between the particles as well as the air drag are very small at this stage, so the particles within the heap maintain their inward motion and hence the number of particles near the center increases. It can be seen that the bed itself becomes slightly curved, because the downward drag at 90 ° was larger at the sides. At 234 °, the bed is coming down again, and the sides have in fact already reached the bottom. The particles now experience a large up- and outward drag force due to the increased air pressure between the box and the descending granular bed. However, the collision with the bottom will rapidly compactify the heap, so that the particles get locked and cannot move anymore. Finally, at 360 ° the heap is in rest except for a thin layer

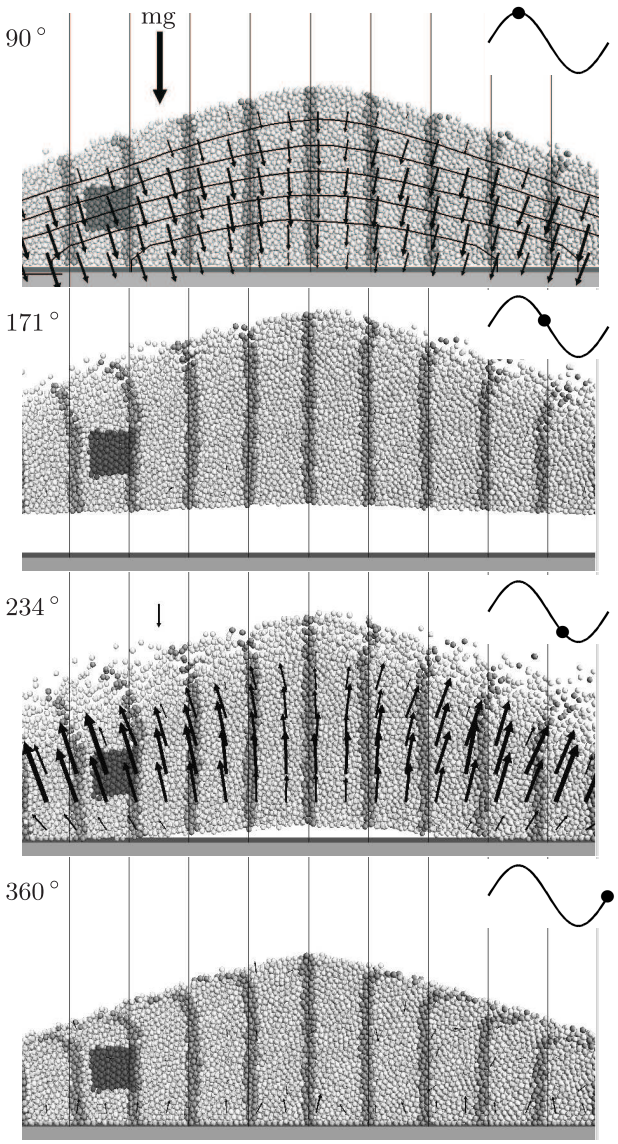


*Figure 3.3: The stable Faraday heap (cf Fig. 3.2) at four successive phases during one driving cycle. The arrows indicate the air drag force on the particles averaged per CFD cell (one out of every 4 arrows is shown); at* $234\,^\circ$*, when the drag force is very strong, the arrows are scaled by a factor of* $1/3$ *compared to those at the other phase angles. For comparison, the gravitational force on a particle is shown in the* $90\,^\circ$ *figure (and also at* $234\,^\circ$*); the ratio of gravity and air drag forces, which is comparable to the Bagnold number [13], is of order one in this simulation. The dynamics of the rectangular ensemble of dark particles is further analyzed in Fig. 3.4. A video of one driving cycle can be found on the enclosed CD-ROM.*

of particles that avalanches down its slopes. Since we are in a steady state, this precisely neutralizes the surplus of particles at the heap's center built up during the previous stages, and thereby completes the circulation pattern of Fig. 3.2.

The above findings are similar to the experimental observations of Thomas and Squires [3], who found - from floor pressure measurements at multiple locations - a horizontal component of the pressure gradient which drives the particles inward during the first part of the cycle, when the particles are free to move. However, the horizontal component of the pressure gradient not only arises from air entering the heap more easily through the sides (resulting in a horizontal pressure gradient at the floor) but also from the isobars running parallel to the surface[†], which induces a horizontal component of the pressure gradient in the bed. We further investigated the significance of this second mechanism by carrying out a simulation in which the top of the box is closed and the bottom is permeable for air (i.e., a constant pressure at the bottom is prescribed): Also in this case heaps are formed, solely due to the fact that the isobars are parallel to the surface, without any pressure gradient at the bottom. The inward pressure gradient due to the isobars running parallel to the surface plays an especially important role at onset of heaping, when the horizontal pressure gradient on the floor is relative small and the main contribution to the horizontal component of the pressure gradient stems from the curved isobars along the surface.

For a quantitative description of the heaping mechanism we show in Fig. 3.4(a) the *horizontal* components of the contact and drag forces per unit mass on the rectangular ensemble in Fig. 3.3, during one driving cycle. In Fig. 3.4(b) we integrate these forces twice, which yields the virtual displacement of the ensemble due to the contact and drag forces individually. The sum of these two virtual displacements is the actual horizontal displacement of the ensemble, given by the solid black curve in Fig. 3.4(b).

During the very first stages, the particles are seen to move slightly outward due to the contact forces, which are initially quite large, but rapidly decrease as the bed loosens up. At $40^\circ$ they become practically zero. At this point the gap between the bed and the bottom starts to grow,

[†]Thomas and Squires use a linear interpolation between floor pressures and the constant surface pressure to obtain a pressure within the bed. This interpolation results in isobars that follow the surface - this is however not mentioned in their article [3], and also not the important consequence of the resulting inward pressure gradient near the surface.

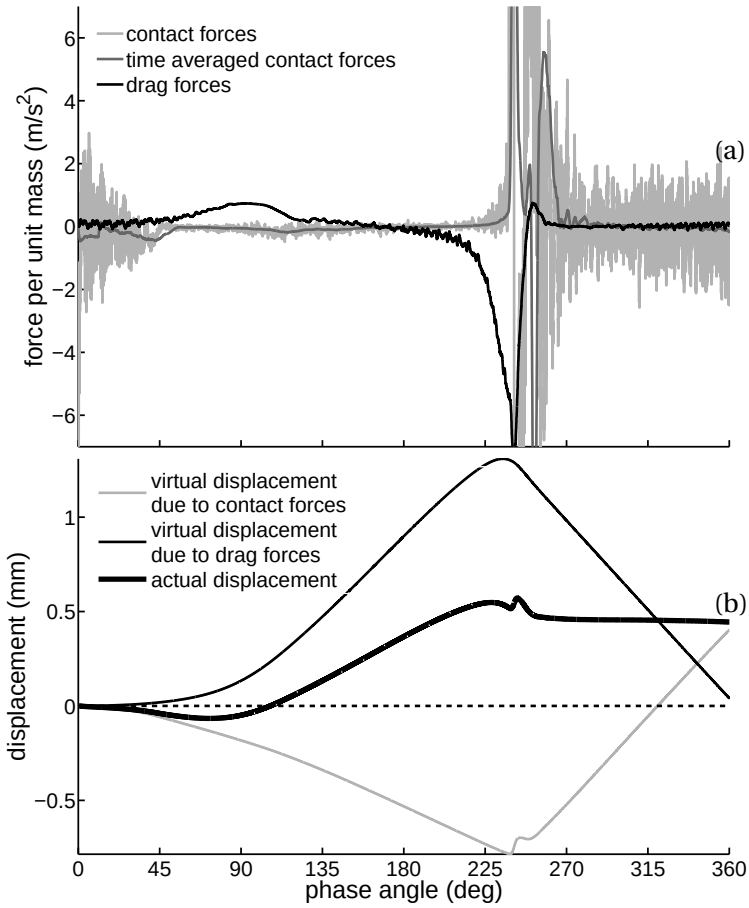


*Figure 3.4: (a) The averaged horizontal components of the contact and drag forces (per unit mass) on the rectangular ensemble of dark particles in Fig. 3.3, as a function of time during a complete driving cycle. Positive forces point towards the center of heap. (b) The virtual displacements due to the contact and drag forces individually, and their sum, i.e., the actual horizontal displacement of the ensemble. The net displacement during one cycle* (0.43 *mm towards the center of the heap) is already reached at* 260 °. *After that, the heap is fully compactified and the particles in the ensemble are locked until a new cycle starts.*

inducing the inward air drag discussed above, which reaches a maximum value around 90°. This drag force succeeds in turning the motion of the ensemble around at 75°, and the particles start to move inward. This motion is maintained up to 220°. At 200° the gap between bottom and bed is largest and the ensemble hardly experiences any forces. After 200° the gap becomes smaller again and the air drag is now directed in the opposite direction, reversing the motion of the ensemble at 220°. Shortly afterwards ($\approx$ 240°), the heap collides with the bottom - sides first - and this sends a shock wave through the bed with a large horizontal *inward* component. As a result, the motion is turned around again towards the center of the heap (exemplified by the small hump in the total displacement curve, Fig. 3.4(b)) and the bed compactifies, causing the wild turmoil of contact forces in Fig. 3.4(a) at 240°-260° and fixating the particles. Figure 3.4(b) shows that around 260° the ensemble comes to a standstill, its final horizontal displacement after one cycle being 0.43 mm inward, slightly less than a particle diameter.

## 3.4 Evolution of an initially flat bed

So far we focused on the steady state of a single Faraday heap, but how does this steady state come into existence? Figure 3.5(a) shows the evolution of an initially flat bed (which was created by giving all particles a random velocity with a standard deviation of 0.1 m/s) as a function of the number of cycles. The width of the box $W$ is here increased from 0.1 to 0.3 m (to accommodate a reasonable number of heaps) and 40,500 instead of 13,500 particles are used, thus keeping the mean depth of the granular bed constant. We observe a two-stage coarsening process [14, 15]: $(a)$ A fast initial stage where seven small heaps are formed within 50 cycles, followed by $(b)$ a slow second stage where the heaps merge and combine into two larger heaps; it is anticipated that these heaps will eventually merge into one single heap, as in Fig. 3.1, however, since the merging slows down considerably with a decreasing number of heaps, the required computing time is beyond our computer resources. Interestingly, during the whole coarsening process the slopes of the heaps have a nearly constant angle of 18.5°, which is lower than the static angle of repose (22.7°, determined by an independent simulation).

With respect to stage $(a)$, detailed simulations show that as soon as a slight ripple appears on the surface, the isobars follow the surface and the local air drag directly acquires a noticeable horizontal component,

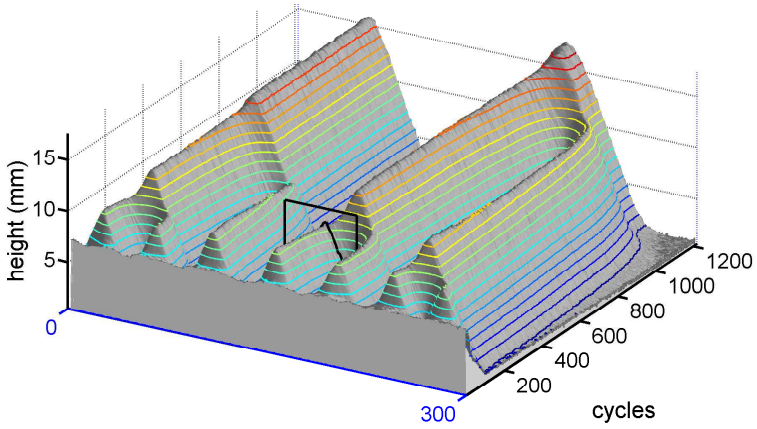


*Figure 3.5: Evolution of the heap pattern in a box three times as wide as that in Fig. 3.1. A video of this evolution can be found on the enclosed CD-ROM.*

dragging particles towards the center via the mechanism of Fig. 3.3. Initially, the slope of the ripple is so small that there is hardly any avalanching. Thus it steadily grows, increasing its slope and thereby the number of particles that avalanche down, until at some specific angle (here 18.5°) an equilibrium is reached between the fluxes due to avalanching and inward drag force. This is illustrated in Fig. 3.6(a), which shows the averaged horizontal displacement per cycle of inward and outward moving particles separately, as a function of the angle of the slope. The measurements for heap angles up to 18.5° are obtained during the first 50 cycles and averaged over the five center heaps in Fig. 3.5. The measurements for heap angles between 18.5° and 22° are obtained by pouring particles on the seven heaps after 50 cycles, until the static angle of repose is reached, and than restart the vibration of the system. The error bars denote the standard deviation of the data.

After stage $(a)$, seven heaps are present in the box with a width $W$ of 0.3 m, independent of the vibration parameters: Simulations carried out at different frequencies and amplitudes always result in this wave number. An almost constant wave number was also found experimentally in [16], although the wavelength found there is around 6 mm, while the wavelength in our simulations is around 43 mm. A Fourier transform of Fig. 3.5 shows that the wave number is already strongly present in the initial condition (Fig. 3.7a), although the difference in height between the peaks and valleys is less than one particle diameter. The question arises if the wave number of 7 is inherent to the heaping instability, or just a result

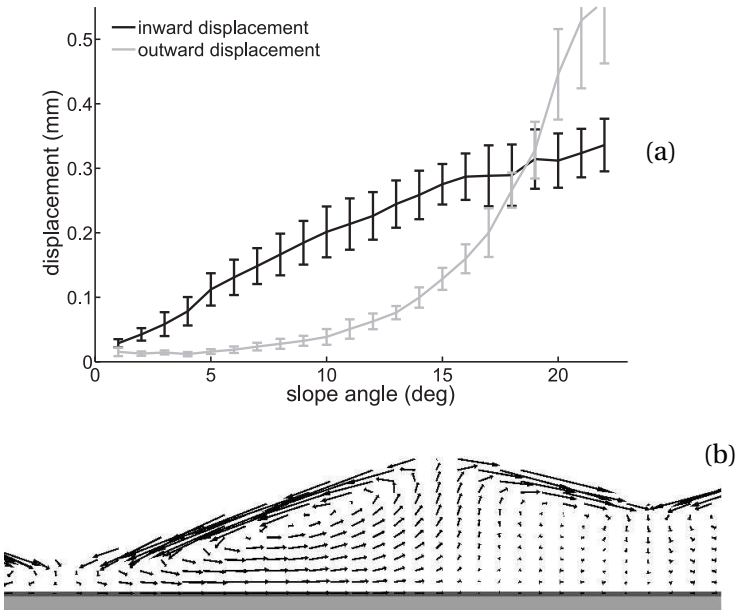


*Figure 3.6: (a) Averaged horizontal particle displacement in a heap, due to the inward air drag (black) and outward avalanching (gray), as a function of the growing slope angle, during the first stage when the heaps are formed. The displacements balance each other at a slope of* $18.5^\circ$*. (b) Particle displacement during one cycle in the heap indicated by the frame in Fig. 3.5, which is about to merge with the neighboring heap to the right. The displacements are averaged over five cycles around* 240 *cycles and multiplied by two for clarity.*

of the initial condition of the granular bed. To answer this question, the initial granular bed is first vibrated for 5 seconds at a frequency of 200 Hz and an amplitude of $1 \cdot 10^{-5}$m, resulting in a granular bed with a nearly flat surface. The difference in height between the peaks and valleys is less than one particle diameter and a Fourier transform of the surface shows small humps at many wave numbers. Subsequently, a heaping simulation with this bed as initial condition is carried out, resulting after 45 cycles in a collection of heaps with different sizes and no specific wave number (Fig. 3.7(b)), although wave numbers above 15 are not present anymore; a detailed analysis shows that the heaplets with larger wave numbers merge into heaps with small wave numbers before they reach their steady state angle. It may be concluded that the wave number during stage $(a)$ is very sensitive to the initial condition and that the wave number of 7 is not related to the vibration parameters or particle and box dimensions.

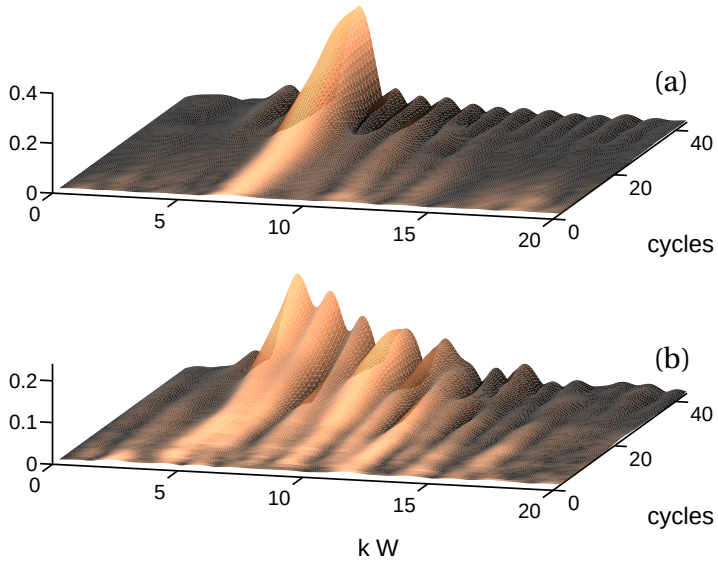


*Figure 3.7: (a) Fourier transform of the first 45 cycles of Fig. 3.5 as a function of the wave number $k$ (made dimensionless by the width of the box $W$). The color indicates the relative value of the Fourier transform per cycle, the height is the absolute value. The initial number of 7 heaps is already present in the initial condition and grows stronger as the heaps grow during the first 30 cycles. (b) Fourier transform of the first 45 cycles of a simulation with different initial conditions, resulting in a landscape of heaps without any specific wavelength.*

To explain the physics of stage $(b)$, i.e., why the heaps merge, we proceed analogously as for the single Faraday heap and consider the averaged displacement of particles during one cycle in the region indicated with black lines in Fig. 3.5 after 240 cycles (Fig. 3.6(b)). The arrows show that the inward motion inside the left part of the selected heap is much larger than in the right part. This asymmetry in the displacement field is caused by the fact that the slope of the left side of the heap is longer than the right slope, so the inward drag force is stronger here. This will result in a displacement of the entire heap towards the right, and the merging with the neighboring heap. Thus the coarsening of heaps takes place primarily because heaps move towards each other and not because the height of one heap steadily increases while the height of another heap decreases, as suggested in [17]. The coarsening process is discussed in more detail in chapter 4.

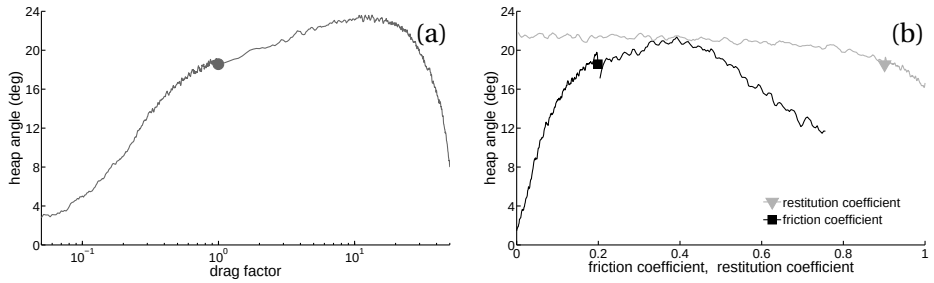


*Figure 3.8: (a) Heap angle as a function of the air drag factor. (b) Heap angle as a function of restitution and friction coefficient. The measurements are obtained from simulations in which one parameter is changed slightly after each vibration cycle. The initial condition for each simulation, corresponding to the steady state heap of Fig. 3.1, is indicated with a marker.*

## 3.5 Influence of different parameters

### 3.5.1 Air drag, friction, and restitution coefficient

The outcome of a heaping simulation depends on a number of parameters. In order to obtain insight in the influence of these parameters, simulations are carried out where one parameter is slightly changed after each vibration cycle. The rate of change of a parameter was chosen such that decreasing the rate of change any further did not produce significantly different results. The initial condition for each simulation is the steady state heap shown in Fig. 3.1 and is indicated by the markers in Fig. 3.8.

One of the most important parameters which influences the heaping is the ratio of the air drag and the gravity force, comparable to the (reciprocal) Bagnold number that plays an important role in the description of aerial transport of sand in deserts [13]. If it is reduced to zero, no heaping of any kind is observed.

The drag force acting on the granular bed can be represented as the drag force on a single isolated particle in the limit of zero Reynolds number (the Stokes-Einstein relation) multiplied by a dimensionless empirical function $f$ that depends on the packing fraction $\phi$ and Reynolds number Re, e.g, the Ergun relation [18] or the drag force relation described in [12]: $F_{\mathrm{drag}} = 3\pi\mu dUf(\phi, \mathrm{Re})$, where $\mu$ is the viscosity of the medium, $d$ the diameter of the particles, and $U$ the velocity of the air relative to the bed.

The gravitational force on each particle (of mass $m$) is simply $F_g = mg = \rho\pi g d^3/6$, with $\rho$ the density of the particles and $g$ the gravitational

acceleration. Hence the dimensionless number that gives the ratio of the (typical) drag force and gravity takes the form:

$$B = \frac{F_{\text{drag}}}{F_g} = \frac{18\mu U}{\rho g d^2} f(\phi, \text{Re}). \tag{3.1}$$

In this equation, the particle size and density ($d$ and $\rho$), gravity ($g$), and viscosity ($\mu$) are the *control* parameters, whereas $\phi$, Re, and $U$ are *response* parameters of the system, which vary through the system and change if we vary any one of the control parameters. This means that it is not feasible to systematically vary the dimensionless number Eq. (3.1) via one of the physical control parameters. Moreover, a modification of the control parameters may not only change the ratio $B$, but also other quantities that influence the heaping. Therefore, we choose to modify the level of the air drag $F_{\text{drag}}$ artificially by introducing an *air drag factor*, i.e., a factor by which we multiply the air drag obtained from the drag relation. The result is shown in Fig. 3.8(a): If the air drag factor is decreased from its default value 1 towards zero, the heap angle becomes smaller and smaller, just as expected. Likewise, if we increase the air drag factor, the heap angle grows and reaches a maximum at a drag factor of 20. Increasing the drag factor still further results in a *decrease* of the heap angle; detailed simulations show that for a drag factor of 40 the air drag acting on the particles becomes so strong that the bed does not detach from the plate anymore and hence the particles can hardly move inward.

For comparison we also performed a limited set of simulations in which we varied a physical control parameter (particle size and density, gravity, viscosity). We found that changing either the viscosity $\mu$ or the particle density $\rho$ gave similar results as a corresponding change of the air drag factor[‡]. However, decreasing the particle diameter $d$ by a factor of 7 turned out to give a quite different result than simply multiplying the drag factor by 49; in particular, in the former case the granular bed is much more diluted (i.e., $\phi$ becomes smaller) during the free flight phase. Finally, changing the gravitational acceleration $g$ leads to different results (than the corresponding reciprocal change in the air drag factor) because it does not only influences the dimensionless ratio $B$, but the dimensionless

[‡]Even if the viscosity of the fluid is reduced to zero, a small drag force acts on the particles, because part of the drag force does not depend on the viscosity, but on the pressure drop over a particle (the so-called form drag, which is included in the emperical models). However, for these systems, the form drag is much smaller than the viscous drag and changing $\mu$ leads to simular results as changing the air drag factor.

acceleration $\Gamma$ as well[§]. Therefore, it can be concluded that the influence of the particle density $\rho$ and the viscosity $\mu$ on the heap formation is controlled exclusively by the ratio $B$, which is not true for the diameter $d$ or gravitational acceleration $g$.

Changing the *friction coefficient* has a pronounced influence on the heap angle. Because the angle of repose of a pile of particles is $0\,^\circ$ without any friction, the heap must disappear when the friction coefficient is reduced to zero. On the other hand, increasing the friction above 0.4 also results in a decrease of the heap angle. This can also be explained since the inward motion of the particles due to the air drag is hindered by the increased particle-wall and particle-particle friction.

Interestingly, the *restitution coefficient* only has a small influence on the heap angle at these vibration parameters. Even at a restitution coefficient of 1 (the elastic case), the energy dissipation due to friction is sufficient to prevent the heap from collapsing during impact. However, simulations show that the restitution coefficient can have a marked influence at more vigorous shaking conditions: When the box is vibrated with a dimensionless acceleration $\Gamma$ of 2.4 (at a frequency $f = 12.5$ Hz), the heap collapses with a restitution coefficient of 0.9 but remains stable with a restitution coefficient of 0.5.

### 3.5.2 Vibration amplitude and acceleration

The vibration amplitude $a$ and dimensionless acceleration $\Gamma$ are important parameters for Faraday heaping. The influence of these parameters is systematically studied in simulations at five different frequencies (4.17, 5, 6.25, 9, and 17 Hz). In each simulation, the dimensionless acceleration $\Gamma$ starts with 1.2 and is increased (via the amplitude $a$) with 0.005 after each vibration cycle. This value was chosen such that decreasing this value any further did not produce significantly different results. The initial condition for the simulations is the steady state heap in Fig. 3.1. The heap angle as a function of vibration amplitude $a$ and dimensionless acceleration $\Gamma$ that results from these simulations, is indicated by colors in the straight lines in Fig. 3.9(a). The heap angle slowly decreases with increasing acceleration until a dimensionless acceleration of approximately 1.9, above which the heap collapses and the heap angle reduces to $0\,^\circ$.

[§]The dimensionless acceleration $\Gamma$ is important because, in a vacuum, it is the *only* parameter that determines the phase angle at which the granular mass detaches from and collides with the bottom of the box during a vibration cycle.

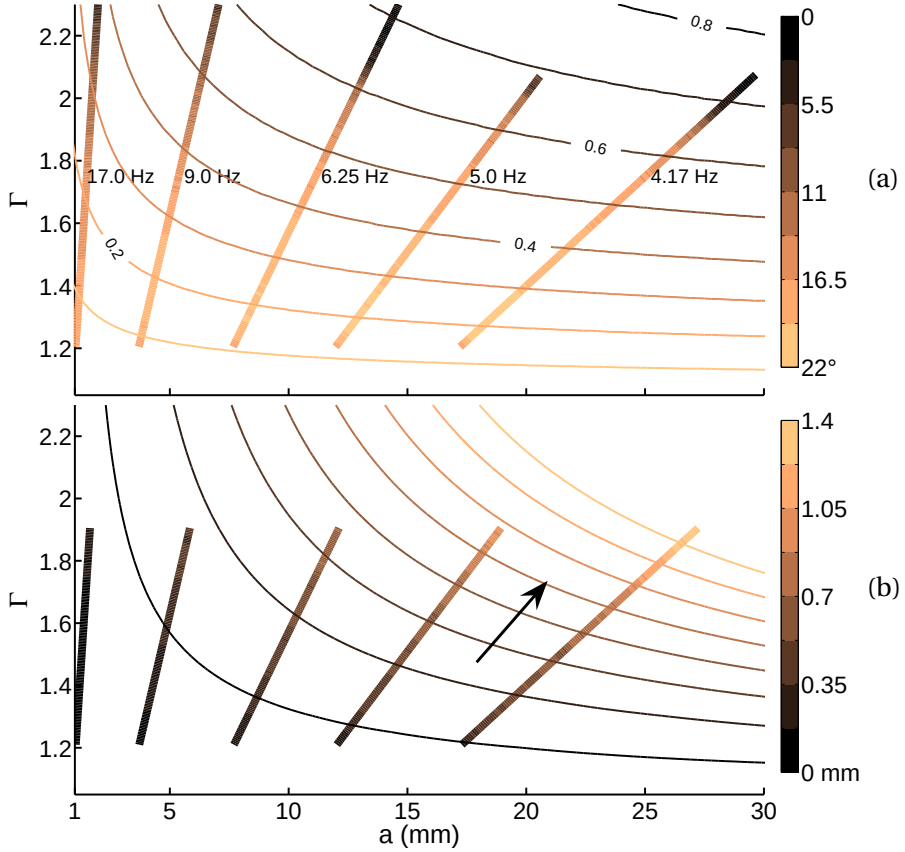


*Figure 3.9: (a) Straight lines: Heap angle as a function of vibration amplitude $a$ and dimensionless acceleration $\Gamma$. The color bar indicates the heap angle in degrees. The measurements are obtained from simulations at five different frequencies as indicated. Contour lines: Impact velocity obtained from the model. The increment between the contour lines is 0.1 m/s. (b) Straight lines: Inward particle motion obtained from the same simulations. The color bar indicates the inward displacement per particle per vibration cycle in mm. The inward displacement increases in the direction of the arrow. Contour lines: Inward motion of the particles obtained from the model. The maximum value of the inward motion in the model is scaled to match the maximum value in the simulation.*

Simulations show that the inward motion during one vibration cycle (and therefore the velocity of the Faraday circulation) depends on both vibration acceleration and amplitude. The straight lines in Fig. 3.9(b) show that the inward motion during one vibration cycle, is small for low vibration amplitudes, that is, at equal values of $\Gamma$ the magnitude of the inward motion grows for increasing $a$[¶]. This is reflected in the time required to evolve from an initially flat surface to 7 small heaps: Around 20 seconds in a simulation with a vibration amplitude $a = 2.5$ mm (and frequency $f = 12.5$ Hz) and just 3 seconds in a simulation with $a = 22$ mm (and $f = 4.17$ Hz); $\Gamma$ is 1.6 in both simulations.

The simulations show that the heap disappears with increasing acceleration, despite the fact that the inward motion increases. In order to gain more insight in the influence of the vibration amplitude and acceleration, a simple one-dimensional model was created which consists of a completely inelastic object (representing the total granular mass) bouncing on a vibrating plate. It is assumed that the velocity of the air is equal to the velocity of the vibrating plate. The vertical component of the air drag on the object is calculated with the Ergun drag force relation [18] on a single particle, where it is assumed that the porosity of the granular mass has a constant value of 0.5. Because the pressure contours are parallel to the heap surface (and the air drag force is perpendicular to the pressure contours), the horizontal drag force on the particles is calculated by multiplying the vertical drag force with the sine of a steady heap angle of $18.5^\circ$. Integrating the horizontal drag force twice (until impact of the object with the plate) results in the inward motion of the particles during one vibration cycle, as indicated by the contour lines in Fig. 3.9(b). The results from the model correspond well with the results from the simulations: The inward motion (and therefore the Faraday circulation) increases with increasing amplitude and acceleration.

The model also calculates the impact velocity of the object on the vibrating plate. This impact velocity is indicated by contour lines in Fig. 3.9(a). In order to determine the relation between the impact velocity and the outward displacement of the particles due to avalanching, we carried out simulations in which a heap was thrown with different velocities onto a horizontal plate. The simulations showed that avalanching strongly increases with increasing impact velocity; the precise relation however depends on various parameters as heap size, porosity before

[¶]The simulation results of the inward motion above $\Gamma \approx 1.9$ are very scattered (because the heap does not remain in the same position) and are therefore not shown in the plot.

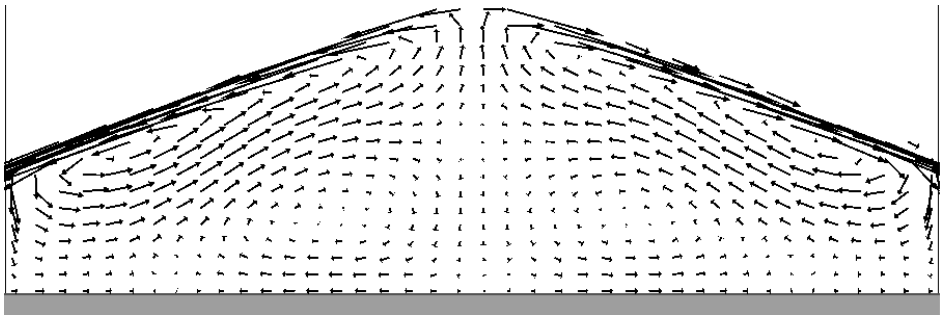

*Figure 3.10: Circulation in the Faraday heap: The arrows indicate the particle displacement (multiplied by five for clarity) during one driving cycle, averaged over* 10 *cycles. Apart from the usual Faraday circulation close to the heap surface, we also find a weak inverse convection role in the lower central region of the heap.*

impact, etc.

So why does the heap disappear with increasing acceleration while the inward motion of the particles increases? From the model and the simulations, it follows that the inward motion due to air drag increases with vibration amplitude and acceleration, but a limit is reached when the impact of the heap on the plate becomes so severe that the outward motion due to avalanching can never be compensated by the inward motion of the particles.

### 3.5.3 Bed height

In the simulations shown previously, the mean height of the granular bed in rest is about 14 particles diameters. In order to investigate the influence of the bed height, a simulation was carried out with three times as many particles, resulting in a mean height of the granular bed in rest of about 42 particles diameters. In this system, the horizontal pressure gradient driving the heaping mechanism is larger near the surface than in the interior. For this reason, the average particle displacement during one vibration cycle is larger near the surface than in the interior of the heap (see Fig. 3.10). This is consistent with the experimental observation in [11], where it was shown that for very deep granular beds ($>$500 particle diameters), the Faraday circulation is confined to a thin surface layer. Close inspection of Fig. 3.10 reveals a special characteristic of these deep granular beds: Near the bottom of the heap, the particles move slightly outward, although the pressure gradient is still directed inward at that

location. This can be explained by the fact that the inward pressure gradient (at a phase angle of 90° during a vibration cycle) forces the particles toward the center of the heap, where they can move upward against gravity but also downward. If one descents deeper from the peak into the heap, the particles cannot move upward due to the weight of the column of particles above. Instead, the weight of this column forces the particles downward, resulting in a weak inverse convection roll in the central lower region of the heap.

## 3.6 Heaping in a bronze-glass system

In closing this chapter, we would like to touch upon a very remarkable effect of air on granular matter, the segregation of a mixture of equally sized bronze and glass particles under vertical vibrations. Amazingly, the heavy bronze particles rise to the top, while the lighter glass particles sink to the bottom [19]. This effect can be explained as follows [20]: Around a phase angle of 90° during a vibration cycle, the granular bed has detached from the bottom and a gap starts to grow between bottom and bed, causing a region of low pressure underneath the heap. This results in an airflow through the bed which drags the glass particles - since they have a lower inertia - more to the bottom of the container than the bronze particles. When the bed is falling down on the bottom plate, the opposite phenomenon occurs. However, the collision with the bottom will rapidly compactify the granular mass, so that the particles get locked and cannot move anymore.

This mechanism is very similar to the Faraday heaping mechanism and this makes it interesting to simulate Faraday heap in this bidisperse system. The simulated system (see Fig. 3.11) contains 9500 glass ($\rho = 2500$ kg/m$^3$) and 4000 bronze ($\rho = 8900$ kg/m$^3$) spherical particles of average diameter 0.25 mm, with a Gaussian size distribution ($\sigma = 0.025$ mm) to avoid excessive ordering of the bed. All other particle and vibration parameters are equal to the ones used in the heaping simulations. The segregation and heap formation occur simultaneously: After a few cycles, the initially randomly distributed bronze particles start to cluster and rise towards the top, forming a layer of heavy bronze particles on top of the light glass particles. At the same time, two heaps are formed, with a core of glass particles and slopes consisting of bronze particles. After 25 driving cycles, the glass core breaks through the bronze layer, and glass particles avalanche over the bronze slopes.

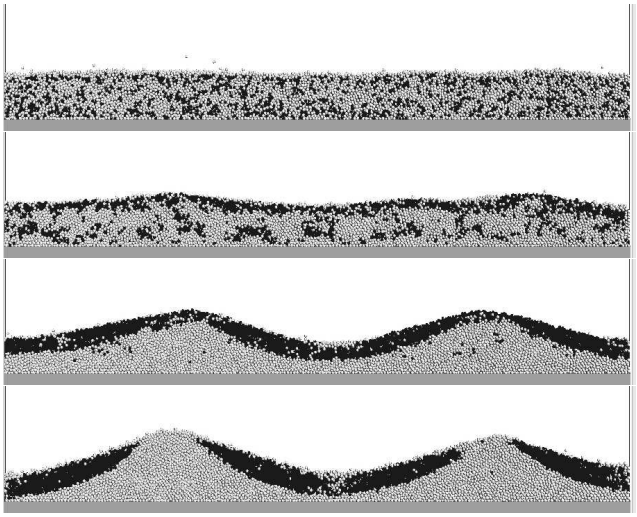

*Figure 3.11: Numerically simulated Faraday heaping in a vibrated container filled with 4000 bronze particles (black) and 9500 glass particles (white) after 1, 5, 12 and 25 driving cycles.*

## 3.7 Conclusion

In conclusion, the simulations give a detailed insight into the mechanism of Faraday heaping, elucidating in particular the role of the ambient air. Faraday's original assertion that the air must play a key role has been fully verified [6]; the experiments by Thomas and Squires [3] have been validated; their proposed pressure-gradient mechanism has been identified as the correct one; moreover, we have shown the important role being played by the isobars running parallel to the surface of the granular bed.

The simulations also explain how the system evolves from an initially flat surface to a single stable heap: very small initial surface deflection are unstable, leading to a transient state of several small heaps, which (on a much longer time scale) move toward each other due to the reduced inward drag force in the side of a heap that is close to another one.

Finally, we have shown that the Faraday circulation velocity increases with vibration amplitude and acceleration. A limit is reached when the impact of the bed on the plate becomes too strong and the outward motion due to avalanching becomes larger than the inward motion due to the air drag. That is why the heaping phenomenon breaks down at large shaking strengths.

## References

[1] C. Laroche, S. Douady, and S. Fauve, *Convective Flow of granular masses under vertical vibrations*, J. Phys. **50**, 699 (1989).

[2] H.K. Pak, E. van Doorn, and R.P. Behringer, *Effects of Ambient Gases on Granular Materials under Vertical Vibration*, Phys. Rev. Lett. **74**, 4643 (1995).

[3] B. Thomas and A.M. Squires, *Support for Faraday's View of Circulation in a Fine-Powder Chladni Heap*, Phys. Rev. Lett. **81**, 574 (1998).

[4] R.P. Behringer, E. van Doorn, R.R. Hartley, and H.K. Pak, *Making a rough place "plane": why heaping of vertically shaken sand must stop at low pressures*, Gran. Matter **4**, 9 (2002).

[5] H.M. Jaeger, S.R. Nagel, and R.P. Behringer, *Granular solids, liquids, and gases* , Rev. Mod. Phys. **68**, 1259 (1996).

[6] M. Faraday, *On a peculiar class of acoustical figures; and on certain Forms assumed by groups of particles upon vibrating elastic surfaces*, Phil. Trans. R. Soc. London **121**, 299 (1831).

[7] J. Duran, *The physics of fine powders: pluging and surface instabilities*, C. R. Physique **3**, 217 (2002).

[8] R.J. Milburn, M.A. Naylor, A.J. Smith, M.C. Leaper, K. Good, M.R. Swift, and P.J. King, *Faraday tilting of water-immersed granular beds*, Phys. Rev. E **71**, 011308 (2005).

[9] M.A. van der Hoef, M. Ye, M. van Sint Annaland, A.T. Andrews IV, S. Sundaresan, and J.A.M. Kuipers, *Multi-Scale Modeling of Gas-Fluidized Beds*, Adv. Chem. Eng. **31**, 65 (2006).

[10] N.G. Deen, M. van Sint Annaland, M.A. van der Hoef, and J.A.M. Kuipers, *Review of discrete particle modeling of fluidized beds*, Chem. Eng. Sc. **62**, 28 (2007).

[11] K. Kumar, E. Falcon, K.M. Bajaj, and S. Fauve, *Shape of convective cell in Faraday experiment with fine granular materials*, Physica A **270**, 97 (1999).

[12] M. van der Hoef, R. Beetstra, and J.A.M. Kuipers, *Lattice-Boltzmann simulation of low-Reynolds-number flow past mono- and bidisperese arrays of spheres: results for the permeability and drag force*, J. Fluid Mech. **528**, 233 (2005).

[13] J. Duran, *Sand, powders, and grains. An introduction to the physics of granular materials* (Springer, New York, 2000).

[14] M.C. Cross, and P.C Hohenberg, *Pattern formation outside of equilibrium*, Rev. Mod. Phys. **65**, 851 (1993).

[15] D. van der Meer, J.P. van der Weele, and D. Lohse, *Coarsening dynamics in a vibrofluidized compartmentalized granular gas*, J. Stat. Mech.: Theor. Exp. P04004 (2004).

[16] E. van Doorn, R.P. Behringer, *Onset and evolution of a wavy instability in shaken sand*, Phys. Lett. A **235** 469-474 (1997).

[17] J. Duran, *Rayleigh-Taylor Instabilities in Thin Films of Tapped Powder*, Phys. Rev. Lett. **87**, 254301 (2001).

[18] S. Ergun, *Fluid flow through packed columns*, Chem. Engng. Proc. **48**, 89 (1952).

[19] N. Burtally, P.J. King, M.R. Swift, *Spontaneous Air-Driven Separation in Vertically Vibrated Fine Granular Mixtures*, Science **295**, 1877 (2002).

[20] C. Zeilstra, M.A. van der Hoef, and J.A.M. Kuipers, *Simulation study of air-induced segregation of equal-sized bronze and glass particles*, Phys. Rev. E **74**, 010302(R) (2006).

# 4

# Coarsening of Faraday heaps: Experiment, simulation, and theory[§]

*When a layer of granular material is vertically shaken, the surface spontaneously breaks up in small Faraday heaps that merge into larger ones on an ever increasing timescale. We study this coarsening process by means of a threefold approach combining experiment, simulations, and theory. The average lifetime of the transient state with $N$ Faraday heaps is shown to scale as $N^{-3}$ for coarsening in one dimension and $N^{-2}$ for coarsening in two dimensions.*

## 4.1 Introduction

When a bed of fine dry sand is vertically vibrated or tapped, its initially flat surface turns into a landscape of small heaps, which in the course of time coarsen into larger ones. This phenomenon, known as Faraday heaping, is one of the most celebrated and beautiful examples of the effect of air on granular matter [1–7] and in a broader context, provides a prime example of spontaneous pattern formation in a dynamical system far from equilibrium [8, 9].

The dynamic equilibrium of a single heap is well understood (see previous chapter): The outward avalanches in the upper layers are balanced by the inward motion of the deeper layers (induced by the airflow through the vibrating bed [5, 7]), and together they form the convective flow of particles known as Faraday circulation. By contrast, the merging of small

[§]Based on: H.J. van Gerner, Gabriel A. Caballero-Robledo, D. van der Meer, K. van der Weele, and M.A. van der Hoef, *Coarsening of Faraday Heaps: Experiment, Simulation, and Theory*, submitted to Phys. Rev. Lett.

H.J. van Gerner, D. van der Meer, K. van der Weele, and M.A. van der Hoef, *Coarsening in two dimensions of Faraday heaps*, to be submitted.

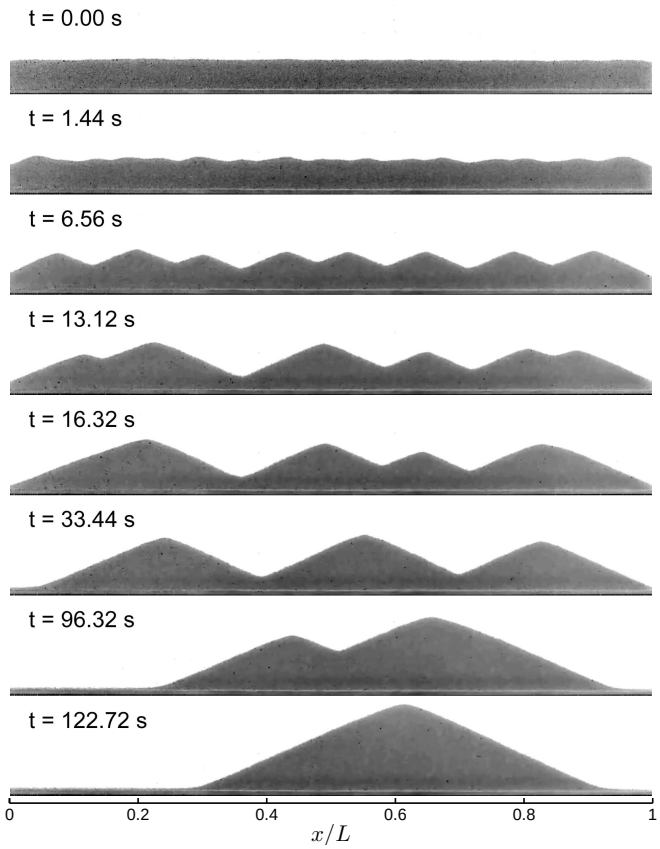


*Figure 4.1: Coarsening of a vertically vibrated 1D granular bed, as recorded in our experiments. It takes roughly two minutes to evolve from a flat landscape to a single Faraday heap. Every image is taken at the same point during the vibration cycle, when the container moves upward and the bed is pressed against the floor.*

heaps into larger ones - the coarsening process (see Fig. 4.1) - is much less understood, and quantitative experiments have been scarce [10, 11].

In the present study we introduce a new model for the coarsening behavior, validated by experiments and detailed numerical simulations. This threefold approach leads to the identification of the mean lifetime $\tau_N$ of the $N$-heap state as the proper coarsening quantity. It is proven to scale, in our 1D setup of Fig. 4.1, as $\tau_N \propto N^{-3}$ and as $\tau_N \propto N^{-2}$ in two dimensions.

## 4.2 Experiments

A glass box of dimensions $L \times H \times D = 300 \times 100 \times 2.1$ mm$^3$ is vertically vibrated using a sinusoidal driving with frequency $f = 6.25$ Hz and amplitude $a = 10$ mm. The box contains 19.44 grams of spherical glass particles ($\rho = 2500$ kg/m$^3$) with average diameter $d = 0.5$ mm (and an approximate Gaussian size distribution with $\sigma = 0.055$ mm), i.e., the height of the granular bed in rest is about 31 particle diameters. The above choice of parameters means that we operate at a dimensionless acceleration $\Gamma = a(2\pi f)^2/g = 1.6$, so that the bed detaches from the vibrating bottom during part of the driving cycle [12]. This is necessary, since the heaping effect relies on the air flowing into (and out of) the void between bed and bottom, with the bed acting as a porous piston [7]. In addition, the dimensionless energy input $E = (a2\pi f)^2/(gd) = \Gamma a/d$ must be sufficiently high in order to sustain the convective circulation of grains within the heaps [7, 10]. Our choice of $a/d = 20$ gives $E = 36$, which lies well above the required threshold value of $E \approx 2.0 + 1.26a/d = 27$ [10] and thus guarantees a smooth coarsening process.

Where Fig. 4.1 shows snapshots from a typical experimental run, Fig. 4.2(a) contains the time evolution for a second run. In order to get sufficient statistics to determine the mean lifetime of the $N$-heap state, 19 runs were performed. Figure 4.3 shows the number of heaps $N(t)$ (a decreasing step function) for all 19 experiments [14]. The inset shows the averaged data on a log-log scale, suggesting that $N(t) \propto t^{-\beta}$ with $\beta$ close to 0.5. We do not find the exponential decay reported by Van Doorn and Behringer [10]. Presumably the exponential behavior is a critical case, since it was only observed in experiments for which the energy input $E$ was around the value that is minimally required for heaping. When $E$ exceeded this threshold, as in our case, also Van Doorn and Behringer found a clear deviation from exponential decay.

## 4.3 Numerical simulations

We also performed numerical simulations on the same system. Our code combines Granular Dynamics (GD) and Computational Fluid Dynamics (CFD) [13]: The GD part calculates the particle trajectories from Newton's law, with the particle-particle interactions being given by a 3D soft sphere collision model including tangential friction, while the CFD part evaluates the full Navier-Stokes equations for the interstitial air by a finite difference

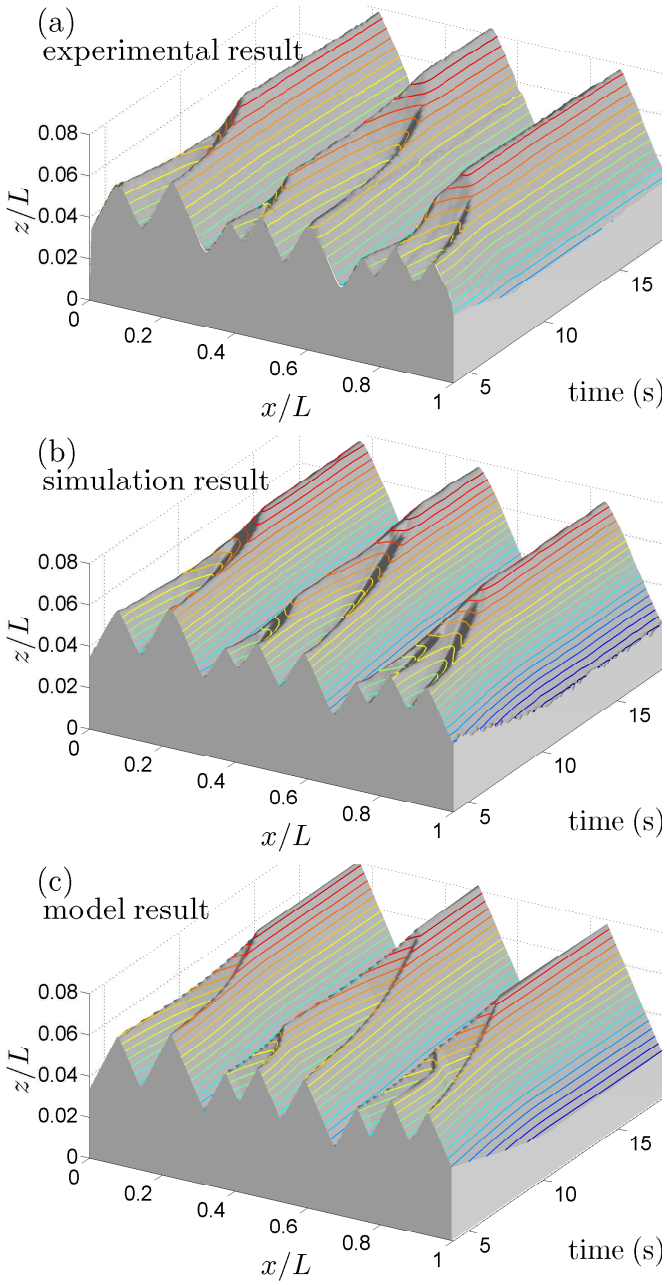


*Figure 4.2: Evolution of the heap pattern from $t = 4$ s to 18 s obtained by (a) experiment, (b) simulation, and (c) the analytical model. A stroboscopic video of the evolving heap pattern as obtained by experiment, simulation, and model can be found on the enclosed CD-ROM.*

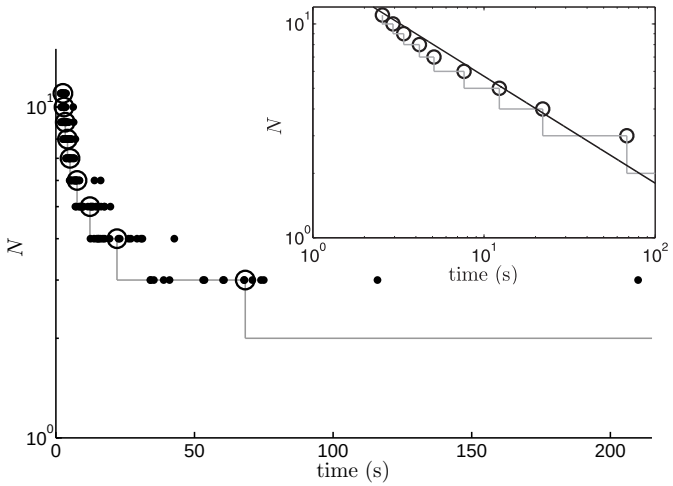


*Figure 4.3: Experiment: Number of heaps N as a function of time. The black dots are the measured times when the $N$-heap state gives way to the $(N-1)$-state; the open circles represent the average over all 19 experimental runs. No data for $N = 2$ are shown [14]. Inset: The averaged data on a doubly logarithmic scale. The solid line represents the approximate scaling behavior $N(t) \propto t^{-1/2}$.*

method. The two parts of the code are coupled to account for the effect of the air on the particles, and vice versa. The position and height of the peaks at $t = 4$ s in the experiment of Fig. 4.2(a) are used to create the starting condition for the numerical simulation [Fig. 4.2(b)]. The excellent correspondence confirms that any unwanted side-effects in the experimental setup (due to e.g. misalignment, humidity, or static electricity, none of which are present in the numerical code) have been successfully kept to a minimum. Apart from the heap patterns, the simulations can provide detailed information that cannot be readily obtained from the experiments (such as the location of isobars and the data shown in Fig. 4.7), and which will presently be used in setting up the analytical model.

## 4.4 Analytical model

Our aim is to derive equations for the time evolution of the position $x_i(t)$ and height $z_i(t)$ of a typical heap (see Fig. 4.4), which are then combined to determine the evolution of the whole system. A first observation, and a key ingredient of our model, is that the slope angle is the same for all

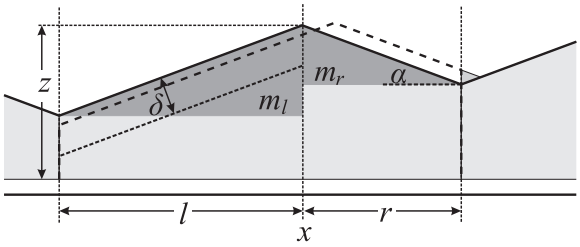


*Figure 4.4: Part of a typical heap pattern, indicating the key parameters used in the coarsening model. The dashed profile indicates the position of the heap after one time step* d$t$.

heaps and remains constant during the entire coarsening process; see Fig. 4.1 and Fig. 4.2(a,b). At this angle, which in our experiments has the value $\alpha = 18.5°$, the inward particle flux and the avalanching precisely balance each other [7].

A second observation (from the simulations) is that when the bed detaches from the vibrating plate, the lines of constant air pressure run parallel to the slopes just below the surface [7] whereas deeper inside the heap, the equal pressure lines flatten out. This means that below a certain depth $h$ the horizontal component of the air drag becomes negligible and thus the total horizontal drag force $F_x$ on the left part of the heap scales with the slope length $l$. This force acts during a small fraction of the driving cycle $\delta t_1$ (see Fig. 4(a) in [7]) and as a result, the particles in the left dark grey triangle in Fig. 4.4 (representing a mass $m_l \propto l^2$) are set in motion. Analogously, for the right side of the heap the force is proportional to $r$ and will be in the negative $x$-direction. As a result the total effective mass ($\propto l^2 + r^2$) acquires a horizontal velocity $u_x \propto \delta t_1 \ (l-r)/(l^2+r^2)$. This velocity is maintained during a considerable fraction of the vibration cycle $\delta t_2$, until the heap collides again with the vibrating plate (see Fig. 4(b) in [7]). So during the period of each vibration cycle, $\Delta t = 1/f$, the top of the heap will be displaced over a distance $\Delta x = u_x \delta t_2$. Since $\delta t_1$ and $\delta t_2$ do not change during a single realization of the experiment, the time rate of change of the horizontal position $x$ of the top of the heap (on a timescale much larger than the duration of a cycle) is thus given by

$$\frac{\mathrm{d}x}{\mathrm{d}t} = C\frac{l-r}{l^2+r^2}\ , \tag{4.1}$$

with $C$ a constant that can be determined from experimental or simu-

lation data. For this we calculate $\mathrm{d}x/\mathrm{d}t$, by differentiating the polynomials that are obtained by fitting curves through the peak position data [Fig. 4.6(a)], and $(l-r)/(l^2+r^2)$ [Fig. 4.6(b)] for all heaps as a function of time. Most of the combined data of these figures collapses on a straight line (Fig. 4.7) where the value for $C$ is determined by the slope of this line. The scatter in Fig. 4.7 can be contributed to the error margin of approximately one particle diameter in the determination of the peak location.

To derive an analogous equation for the change of the heap height $z$, we note that the mass in a heap remains the same - in good approximation - from one cycle to the next. This is because the main flow of material is directed away from the valleys, towards the center of each heap, so there is hardly any mass being exchanged through the vertical lines at the valley positions. Thus the total area contained in a heap at time $t$, $A(t) = z(l+r) - \frac{1}{2}\tan\alpha\ (l^2+r^2)$, will still be the same at time $t+\Delta t$, indicated by the dashed profile in Fig. 4.4. Setting $A(t) = A(t+\Delta t)$ [the latter with $z \to z+\Delta z$, $l \to l+\Delta x$, and $r \to r-\Delta x$], we obtain in the limit of $\Delta x, \Delta z \to 0$ the desired equation for the height $z$:

$$\frac{\mathrm{d}z}{\mathrm{d}t} = \tan\alpha\,\frac{l-r}{l+r}\,\frac{\mathrm{d}x}{\mathrm{d}t} = C\frac{\tan\alpha\ (l-r)^2}{(l+r)(l^2+r^2)}\,. \tag{4.2}$$

To complete the model, we use the fact that in each cycle, after the heap has shifted, avalanches relax the slope angles to the value $\alpha$ again. This leads to a relocation of the $i$-th valley (between peak $\{x_i, z_i\}$ and $\{x_{i+1}, z_{i+1}\}$) such that its horizontal position $\check{x}_i$ is given by

$$\check{x}_i = \frac{1}{2}(x_{i+1}-x_i) - \frac{1}{2\tan\alpha}(z_{i+1}-z_i)\,. \tag{4.3}$$

The change of area due to this relocation of the valleys (equal to the area of the small grey triangle in Fig. 4.4) is of second order in $\mathrm{d}x$ and therefore in $\mathrm{d}t$. It thus vanishes in the limit $\mathrm{d}t \to 0$ and the total mass in the system is conserved.

The model contains one parameter $C$, which sets the absolute timescale of the coarsening process. It depends on particle size and density, gravity, and viscosity (see Eq. (1) in [7]), as well as on the vibration parameters $\Gamma$ and $a/d$, keeping pace with the Faraday circulation velocity (see Fig. 9(b) in [7]). However, in a single realization of the experiment, $C$ is simply a constant and its value can be determined as in Fig. 4.7. With $C$ given, one can numerically solve the model equations; we use the experimental peak

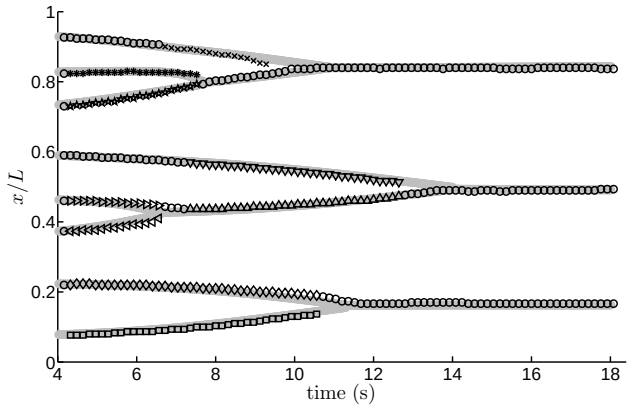


*Figure 4.5: Evolution of the heap pattern. The black markers represent the simulation result, the grey lines represent the result from the analytical model (see Fig. 4.2(a,b)).*

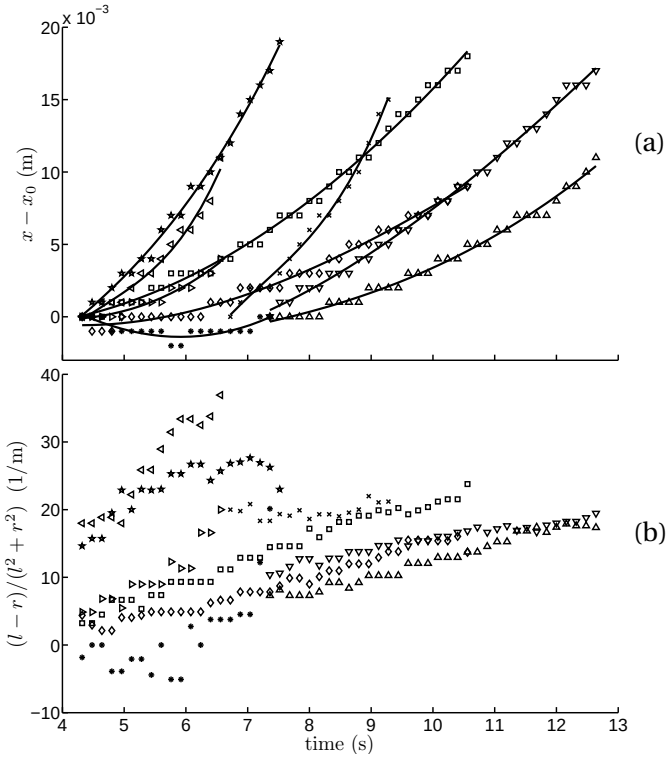


*Figure 4.6: Data used to determine the value for C: (a) Position of the peaks in Fig 4.5 minus their initial position. The fitted curves are used to calculate the horizontal velocity of the peaks,* $\mathrm{d}x/\mathrm{d}t$. *(b) The quantity* $(l-r)/(l^2+r^2)$ *as a function of time.*

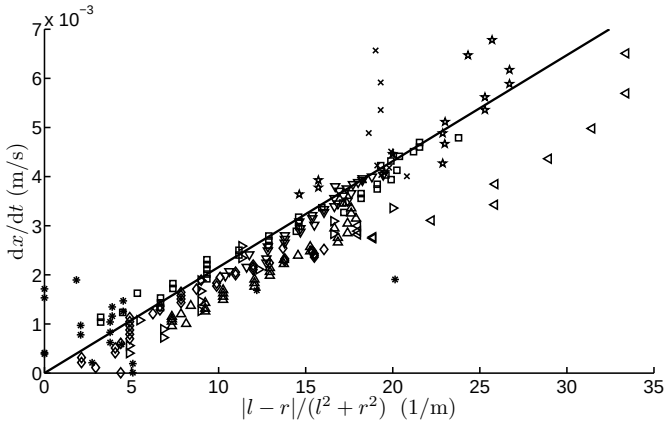


*Figure 4.7: Validation of Eq. (4.1) from the simulation results in Fig. 4.2(b). The slope of the fitted line gives the factor* $C = 0.2\ 10^{-3}\ m^2/s$. *The data in this figure are taken from the eight heaps in Fig. 4.5, with each heap being indicated by a different marker.*

positions $x_i(t), z_i(t)$ at $t = 4$ s to define our initial condition. The solution [Fig. 4.2(c)] is seen to match the experimental and simulated patterns very well. Hence we conclude that the essential features of the process are accurately captured by our model.

## 4.5 Mean lifetime of the N-heap state

The model is ideally suited to study the scaling behavior of the coarsening process. It allows us to start with an arbitrarily large number of heaps (which in experiment would require a forbiddingly long box) and moreover, to perform thousands of different realizations to improve the statistics. In Fig. 4.8 we show the mean lifetime $\tau_N$ of the $N$-heap state; the black circles represent the average over $10,000$ runs of the model, each run starting out from $N = 100$ heaps with slope lengths that are uniformly distributed between $0$ and $L/100$*. We see a clear power-law scaling over the full two decades of $N$, namely $\tau_N \propto N^{-3}$, and once more an excellent agreement between model and experiment in the final decade $N = 10, ..., 3$. The inset of Fig. 4.8 shows that the average number of heaps

*If we start from a narrow distribution of heaps, the initial mean lifetimes are larger than predicted by the power-law, but soon the distribution broadens and the lifetimes $\tau_N$ converge to the straight line of Fig. 4.8.

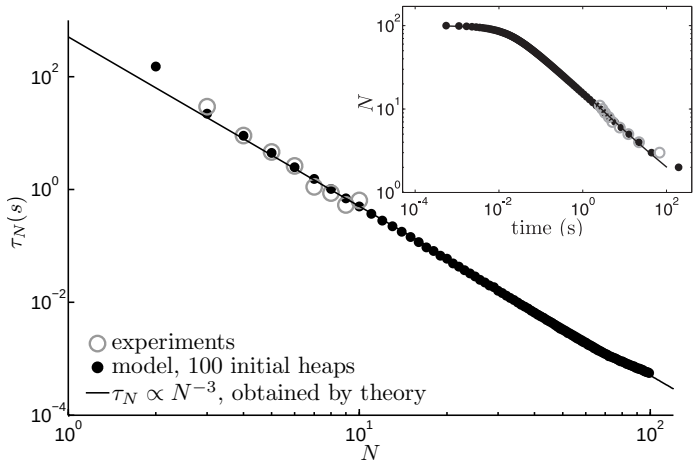


*Figure 4.8: Mean life time of the $N$ heap state $\tau_N$ as a function of the number of heaps $N$. The grey circles indicate the experimental data. The black circles indicate the data averaged over $10,000$ runs of the model starting with $100$ initial heaps. Inset: Number of heaps as a function of time (cf. Fig. 4.3).*

as a function of time $[N(t)]$ does *not* exhibit global power-law scaling. So not $N(t)$, but $\tau_N$ is the natural quantity to analyze from a theoretical point of view.

## 4.6 Explanation of the scaling law

How does $\tau_N \propto N^{-3}$ follow from the model? To answer this, we rewrite Eqs. (4.1)-(4.3) in terms of the previously introduced left and right slope lengths $l_i = x_i - \check{x}_{i-1}$ and $r_i = \check{x}_i - x_i$. After some algebra this leads to

$$\begin{cases} \mathrm{d}l_i/\mathrm{d}t = f(l_i, r_i) - f(l_{i-1}, r_{-1}) \,, \\ \\ \mathrm{d}r_i/\mathrm{d}t = f(r_i, l_i) - f(r_{i+1}, l_{i+1}) \,, \end{cases} \tag{4.4}$$

where the function $f$ is given by

$$f(u,v) = C\frac{u(u-v)}{(u^2+v^2)(u+v)} \,. \tag{4.5}$$

These equations can be non-dimensionalized as follows: We divide all lengths $l_i$ and $r_i$ by the average slope length in the $N$-heap state ($= L/2N$, in the absence of depletion effects [14]): $\widetilde{l}_i = 2l_iN/L$ and $\widetilde{r}_i = 2r_iN/L$.

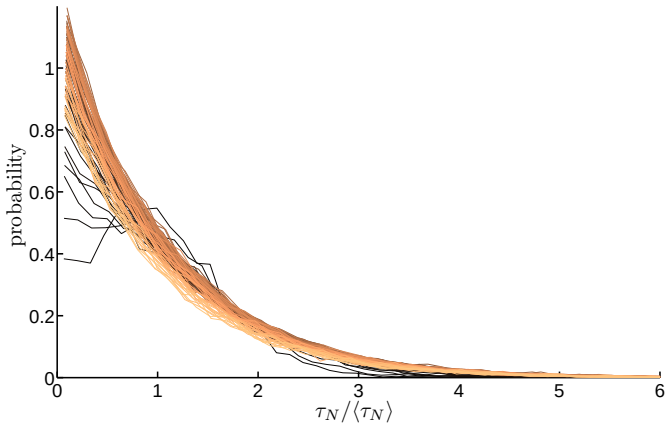


*Figure 4.9: Distribution of $\tau_N$ (normalized by the averaged lifetime) obtained in the 10,000 runs of the model, for $N = 100$ (light) to $N = 3$ (dark). The probability function clearly shows an exponential distribution.*

Further, we make the function $f$ dimensionless by dividing through $C$ (so $\widetilde{f} = f/C$), and arrive at

$$\frac{\mathrm{d}\widetilde{l}_i}{\mathrm{d}\widetilde{t}} = \widetilde{f}(\widetilde{l}_i, \widetilde{r}_i) - \widetilde{f}(\widetilde{l}_{i-1}, \widetilde{r}_{i-1}), \quad \text{and similarly for } \mathrm{d}\widetilde{r}_i/\mathrm{d}\widetilde{t}, \tag{4.6}$$

in which the dimensionless time coordinate $\widetilde{t}$ must be defined as $\widetilde{t} = 4N^2Ct/L^2$.

Now we focus on a single heap $i$ in a $N$-heap state ($i = 1, .., N$) and compute its time-evolution with Eq. (4.6) until it merges with one of its two neighbors. This yields a dimensionless life expectancy $\widetilde{T}_i$ of the heap, which can subsequently be translated to its dimensional value: $T_i = \widetilde{T}_i L^2/(4CN^2)$. So the life expectancy of an arbitrary heap in the $N$-heap state scales as $1/N^2$, and the same will hold for the average life expectancy $T_{\mathrm{av}}(N)$. This average life expectancy is not the mean lifetime $\tau_N$, since the first heap that merges already terminates the $N$-heap state. Therefore, $\tau_N$ is the *shortest* of the $N$ life expectancies, ensemble-averaged over many realizations. When $N$ is not too small, the merging events can be considered as statistically independent, from which follows that the life expectancy $T_i$ of a heap $i$ obeys an exponential distribution: $P(T_i) = P(0)e^{-T_i/T_{\mathrm{av}}}$. This is indeed confirmed by direct evaluation of the model (see Fig. 4.9). A property of this distribution is that the average minimum

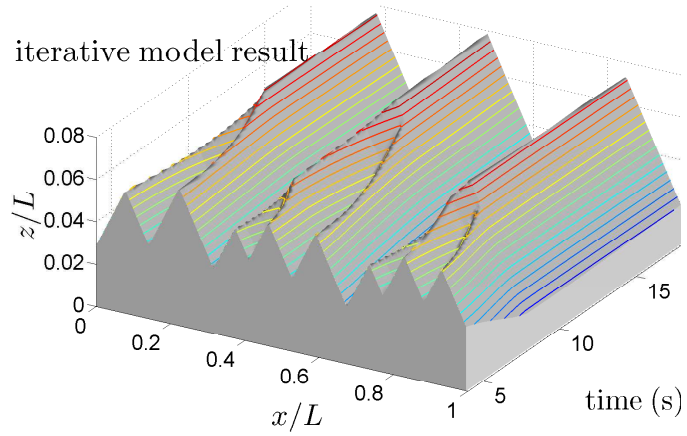


*Figure 4.10: Evolution of the heap pattern obtained by the iterative model.*

value of $T_i$ (alias $\tau_N$) decreases with the sample length $N$ as $T_{\mathrm{av}}(N)/N$. Inserting $T_{\mathrm{av}}(N) \propto 1/N^2$ gives $\tau_N \propto N^{-3}$, which explains the observed scaling behavior.

The above analysis also shows that, for the current problem, $N(t)$ is a more intricate quantity than $\tau_N$: The total elapsed time $t(N)$ at the end of the $N$-heap state is the cumulative sum of all $\tau_{N'}$ with $N' \geq N$. Nevertheless, for small $N$ we still find an approximate scaling law, since

$$t(N) = \sum_{N'=N}^{N_{\mathrm{init}}} \tau_{N'} \approx \int_N^{N_{\mathrm{init}}} \tau_{N'} \mathrm{d}N' \propto \int_N^{N_{\mathrm{init}}} \frac{\mathrm{d}N'}{N'^3} \,, \tag{4.7}$$

so that $t(N)$ scales as $N^{-2}$ for $N \ll N_{\mathrm{init}}$ or vice versa, $N(t) \propto t^{-1/2}$. This is the behavior found in Fig. 4.3, as well as in the data for small $N$ in the inset of Fig. 4.8.

## 4.7 Alternative calculation of the heap height

Close inspection of Fig. 4.2 teaches us that there is a small difference between the heap pattern obtained by the model and the one obtained by experiment or simulation: In the model, a small heap merges at the peak of a large heap, and the area contained by the small heap slightly increases near the merging event. However, in the experiments and simulations, the small heap merges into the slope of the large heap and the area contained by the small heap remains approximately constant. This difference is

due to the assumption in the model that no mass is being exchanged through the vertical lines through the valleys. This assumption is not entirely accurate near merging events: If one heap is much larger than the other, the isobars underneath the valley are not horizontal, which results in a small but noticeable mass flow from the small to the large heap. For this reason, we also worked with a modified model in which $\mathrm{d}z/\mathrm{d}t$ is not calculated by Eq. (4.2), but by an iterative procedure where the area in the individual heaps is kept constant in time (except in case of a merging event, when the mass of the merging heaps is summed). Figure 4.10 shows the evolution of the heaping pattern obtained with the modified model. The agreement with the experiment and simulation is now even better; the small heaps merge into the slopes of the large heaps in experiment, simulation *and* model.

## 4.8 Heaping in 2D

We can extend the principles that we used to construct the one dimensional coarsening model to two dimensions. The change of the momentum in the $x$ direction of a small slice $\mathrm{d}\theta$ of the heap (see Fig 4.11) is proportional to the surface area of the slice ($\frac{1}{2}r_v^2\mathrm{d}\theta/\cos\alpha$, where $r_v(\theta)$ is the shortest distance between the intersection line and the axis of symmetry of the cone, see appendix B), multiplied by the value of the unit vector in the $x$-direction ($-\cos\theta$). The total change in momentum of the heaps in the $x$-direction is found by calculating the intersection lines with all the neighboring heaps and integrating the slice over one complete revolution. In order to obtain the change per unit time of the heap position, the total momentum has to be divided by the affected volume, which yields for the $x$-direction:

$$\frac{\mathrm{d}x}{\mathrm{d}t} = -C\frac{\int_0^{2\pi} r_v^2\cos\theta\mathrm{d}\theta}{\int_0^{2\pi} r_v^3\mathrm{d}\theta}\,, \tag{4.8}$$

and analogously for the $y$-direction:

$$\frac{\mathrm{d}y}{\mathrm{d}t} = -C\frac{\int_0^{2\pi} r_v^2\sin\theta\mathrm{d}\theta}{\int_0^{2\pi} r_v^3\mathrm{d}\theta}\,. \tag{4.9}$$

The derivation of an explicit relation for the change of height $z$ of the heaps [similar to Eq. (4.2)] is very difficult in two dimensions. However,

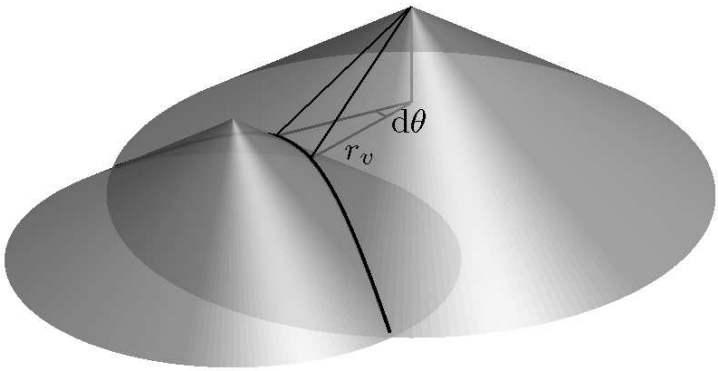


*Figure 4.11: Two cones representing two heaps. The intersection line between the cones is calculated in appendix B. In the 2D model, the intersection of a heap with all surrounding heaps is calculated first, after which the new position and height of the heaps can be calculated with Eqs. (4.8) and (4.9) under the constraint that the volumes of the heaps remain constant.*

we can use the same principle as in the modified 1D model, and calculate $\mathrm{d}z/\mathrm{d}t$ by an iterative procedure where the volume of the individual heaps $(\int_0^{2\pi}(h - r_v \tan\alpha)\frac{1}{2}r_v^2 \mathrm{d}\theta)$ is kept constant in time (except in case of a merging event, when the volume of the merging heaps is summed).

Figure 4.12(a-d) show a typical evolution of an initially flat bed obtained in an experiment by Shinbrot [11]. In the experiment, the heaps move towards each other (indicated by grey lines) until they merge. In Fig 4.12(d) it appears that the granular material in the box is almost depleted, i.e., a large amount of the particles has accumulated in the growing heaps, leaving not enough material to sustain the heaping mechanism around the heaps, which results in the flat bed around the collection of heaps.

In a numerical evaluation of the coarsening model, we start with an initial condition where the distance in the $x$ and $y$ direction between the peaks has an uniform distribution between 0.5 and $1.5\,L/\sqrt{N_0}$, with $L$ the dimension of the box and $N_0 = 49$ the initial number of heaps. The variation in the height of the peaks has an uniform distribution between $-0.05$ and $0.05\,L/\sqrt{N_0}$. Figure 4.12(e-h) show a typical evolution of the heaping pattern obtained by a numerical evaluation of the model. The same coarsening behavior is observed as in the experiment. In the model, the heaps will merge until only one heap remains.

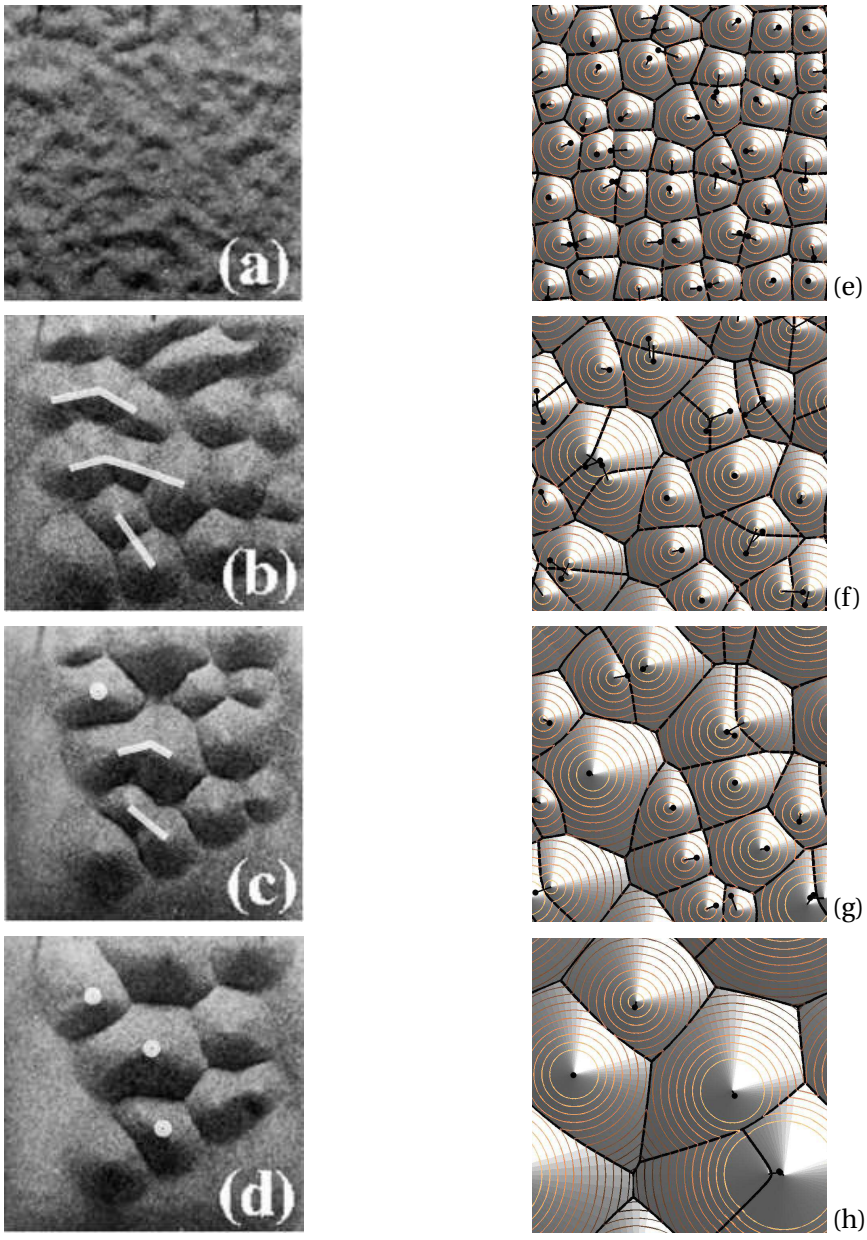


*Figure 4.12: Top view of coarsening in 2D obtained by experiment (a-d, images taken from Shinbrot [11]) and by the model (e-h). In the experiment, heaps move towards each other until they merge (indicated by the grey lines), just as in the model. The velocity and direction of the peaks in the model is indicated by the black lines originating from the peaks of the heaps. A video of the coarsening behavior obtained by the model can be found on the enclosed CD-ROM.*

To study the statistics of the 2D coarsening behavior, we carried out 100 evaluations of the model, each starting with 49 heaps. The black circles in Fig. 4.13 show the averaged life time as a function of the number of heaps $N$. It can be seen that the model predicts a clear algebraic scaling, with the mean life time of the $N$ heap state $\tau_N$ being proportional to $N^{-2}$ (against $\tau_N \propto N^{-3}$ in the one dimensional model).

The difference between the exponents found in the 1D and 2D model can be understood as follows: In the 1D model, a dimensional analysis shows that the life expectancy of a heap scales with $1/N^2$. A similar dimensional analysis shows that the change in the dimensionless position of the peak in the 1D model $\mathrm{d}\widetilde{x}/\mathrm{d}t$, scales with $N^2$, i.e. the rate of change of the peak position is reversely proportional to the life expectancy of a heap.

For the 2D model, we normalize $x$ and $r_v$ in Eq. (4.8) with the averaged heap radius $L/2\sqrt{N}$, yielding:

$$\frac{\mathrm{d}\widetilde{x}}{\mathrm{d}t} = -C\frac{\int_0^{2\pi}\widetilde{r}_v^2\cos\theta\mathrm{d}\theta}{\int_0^{2\pi}\widetilde{r}_v^3\mathrm{d}\theta}\frac{4N}{L^2}\,. \tag{4.10}$$

That is, the change in the dimensionless position of the peak in the 2D model $\mathrm{d}\widetilde{x}/\mathrm{d}t$ scales linearly with $N$. The average life expectancy of a heap in 2D will therefore scale as $1/N$ and, since the life times of the heaps have an exponential distribution, the shortest life expectancy (alias $\tau_N$) scales as $1/N$ times the average life expectancy (see section 4.6), For this reason, $\tau_N \propto N^{-2}$.

## 4.9 Conclusion

The essence of the coarsening of Faraday heaps, a complex dynamical process involving not only many particles but also the interaction with the ambient air, has been captured in a simple system of differential equations. The model gives results that are in excellent quantitative agreement with both the experiment and simulations. Combining the three approaches, we have shown that $\tau_N$, the mean lifetime of the $N$-heap state, scales as $N^{-3}$ in a one dimensional system and as $N^{-2}$ in a two dimensional system.

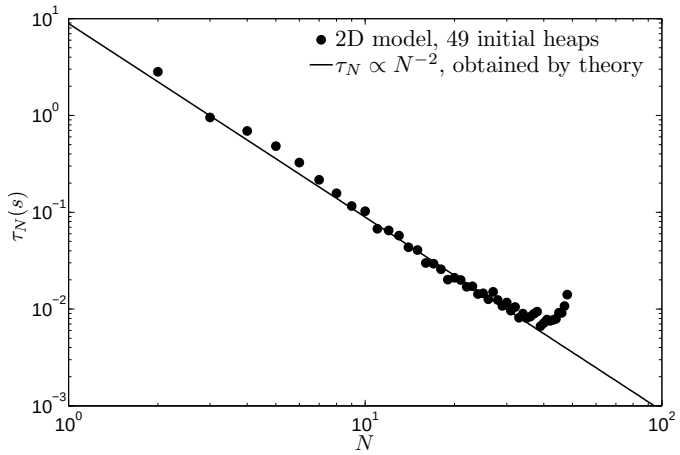


*Figure 4.13: Coarsening in two dimensions: Mean life time of the $N$ heap state $\tau_N$ as a function of the number of heaps $N$. The black circles indicate the data averaged over 100 runs of the model starting with 49 initial heaps. The black line is the theocratically predicted scaling behavior.*

# Appendix A: Distribution of slope lengths

In the numerical evaluation of the model discussed previously, the dimensionless slope lengths, $\widetilde{l}_{\mathrm{i}}$ and $\widetilde{r}_{\mathrm{i}}$, have an uniform distribution as initial condition. Naturally, the initial distribution of the slope lengths has an influence on the coarsening behavior; for example, in the extreme case where the slope lengths are all equal, no coarsening takes place at all. For this reason, we experimented with using different distributions. Fig. 4.14 shows the mean lifetime of the $N$ heap state for different distributions of the initial slope lengths. Around $N = 100$, the lifetime obtained by a normal distributed initial condition is larger than the lifetime which is obtained by an uniform distributed initial condition, since the probability of a small slope (which is usually short lived) is small in a normal distribution. However, after a number of merging events, the coarsening dynamics broadens the distribution and the differences in lifetimes disappear. For a very sharply peaked normal distribution ($\sigma = 0.01$), the mean lifetime first oscillates around $\tau_N \propto N^{-3}$ (see grey crosses in Fig. 4.14), before showing the same coarsening behavior as with the other distributions.

Clearly, the distribution of the slope lengths changes during the coarsening process. To investigate this, we count the number of slopes in

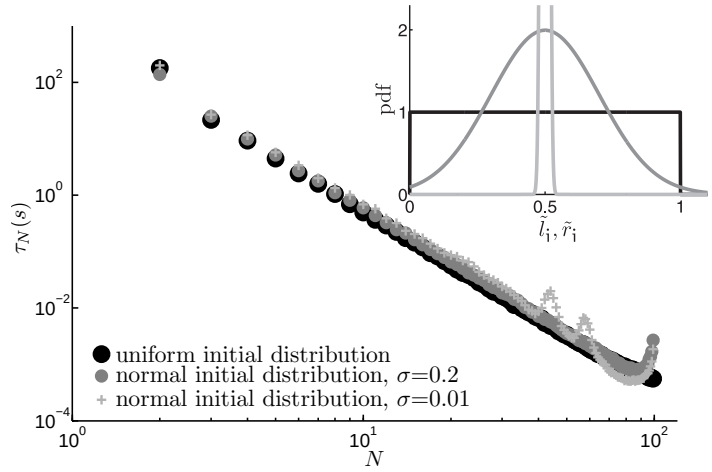


*Figure 4.14: Mean life time of the $N$ heap state $\tau_N$ as a function of the number of heaps $N$ with an uniform (black circles) and normal distributions (grey circles for $\sigma = 0.2$, grey crosses for $\sigma = 0.01$) of the initial slope lengths. The same coarsening behavior is obtained with all three initial conditions. Inset: The three initial distribution of the dimensionless slope lengths.*

48 equally sized bins (with length 0.025 $L/2N(t)$) after each merging event for all 10,000 runs of the model. Figure 4.15 shows the resulting normalized histograms as a function of the number of heaps. Initially, the slope lengths have the specified distribution, uniform in (a) and normal ($\sigma = 0.2$) in (b). However, already after a few merging events the distribution changes noticeably until, eventually, one heap remains with a normalized slope length of $1/2$. Although there is a huge variation from the initial ($N = 100$) to the final ($N = 1$) distribution, the coarsening behavior is the same during the whole coarsening process.

## Appendix B: Intersection between two cones

In this appendix, the intersection line of two cones is calculated in polar coordinates ($x = r\cos\theta,\ y = r\sin\theta$). The implicit cartesian equation for a cone with index $i$ is given by:

$$(x - x_i)^2 + (y - y_i)^2 = \frac{(z - h_i)^2}{\tan^2\alpha} \ . \tag{4.11}$$

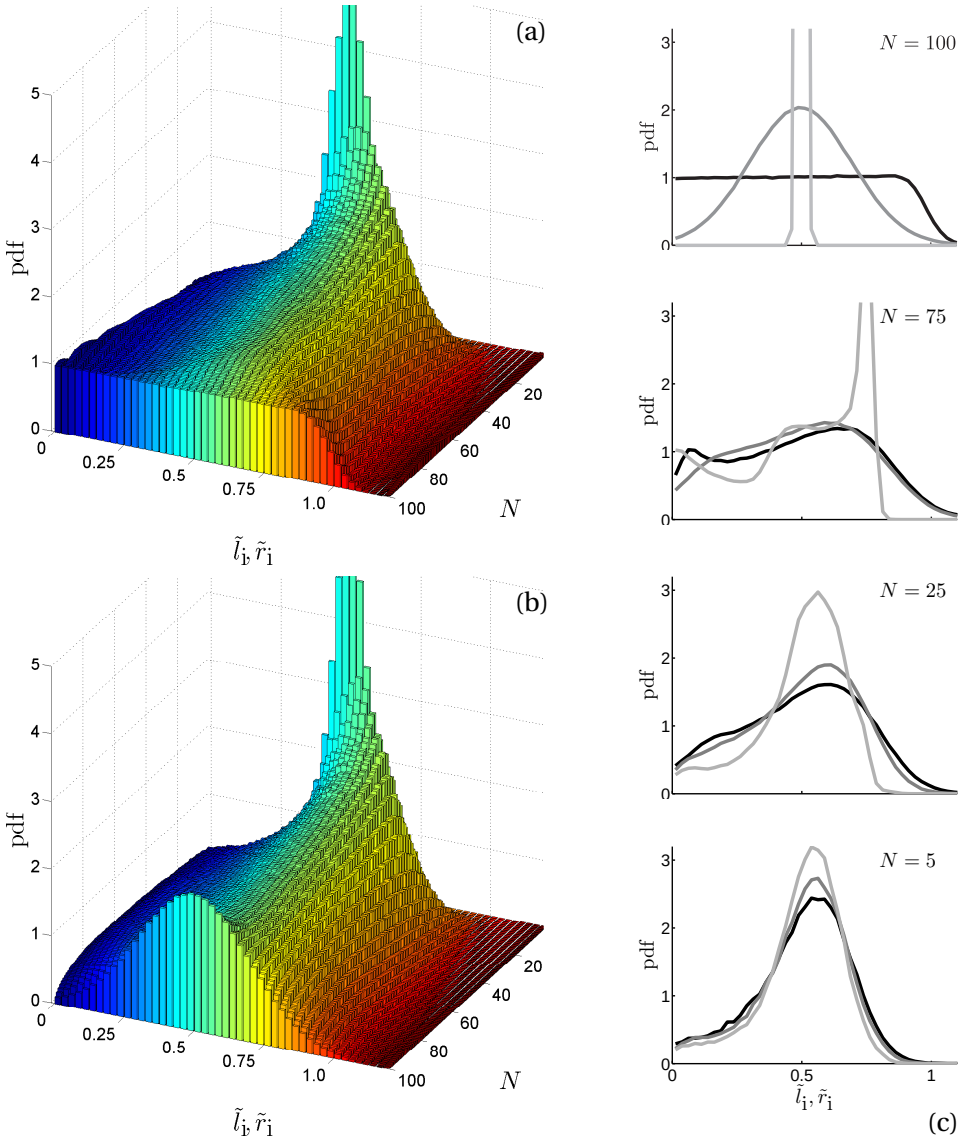


*Figure 4.15: Probability distribution function for the normalized slope lengths (defined immediately after a merging event0 as a function of the number of heaps. The data is averaged over 10,000 runs of the model. Initially, the slope lengths have the specified distribution, uniform in (a) and normal ($\sigma = 0.2$) in (b), however already after a few merging events, the distributions changes until eventually, one heap remains with a normalized slope length of $1/2$. (c) The distributions for all three initial conditions (uniform and normal with $\sigma = 0.2$ and $\sigma = 0.01$, respectively) for N=100, 75, 25, and 5.*

The equation for the first cone in polar coordinates with origin at $x_1, y_1$ is then simply:

$$r^2 = \frac{(z-h_1)^2}{\tan^2\alpha} \,, \tag{4.12}$$

and the equation for the second cone in polar coordinates with origin at $x_1, y_1$ is:

$$r^2 + r_{12}^2 - 2r\, r_{12}\cos(\theta-\theta_{12}) = \frac{(z-h_2)^2}{\tan^2\alpha} \,, \tag{4.13}$$

where $r_{12}$ and $\theta_{12}$ are the distance and angle between the origins of the first and second cone. Solving Eq. (4.12) for $z$ and substituting this result in Eq. (4.13) yields:

$$r^2 + r_{12}^2 - 2r\, r_{12}\cos(\theta-\theta_{12}) - (r + \frac{h_1}{\tan\alpha} - \frac{h_2}{\tan\alpha})^2 = 0 \,. \tag{4.14}$$

This implicit equation can be solved numerically for $r$ and $\theta$ by using the 'contourc' command in Matlab, which yields the intersection line between the two cones. The calculation of the shortest distance between the axis of symmetry of a cone and the intersection line, $r_v$ as a function of $\theta$, is then straightforward.

## References

[1] M. Faraday, *On a peculiar class of acoustical figures; and on certain Forms assumed by groups of particles upon vibrating elastic surfaces*, Phil. Trans. R. Soc. London **121**, 299 (1831).

[2] C. Laroche, S. Douady, and S. Fauve, *Convective Flow of granular masses under vertical vibrations*, J. Phys. **50**, 699 (1989).

[3] H.K. Pak, E. van Doorn, and R.P. Behringer, *Effects of Ambient Gases on Granular Materials under Vertical Vibration*, Phys. Rev. Lett. **74**, 4643 (1995).

[4] H.M. Jaeger, S.R. Nagel, and R.P. Behringer, *Granular solids, liquids, and gases* , Rev. Mod. Phys. **68**, 1259 (1996).

[5] B. Thomas and A.M. Squires, *Support for Faraday's View of Circulation in a Fine-Powder Chladni Heap*, Phys. Rev. Lett. **81**, 574 (1998).

[6] R.P. Behringer, E. van Doorn, R.R. Hartley, and H.K. Pak, *Making a rough place "plane": why heaping of vertically shaken sand must stop at low pressures*, Gran. Matter **4**, 9 (2002).

[7] H.J. van Gerner, M.A. van der Hoef, D. van der Meer and K. van der Weele, *Interplay of air and sand: Faraday heaping unravelled*, Phys. Rev. E **76**, 051305 (2007).

[8] M.C. Cross, and P.C. Hohenberg, *Pattern formation outside of equilibrium*, Rev. Mod. Phys. **65**, 851 (1993).

[9] I.S. Aranson and L.S. Tsimring, *Patterns and collective behavior in granular media: Theoretical concepts*, Rev. Mod. Phys. **78**, 641 (2006).

[10] E. van Doorn, R.P. Behringer, *Onset and evolution of a wavy instability in shaken sand*, Phys. Lett. A **235** 469-474 (1997).

[11] T. Shinbrot, *Granular coarsening*, Gran. Matter **1**, 145 (1998).

[12] P. Eshuis, K. van der Weele, D. van der Meer, R. Bos, and D. Lohse, *Phase diagram of vertically shaken granular matter*, Phys. Fluids **19**, 123301 (2007).

[13] M.A. van der Hoef, M. Ye, M. van Sint Annaland, A.T. Andrews IV, S. Sundaresan, and J.A.M. Kuipers, *Multi-Scale Modeling of Gas-Fluidized Beds*, Adv. Chem. Eng. **31**, 65 (2006).

[14] Note that in our experiments the box becomes depleted towards the end of the coarsening process, so that there are areas where hardly any material is present anymore, either in between the heaps or at the sides of the system (as seen in Fig. 4.1). We only considered data free of depletion effects, which means that for $N \leq 2$ no experimental measurements were used at all.

# 5

# Air-induced inverse Chladni patterns[§]

*When very light particles are sprinkled on a horizontal resonating plate, inverse Chladni patterns are formed. Instead of going to the nodal lines of the plate (and forming a regular Chladni pattern), the particles are dragged to the anti-nodes since the motion of the ambient air averaged over one cycle is non-zero. Although the Eulerian mean velocity is directed to the nodal lines directly above the plate, the more relevant Lagrangian mean velocity is directed to the anti-nodes.*

## 5.1 Introduction

A classic way of visualizing two-dimensional standing waves is by sprinkling coarse particles (sand) on a horizontal plate and bring it into resonance by e.g. a violin bow. The particles will move to the nodal lines, giving rise to the famous Chladni patterns, a standard high school demonstration experiment [1–3]. The technique was developed by Ernst Chladni in 1787 who actually became quite famous with his experiment and toured extensively throughout Europe. In 1809, he was invited to perform the experiment for Napoleon, who was so pleased with it, that he awarded Chladni 6000 francs. Napoleon also promised 3000 francs to anyone who could provide the mathematical theory for the sound figures. This sum was awarded to Sophie Germain in 1816 [2].

Much less known is that very fine particles will move to the *anti-nodes*: This was already noted by Chladni himself, who observed that tiny hair shavings from his violin bow were carried to the anti-nodes. In 1831, the effect was studied systematically by Faraday with the use of lycopodium powder [4]. He and others showed that the inverse Chladni patterning of

[§]Based on: H.J. van Gerner, D. van der Meer, K. van der Weele, and M.A. van der Hoef, *Air-induced inverse Chladni patterns*, to be submitted.

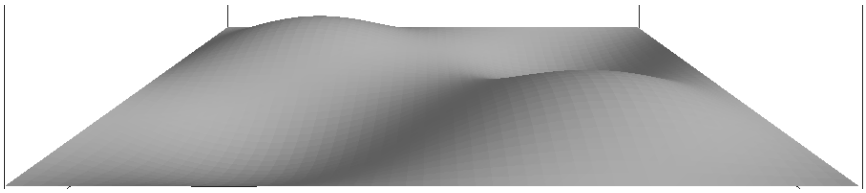

*Figure 5.1: Side view of the flexible plate resonating in its 2 × 2 mode. The vertical dimension is exaggerated 40 times.*

fine particles is due to air currents induced by the vibrating plate [4–6], dragging along the fine particles to the anti-nodes*. The mathematical explanation for these air currents was first provided by Lord Rayleigh in 1884 [7] and is often referred to as Rayleigh or (since much of the early research was concerned with air currents induced by sound waves) acoustic streaming. However, this last term is less appropriate for the particular streaming that causes the inverse Chladni patterns since here the compressibility of the air plays no significant role. We therefore use the term 'steady streaming' instead [8].

Pattern formation on a flexible plate is a prime example of "Newton vs Stokes": the Newtonian forces tend to form Chladni patterns while the Stokesian forces tend to form inverse Chladni patterns. In this chapter, we present direct numerical simulations which provide us with a detailed physical picture of the interplay of the air and particles on a Chladni plate.

## 5.2 Numerical model

The simulated system consists of a flexible rectangular plate ($40 \times 40\,\mathrm{mm}^2$) on which $80,000$ beads with a diameter $d = 0.075$ mm are uniformly distributed. At a height $H = 2$ mm above the flexible plate, a rigid cover plate is mounted. The plate is flexible and pinned along its outer rim. We excite the $2 \times 2$ natural mode of this plate. Ignoring the additional bending of the plate due to gravity, the vertical deflection at any point $(x, y)$ is then given by (see also Fig. 5.1):

$$z(x,y,t) = -a\cos(\omega t)\,\sin\frac{2\pi x}{L}\,\sin\frac{2\pi y}{L}\,, \tag{5.1}$$

*When enough particles have collected at the anti-nodes and the shaking strength is not too large, Faraday heaps as described in the previous two chapters are formed at each of the anti-nodes [4].

where $\omega = 2\pi f = 2\pi\ 200\ \mathrm{s}^{-1}$ is the natural frequency of the plate, $a = 0.075$ mm the amplitude of the vibration (corresponding to a dimensionless acceleration $\Gamma = a\omega^2/g = 12.1$), and $L = 40\ \mathrm{mm}$ the size of the plate. Note that the height of the cover $H$ (2 mm) is one order of magnitude larger than the thickness of the boundary layer $\delta \approx \sqrt{2\nu/\omega} = 0.17$ mm, with $\nu$ the kinematic viscosity. This is sufficiently large to model the streaming which takes place within and just above the boundary layer.

For the simulation we use the hybrid Granular Dynamics (GD) Computational Fluid Dynamics (CFD) code described in chapter 2. The GD code calculates the particle trajectories from Newton's law, with the particle-particle interactions being given by a 3D soft sphere collision model including tangential friction. The CFD code evaluates the full Navier-Stokes equations by a finite difference method. For the interaction between the vibrating plate and the gas phase, the immersed boundary method with 10 iterations is used (see section 2.6.2). The simulated system is divided in 60 CFD cells along each side of the plate, and 110 cells in the vertical direction in order to accurately capture the boundary layer above the plate. The time step used for the flow solver is $5 \cdot 10^{-5}$ s, so that there are 100 time steps per vibration cycle. Since the particles only have a small influence on the gas flow above the vibrating plate (due to the low particle volume fraction), we use one-way coupling, i.e., the flow field is calculated for one vibration cycle (without particles present) and subsequently used for all vibration cycles[†]. The flow field of the air above the flexible plate at time $t = 0.25\ T$ (where $T$ is the time of one vibration cycle) is shown in Fig. 2.5. Note that a similar velocity profile is obtained at $t = 0.75\ T$, with the signs of $u_x$ and $u_y$ (the horizontal velocity components of the air) reversed, i.e., the air moves to-and-fro between the anti-nodes. At the vertical walls, periodic boundary conditions are used.

The drag force on a particles can be approximated by Stokes' law[‡]:

$$\mathbf{F}_{\mathrm{drag}} = 3\pi\mu_g d\left(\mathbf{u} - \mathbf{v}\right)\ , \tag{5.2}$$

where $\mu_g$ is the dynamic gas viscosity, $\mathbf{u}$ is the local flow velocity of the gas phase and $\mathbf{v}$ is the velocity of the particle. The ratio of the (typical) drag

[†]It is possible to calculate the flow field during all vibration cycles and include the interaction with the particles. However, this would lead to extremely long CPU times and the results would be very similar.

[‡]The hydrodynamic interaction with the surrounding particles [9] can be neglected because of the low particle concentration, while the history forces [10] can be neglected since $d/\sqrt{\nu/\omega} < 1$, with $\nu$ the kinematic viscosity of air.

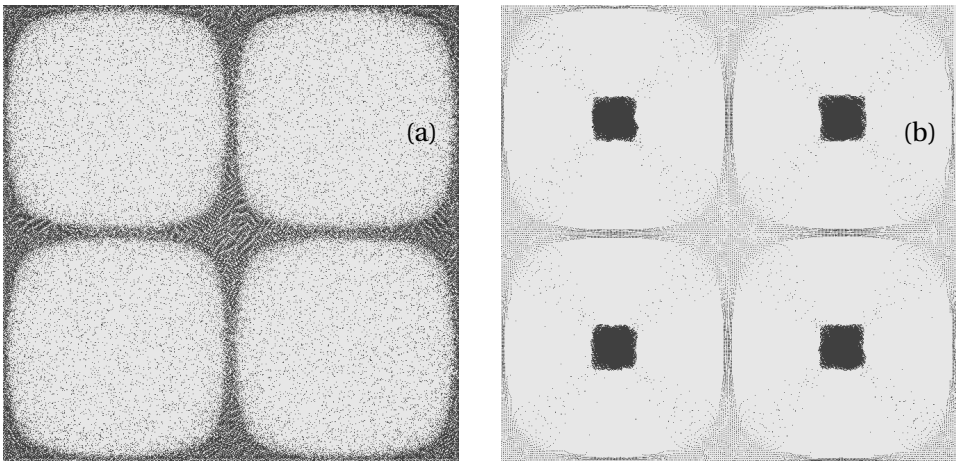


*Figure 5.2: (a) Top view of a flexible plate resonating in its 2 × 2 mode on which heavy particles have been sprinkled. After a few seconds most particles have collected at the nodal lines, forming a classic Chladni pattern. (b) The same plate with very light particles. Due to the presence of air, the particles now migrate to the anti-nodes and after 4 seconds an inverse Chladni pattern has formed. Videos of the formation of regular and inverse Chladni patterns can be found on the enclosed CD-ROM.*

force and gravity on a particle is then:

$$B = \frac{\mathbf{F}_{\text{drag}}}{\mathbf{F}_g} = \frac{3\pi\mu_g d\,(\mathbf{u}-\mathbf{v})}{\rho\pi g d^3/6} \approx \frac{18\mu_g\, a\omega}{\rho g d^2}\,. \tag{5.3}$$

If a simulation is carried out with gold beads ($\rho = 20000$ kg/m$^3$), the ratio $B$ is around 0.03, i.e., the motion of the particles is governed by the Newtonian forces. Because of the oscillations of the plate, the particles start to bounce and (since in most cases a bouncing particle impacts on a section of the plate while it is moving upward) the successive bounces tend to increase their kinetic energy. However, at the nodal lines the plate has a zero velocity and the collisions with the plate and other particles reduce the kinetic energy of the particles. As a result, starting with all 80,000 particles uniformly distributed over the plate, within a few seconds most of them have accumulated at the nodal lines, forming a standard Chladni pattern [Fig. 5.2(a)].

We now reduce the density of the particles to 20 kg/m$^3$ while keeping the diameter constant, resulting in a typical drag force that is almost thirty times larger than the gravitational force on the particle, i.e., $B \approx 30$.

This value is approximately the same as for lycopodium powder ($\rho = 460\,\mathrm{kg/m^3}$, diameter $d \approx 0.016\,\mathrm{mm}$ [11]), which was used by Faraday in his experiments [4]. As can be seen in Fig. 5.2(b), these light particles move to the anti-nodes and form an inverse Chladni pattern[§].

Evidently, since the motion of the particles is governed by the Stokesian forces, the particles do not bounce on the resonating plate. Furthermore, the ratio between the particle response time, $\rho d^2/(18\mu_g)$ [12] and the typical vibration time $T$ is 0.07, so the particles follow the motion of the gas. The physical reason for the inverse Chladni patterning is that the to-and-fro motion of the gas averaged over one cycle is not zero. This counter-intuitive fact is explained in the next section.

## 5.3 Steady streaming

It is a curious but well-known fact that geometries that move sinusoidal, may generate a flow field that is not simply sinusoidal: In addition to (and as a result of) the to-and-fro motion of the gas, there is a steady streaming near the surface of vibrating boundaries [7, 8, 13, 14]. What is the physical explanation for this phenomenon[¶]?

At $t = 0\ T$, the plate has zero velocity and maximum acceleration. The plate accelerates the gas near the surface and the momentum of the gas is subsequently passed to the higher layers of the fluid. After $t = 0.25\ T$, the plate decelerates and the gradient of the horizontal velocity in the boundary layer becomes smaller. This sequence repeats itself half a cycle later ($t = 0.5\ T$), but now in the opposite direction, as indicated in Fig. 5.3(a). In this figure, the velocity at a point on a nodal line ($x = L/2$, $y = L/4$) is shown at two time instants during the first half of a cycle (grey lines) and at two time instants during the second half of a cycle (black lines). Clearly, the velocities during both halves of a cycle cancel each other and the averaged velocity is zero at this location. The situation is different however, half way between an anti-node and a nodal line ($x = 3/8\ L$ and $y = L/4$), as shown in Fig. 5.3(b). Here, the plate is *not* at the same position during the acceleration phase of the first and the second half cycle. As a result, the averaged velocity over one cycle does not vanish, and a steady streaming occurs [blue line in Fig. 5.3(b)].

[§]Regular and inverse patterns formed on a flexible plate that is pinned in the middle and excited at different modes can be seen on the front cover.

[¶]For a short mathematical description of steady streaming, see appendix A.

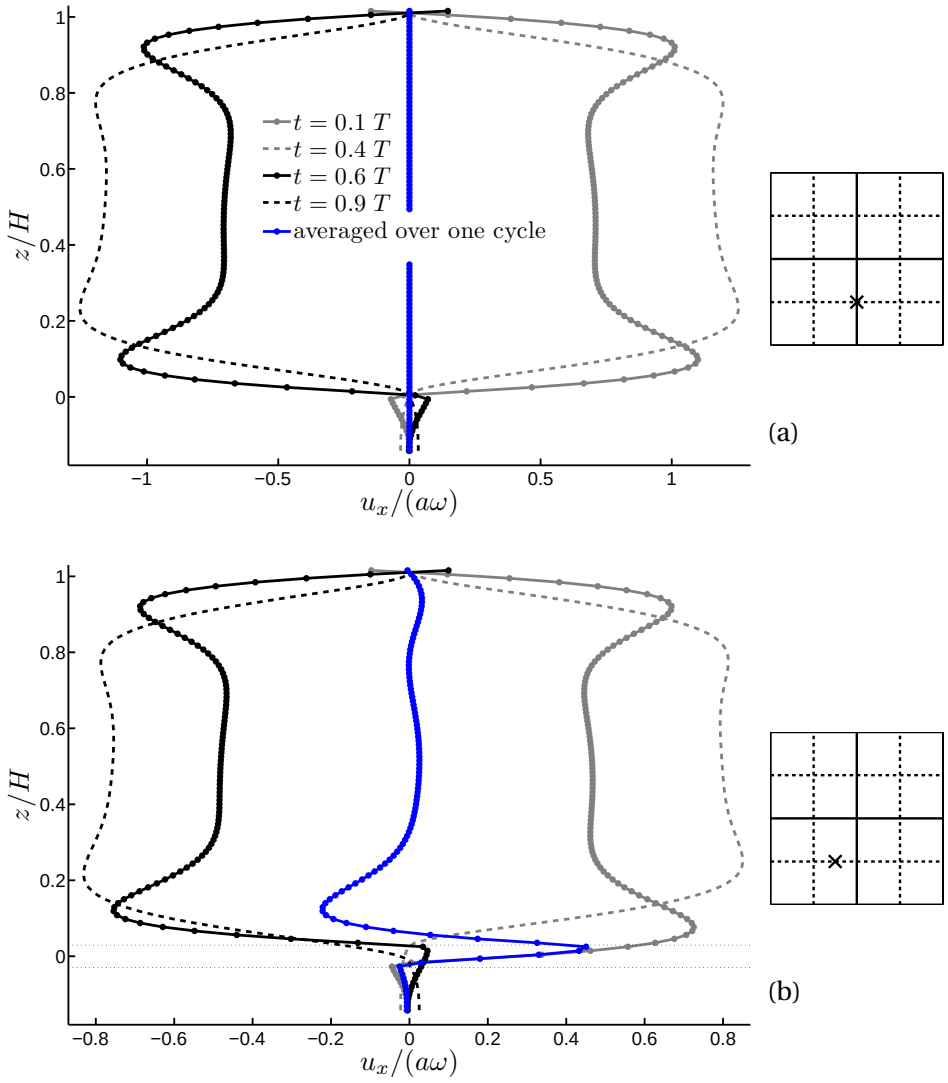


*Figure 5.3: Velocity as a function of the height at two time instants during the first half of a cycle (grey lines) and at two time instants during the second half of a cycle (black lines), at two different locations on the plate (see insets): (a) At a nodal line ($x = L/2$ and $y = L/4$), and (b) at halfway between an anti-node and nodal line ($x = 3/8\ L$ and $y = L/4$). The blue line represents the amplitude of the average velocity over the complete vibration cycle (multiplied by a factor of five for clarity). At location (a) the blue line does not deviate from zero. At location (b) there is steady streaming (blue line deviates from zero).*

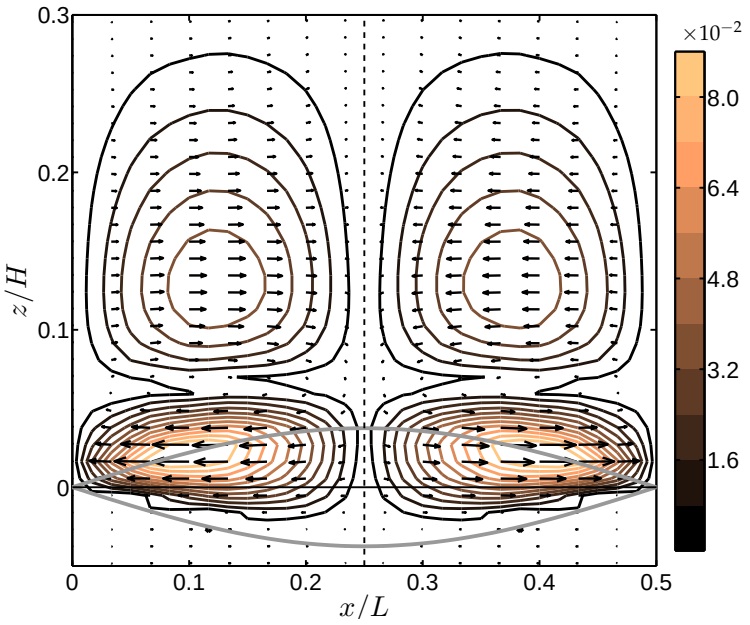


*Figure 5.4: Cross section of the time-averaged Eulerian velocities at $y = L/4$. The vertical dashed line marks the position of the anti-node at $x = L/4$. The grey lines indicate the location of the plate at maximum deflection. The magnitude of the averaged velocity is indicated by the colored lines while the direction is indicated with arrows.*

Figure 5.4 shows a vertical cross section of the steady streaming velocities at $y = L/4$ for $0 < x < L/2$. At the nodal lines ($x = 0,\ L/2$) and anti-nodes ($x = L/4$) the velocity is zero, while in between, the velocity is directed towards the nodal lines for $z < 0.100$ mm ($z/H < 0.05$) and towards the anti-nodes above this height. The particles have a diameter of $d = 0.075$ mm and for this reason one would expect the particles to move to the nodal lines. In the simulation [see Fig. 5.2(b)] however, we find that the opposite occurs: The particles move to the anti-nodes. To understand this, we have to make the distinction between the Eulerian and Lagrangian mean velocity of the gas. The Eulerian mean velocity is the averaged velocity at a point that is fixed in space. This is the velocity that would be measured by a probe located at a certain height, averaged over one cycle. In contrast, the Lagrangian mean velocity is the averaged velocity of a particle that moves with the fluid. This is the mean velocity that would be obtained by releasing very light tracer particles above the resonating plate.

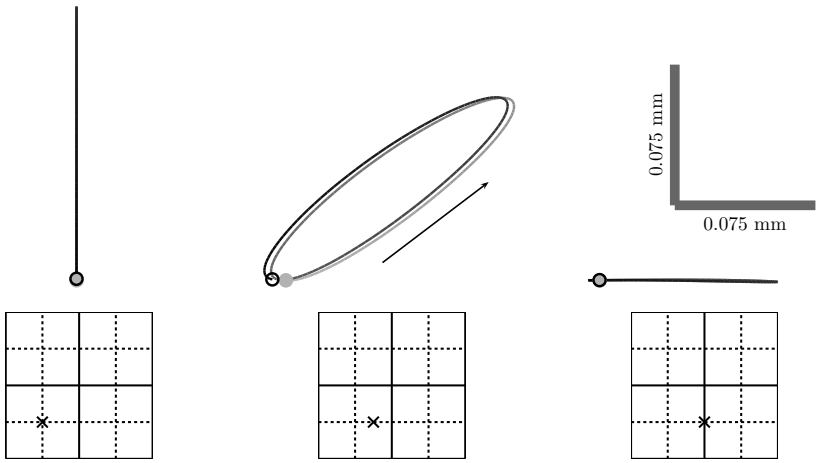


*Figure 5.5: Path in the $xz$-plane of a fluid particle during two vibration cycles at an anti-node, between an anti-node and a nodal line, and at a nodal line, respectively. The initial position of the fluid particles (indicated with the filled grey circles) is 0.0375 mm above the plate. The position of the fluid particle between the anti-node and nodal line has moved to the anti-node after two cycles (indicated by the black circle). Note that the maximum vertical displacement of the fluid particle at the anti-node is twice the vibration amplitude (0.15 mm).*

The Eulerian mean velocity is most commonly used in describing steady streaming [6, 15, 16] since the Lagrangian mean velocity is in general much more difficult to obtain in an analysis. In this study, the Lagrangian mean velocity is however the more appropriate one since the ratio $B$ for the particles that form inverse Chladni patterns is larger than unity (in our case, $B = 30$) and the Stokesian forces dominate, i.e. the particles follow the motion of the fluid and act like tracer particles. To illustrate the importance of the Lagrangian mean velocity, we show in Fig. 5.5 the trajectories of three *fluid* particles at a height of $d/2$ =0.0375 mm ($z/H = 0.019$) above the resonating plate (i.e., the same height as the centers of most *granular* particles) during a time span of two vibration cycles. At the anti-node, the fluid particle moves up and down while at the nodal line, the fluid particle moves from left to right. In both cases, the fluid particles have the same position after two vibration cycles. In between the anti-node and nodal line however, the fluid particle has moved to the left i.e., to the *anti-node*, whereas the mean Eulerian velocity is directed to the *nodal line* at this location (see Fig. 5.4).

A difference in Eulerian and Lagrangian velocities may occur in all

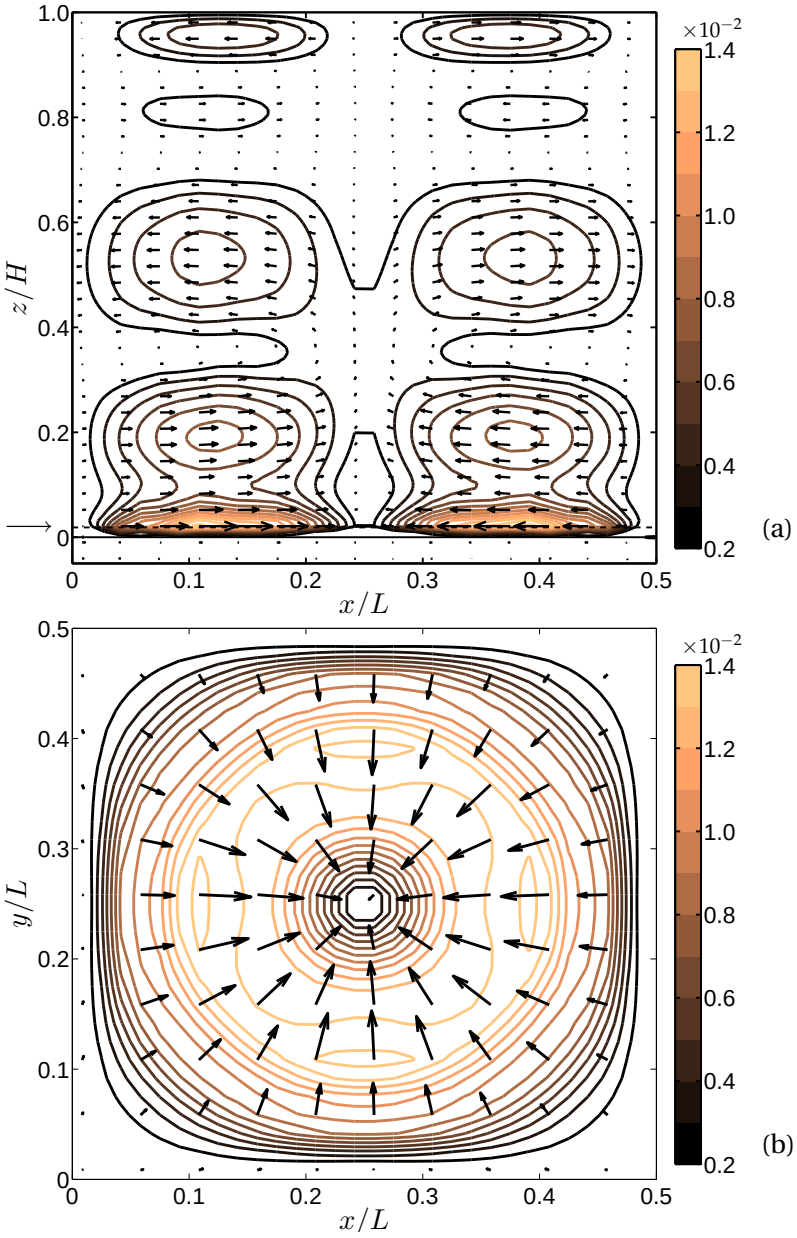


*Figure 5.6: (a) Cross section of the time-averaged Lagrangian velocities at* $y = L/4$. *The magnitude of the averaged velocity is indicated by the colored lines while the direction is indicated with arrows. (b) Cross section of the time-averaged Lagrangian velocities of one quarter of the vibrating plate at* $z = d/2 = 0.0375$ *mm* $[z/H = 0.019$, *indicated by the arrow in (a)].*

oscillatory flows which are inhomogeneous in space and is often referred to as the Stokes drift. This term arises from Stokes' derivation of the expressions that describe the net motion of a small particle near the free surface of water waves (its Lagrangian velocity), in the direction of the wave propagation [17]. Lighthill was one of the first to recognize the difference between the Eulerian and Lagrangian velocities in steady streaming [14]. However, in the case he studied, where the streaming was caused by a standing soundwave, the difference between the two types of velocities was considerably smaller than the steady streaming velocity itself. In our case, where the streaming is caused by the resonating plate, the difference is much larger and the directions of the Eulerian and Lagrangian velocities are even *opposite*.

We can determine the Lagrangian mean velocity by subtracting the initial position of a fluid particle, anywhere on the vibrating plate, from its position after one vibration cycle (and dividing by the time $T$)[‖]. Figure 5.6(a) shows a vertical cross section of the Lagrangian streaming velocities at $y = L/4$ for $0 < x < L/2$. The mean velocity is directed towards the anti-nodes for $z < 0.7$ mm ($z/H < 0.35$). Figure 5.6(b) shows the corresponding horizontal cross section of the time-averaged velocities of one quarter of the vibrating plate at height of half of the particle diameter $z = 0.075/2$ mm ($z/H = 0.019$) i.e., the height where most particles are. The inverse Chladni patterns of fine particles are formed as a result of this mean Lagrangian streaming.

Interestingly, Dorrestijn *et al.* [6] found in experiments that nanobeads (with a diameter of 0.5 $\mu$m) can move to the nodal lines of a cantilever beam resonating in water, thus forming a *regular* Chladni pattern. At first sight, this seems to contradict our own findings. In their setup however, Dorrestijn *et al.* use a frequency of 0.5 MHz and a vibration amplitude ($a \approx 0.02$ $\mu$m) that is much smaller than the thickness of the boundary layer ($\delta \approx \sqrt{2\nu/\omega} = 0.8$ $\mu$m, with $\nu$ the kinematic viscosity of water), whereas in our system (and in most Chladni plate experiments) the ratio between the vibration amplitude and boundary layer thickness is of order one. Presumably, the vertical displacement of the plate only plays a minor role in the experiments of Dorrestijn *et al.* and the induced streaming is more reminiscent of acoustic streaming.

In acoustic streaming, two layers of vortices can be identified [7, 18, 19]: Vortices inside the boundary layer (inner circulation) and vortices

[‖] In this case, we begin a vibration cycle at $t = 0.25\ T$, when the plate has no deflection.

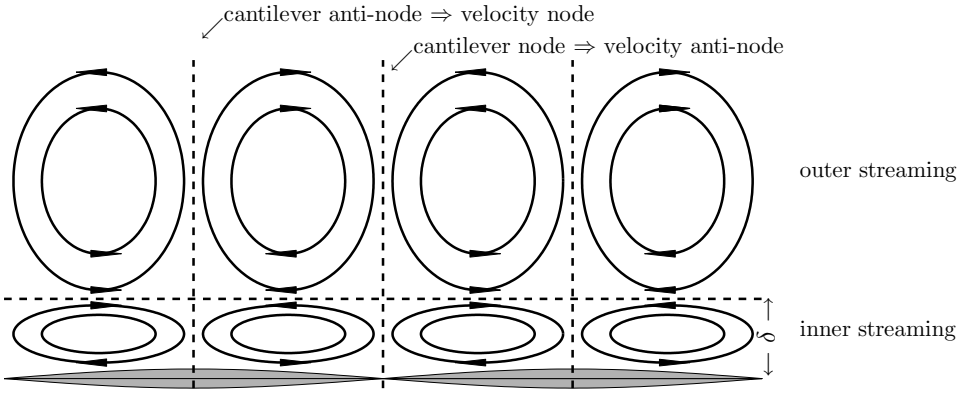


*Figure 5.7: Sketch of the supposed streaming pattern as a result of a cantilever beam which resonates with very small amplitude. The vertical vibration of the beam results in an instantaneous horizontal velocity of the medium which is zero at the anti-nodes of the beam and maximal at the nodes (see also Fig. 2.5). For this reason, the velocity nodes are located at the anti-nodes of the beam and vice versa.*

outside the boundary layer (outer circulation), which have an opposite direction of rotation (see Fig. 5.7). The nanobeads in the experiments of Dorrestijn *et al.*, which are smaller than the thickness of the boundary layer, can be dragged by the inner circulation to the nodal lines of the cantilever beam. Particles that are larger than $\delta$ will move to the anti-nodes due to the outer circulation, in agreement with the observation of Dorrestijn *et al.* [6]. They provide an explanation similar as the one described above, but in their analysis, the inner circulation should be confined to the region of vibration, see Fig. 5 in [15], while in our explanation, the inner circulation is confined to the boundary layer. Since the vibration amplitude in their experiment ($\approx 0.02\ \mu$m) is much smaller than the diameter of the nanobeads ($0.5\ \mu$m), the inner circulation used in the analysis of Dorrestijn *et al.* cannot drive the nanobeads to the nodes.

## 5.4 Concluding remarks

In this chapter we have studied the formation of Chladni patterns on a resonating plate by direct numerical simulations, including the flow of the ambient air. To briefly summarize our main findings, we show in Fig. 5.8 the complete transition between inverse patterning and regular patterning. When the Stokesian forces dominate [$B > 1$, see Eq. (5.3)], the particles are driven to the anti-nodes [Fig. 5.8(a)]. The reason for

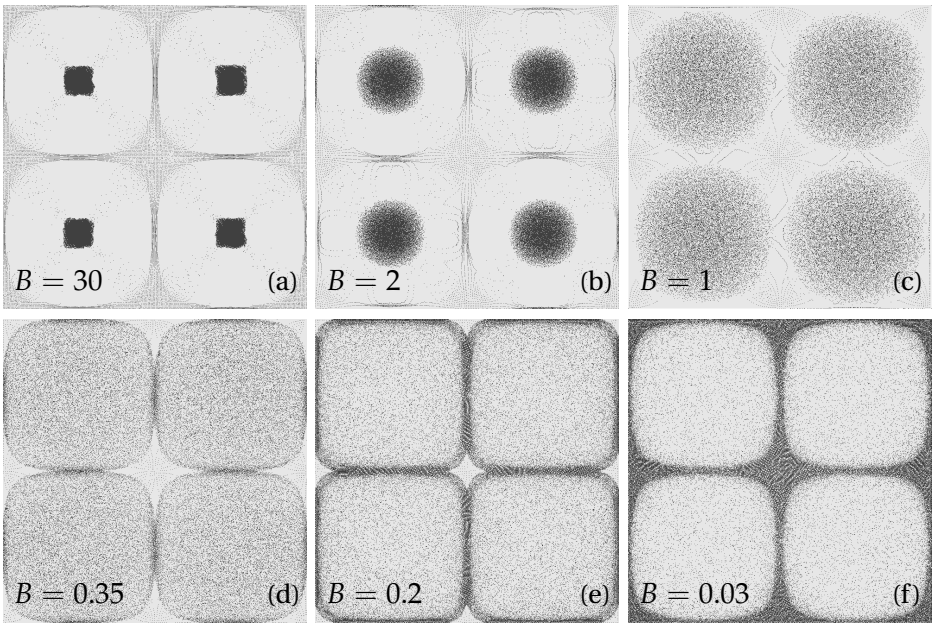


*Figure 5.8: Particles on a resonating plate where $B$ is varied [see Eq. (5.3)] by modifying the particle density. (a) The Stokesian forces dominate and an inverse Chladni pattern is formed. (b,c,d,e) For decreasing values of $B$, we see a gradual transition towards a regular Chladni pattern. In (c) the ratio of the typical drag force and gravity is around unity ($\rho = 550$ kg/m$^3$) and the Newtonian and Stokesian forces balance each other. As a result, the particles neither accumulate at the anti-nodes, nor at the nodal lines. (f) Finally for $B = 0.03$, the resulting pattern is clearly Newtonian dominated.*

this is that the motion of the ambient air averaged over one cycle is non-zero. In particular, the very light particles behave like tracer particles and follow the motion of the air; their motion is appropriately described by the Lagrangian streaming velocity of the air over the resonating plate. Interestingly, Eulerian streaming would give a result that contradicts experiments and simulation. The streaming phenomenon that causes the inverse Chladni patterns is a striking example of a physical system in which the Lagrangian velocity field proves to be more relevant than the Eulerian one.

When we slowly increase the density of the particles (with 0.1% per vibration cycle, allowing the system to adjust itself to the new condition), the Newtonian forces become more important and the particles start to bounce, forming clouds around the anti-nodes that become larger as

the density increases [Fig. 5.8(b)]. Around $B = 1$ the Newtonian and Stokesian forces are equally strong, and the clouds cover almost the entire plate [Fig. 5.8(c)]. When the density is increased further, the Newtonian forces dominate ($B < 1$), resulting in the regular Chladni pattern with the particles accumulated at the nodal lines [Fig. 5.8(f)].

## Appendix A: Mathematical description of streaming

In this appendix, we give a short mathematical description of the steady streaming. For this, we use the momentum equation for the gas phase:

$$\frac{\partial\left(\rho_g \mathbf{u}\right)}{\partial t} + \nabla \cdot \rho_g \mathbf{u}\mathbf{u} = -\nabla p - \nabla \cdot \boldsymbol{\tau} \,, \tag{5.4}$$

where $p$ is the gas phase pressure, $\rho_g$ the density of the gas phase (which we assume to be constant), $\boldsymbol{\tau}$ the viscous stress tensor and $\mathbf{u}$ is the flow velocity of the gas phase. We now approximate the velocity and the pressure by a harmonic velocity and pressure (with a zero average over time), plus a time-independent correction, representing the steady streaming:

$$\mathbf{u} = \mathbf{u}^H + \mathbf{u}^S \,,\; p = p^H + p^S \,. \tag{5.5}$$

Substituting the harmonic and streaming velocity into Eq. (5.4) and averaging over one vibration cycle yields (note that $\langle \mathbf{u}^H \rangle = 0$, but $\langle \mathbf{u}^H \mathbf{u}^H \rangle \neq 0$):

$$\nabla \cdot \rho_g \mathbf{u}^S \mathbf{u}^S = -\nabla p^S - \nabla \cdot \boldsymbol{\tau}^S - \langle \nabla \cdot \rho_g \mathbf{u}^H \mathbf{u}^H \rangle \,, \tag{5.6}$$

where the brackets indicate a time averaging over one vibration cycle. As in turbulence modelling, the last term in the equation is commonly called Reynolds stress [20]. This Reynolds stress drives the steady streaming. The Reynolds stress in $x$-direction at $y = L/4$ is equal to $\partial(u_x^2)/\partial x + \partial(u_x u_z)/\partial z$. The second term is large in the boundary layer when there is a large velocity in both the $x$-, and $z$-direction. For this reason, the steady streaming is much stronger near the vibrating plate than higher up near the cover plate (where the velocity in $z$-direction is practically zero). To obtain a analytical solution for Eq. (5.6), one begins by finding a solution for $\mathbf{u}^H$ and then substitutes this solution into Eq. (5.6) [13, 15]. Although the Lagrangian velocity field is more relevant, most studies only calculate the Eulerian velocity field [6, 8, 13, 15] or the streaming induced by a standing sound wave [14]. Finding the solutions for Eq. (5.6) is far

from trivial in a 3D system like ours and we limit ourselves to the flow fields obtained in the simulations.

## References

[1] H.-J. Stöckmann, *Ein Nomade der Wissenschaft*, Physik Journal **5**, 47 (November 2006).

[2] H.-J. Stöckmann, *Chladni meets Napoleon*, Eur. Phys. J. Special Topics **145**, 15 (2007).

[3] E.F.F. Chladni, *Die Akustik* (Breitkopf&Härtel, Leipzig, 1802); *Traité d'Acoustique* (Courcier, Paris, 1809).

[4] M. Faraday, *On a Peculiar Class of Acoustical Figures; and on Certain Forms Assumed by Groups of Particles upon Vibrating Elastic Surfaces*, Phil. Trans. R. Soc. London **121**, 299 (1831).

[5] M.D. Waller, *Air circulations about a vibrating plate*, Br. J. Appl. Phys. **6**, 347-348 (1955).

[6] M. Dorrestijn, A. Bietsch, T. Açikalin, A. Raman, M. Hegner, E. Meyer, and Ch. Gerber, *Chladni Figures Revisited Based on Nanomechanics*, Phys. Rev. Lett. **98**, 026102 (2007).

[7] Lord Rayleigh, *On the Circulation of Air Observed in Kundt's Tubes, and on Some Allied Acoustical Problems*, Phil. Trans. R. Soc. London **175**, 1 (1884); *The Theory of Sound Vol. II*, (Macmillan, London, 1896).

[8] N. Riley, *Steady streaming*, Annu. Rev. Fluid Mech. **33**, 43 (2001).

[9] S. Ergun, *Fluid flow through packed columns*, Chem. Engng. Progs. **48**, p. 89 (1954).

[10] M. Maxey and J. Riley, *Equation of motion for a small rigid sphere in a nonuniform flow*, Phys. Fluids **26**, 883 (1983).

[11] S. Banerjee and S.E. Law, *Characterization of chargeability of biological particulates by triboelectrification*, IEEE Trans. **IA-34** 6, 1201 (1998).

[12] S. Elghobashi, *On predicting particle-laden turbulent flows*, Appl. Sci. Res. **52**, 309 (1994).

[13] W.L. Nyborg, *Acoustic Streaming due to Attenuated Plane Waves*, J. Acoust. Soc. Am. **25**, 68 (1953).

[14] J. Lighthill, *Acoustic streaming*, J. Sound Vib. **61**, 391 (1978).

[15] T. Açikalin, A. Raman, and S. V. Garimella, *Two-dimensional streaming flows induced by resonating, thin beams*, J. Acoust. Soc. Am. **114**, 1785 (2003).

[16] B.-G. Loh, S. Hyun, P.I. Ro, and C. Kleinstreuer, *Acoustic streaming induced by ultrasonic flexural vibrations and associated enhancement of convective heat transfer*, J. Acoust. Soc. Am. **111**, 875 (2002).

[17] G. G. Stokes, *On the theory of oscillatory waves*, Camb. Phil. Soc. Trans. **8**, 441 (1847).

[18] M. F. Hamilton, Y. A. Ilinskii, and E. A. Zabolotskaya, *Acoustic streaming generated by standing waves in two-dimensional channels of arbitrary width*, J. Acoust. Soc. Am. **113**, 153(2003).

[19] S. Boluriaan and P.J. Morris, *Acoustic streaming: from Rayleigh to today*, Int. J. Aeroacoust. **2**, 255 (2003).

[20] S.B. Pope, *Turbulent Flows* (Cambridge Univ. Press, Cambridge, 2000).

# 6

# Gravity-induced inverse Chladni patterns[§]

*Inverse Chladni patterns, i.e., grains collecting at the anti-nodes of a resonating plate, are traditionally believed to occur only when the particles are small enough to be carried along by the ambient air. We now show - theoretically and numerically - that air currents are* not *the only mechanism leading to inverse patterns: When the acceleration of the resonating plate is below $g$, particles will always move to the anti-nodes, irrespective of their size. We also explain why this effect has hitherto escaped detection in standard Chladni experiments.*

## 6.1 Introduction

In the previous chapter, we have shown that very fine particles form inverse Chladni patterns on a resonating plate because the particles are dragged by the air to the anti-nodes.

In this chapter we give a proof-of-principle that *all* particles - also coarse ones for which the effect of air can be ignored - are able to form inverse Chladni patterns, by a completely different mechanism. If the vibrational acceleration of the plate is below $g$, it can be shown analytically that the net movement (over one vibration cycle) of the particles due to gravity will be in the direction of the anti-nodes, and this is confirmed by numerical simulation. It would be extremely interesting to observe this effect also experimentally. However, we will show that under standard experimental conditions the subtle mechanism responsible for the pattern formation is overwhelmed by other effects, especially the

[§]Based on: H.J. van Gerner, M.A. van der Hoef, D. van der Meer, and K. van der Weele, *Gravity-induced inverse Chladni patterns*, submitted to Phys. Rev. E.

bending of the plate under its own weight.

## 6.2 Numerical simulations

The simulated system consists of a flexible rectangular plate ($62 \times 62\ \mathrm{cm}^2$) on which $80,000$ glass beads ($\rho = 2.50\ \mathrm{g/cm}^3$, diameter $1.0$ mm) are uniformly distributed. The plate is flexible and pinned along its outer rim. We excite a standing wave pattern in it by applying one of its natural frequencies $\omega_{kl}$, corresponding to $k$ sinusoidal half-wavelengths in the $x$-direction and $l$ in the $y$-direction. Ignoring the additional bending of the plate due to gravity, the vertical deflection at any point $(x,y)$ is then given by:

$$z(x,y,t) = a\sin(\omega_{kl}t)\ \sin\frac{k\pi x}{L_x}\ \sin\frac{l\pi y}{L_y} \tag{6.1}$$

(with $k,l = 1,2,3,...$), where $a$ is the amplitude of the vibration, and $L_x = L_y = 62\ \mathrm{cm}$ the size of the plate. As an example, in Fig. 6.2 we have excited the $2 \times 2$ mode, which for a typical stainless steel plate of 1 mm thickness has a natural frequency of $f_{22}$ $(= \omega_{22}/2\pi) = 50$ Hz (see appendix A, other modes can be seen in Fig. 6.1).

The trajectories of the particles are calculated via the Granular Dynamics code discussed in chapter 2, in which the collisions (with the plate, and between the particles themselves) are taken care of by a 3D soft sphere model including tangential friction. The results do not depend very sensitively on the precise values of the friction and restitution coefficients. In the simulations presented here the friction coefficient is set to $0.2$, and the normal and tangential coefficients of restitution are $0.90$ and $0.33$, respectively. These values are used both for the particle-plate and the particle-particle interaction. A key parameter in vibration is the dimensionless acceleration $\Gamma = a(2\pi f)^2/g$, i.e., the ratio of the vibrational and the gravitational acceleration. For a given mode (with a prescribed frequency $f = f_{kl}$) the value of $\Gamma$ is varied via the amplitude $a$.

In Fig. 6.2(a) we show the final pattern if we give the plate an amplitude of $0.40$ mm ($\Gamma = 4.0$, Fig. 6.2(a)), the dimensionless acceleration is larger than unity over a sizeable region around the anti-nodes, with a maximum of $4.0$ at the anti-nodes themselves. The particles in these regions start to bounce, and (since in most cases a bouncing particle impacts on a section of the plate while it is moving upward) the successive bounces tend to increase their kinetic energy. On the other hand, at the nodal lines the dimensionless acceleration is zero and the collisions with the plate

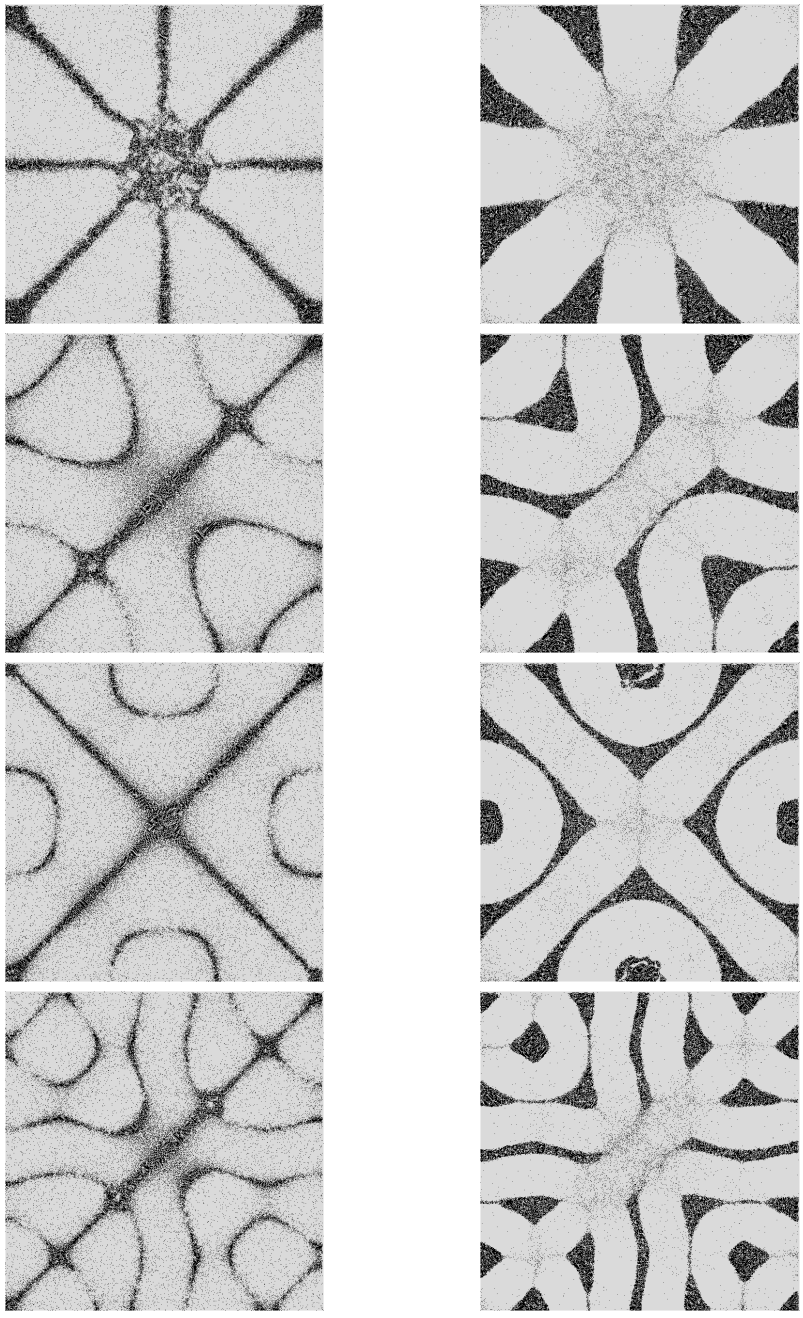

*Figure 6.1: Standard (on the left) and inverse (on the right) Chladni patterns formed on a flexible plate that is pinned in the middle and vibrating at 90, 180, 210, and 390 Hz, respectively. A movie of the formation process can be found on the enclosed CD-ROM.*

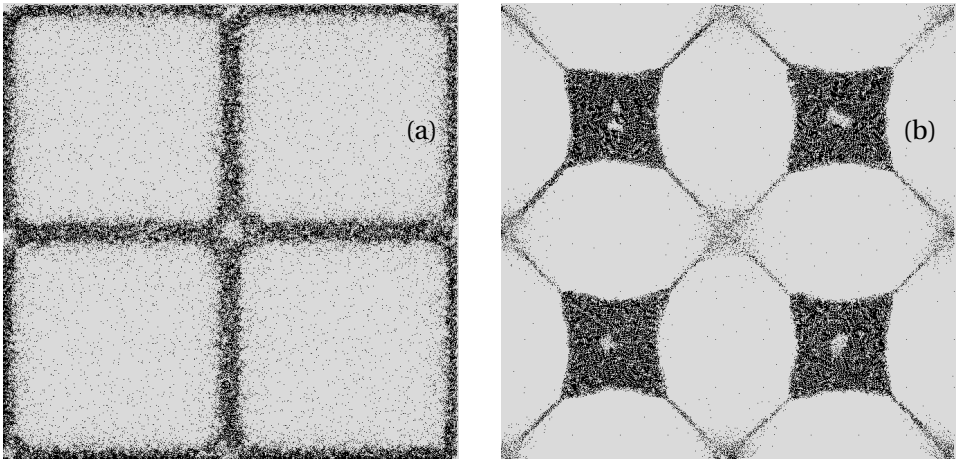


*Figure 6.2: (a) Top view of a flexible plate resonating in its 2 × 2 mode, at* 50 *Hz, with an amplitude of* 0.40 *mm (dimensionless acceleration* $\Gamma = 4.0$*). After 4 seconds most particles have collected at the nodal lines, forming a classic Chladni pattern. (b) The same plate at a smaller amplitude of* 0.09 *mm* ($\Gamma = 0.91$*). The particles now migrate from the nodal lines to the anti-nodes and after 1 minute an inverse Chladni pattern has formed. A movie of the formation process can be found on the enclosed CD-ROM.*

*reduce* the kinetic energy of the particles; this effect is further enhanced by the mutual particle-particle collisions. As a result, starting with all 80,000 particles uniformly distributed over the plate, within a few seconds most of them have accumulated at the nodal lines, forming a standard Chladni pattern.

If we reduce the amplitude to $a = 0.09$ mm ($\Gamma = 0.91$, Fig. 6.2(b)), the particles stop bouncing and start to migrate towards the anti-nodes. After a while, the motion speeds up and after about one minute most of the particles have accumulated at the anti-nodes, thus forming an inverse Chladni pattern.

The general outcome of our simulations is that one can create either a normal or an inverse Chladni pattern, just by varying the value of $\Gamma$: If $\Gamma > 1$ one obtains a normal Chladni pattern, and if $\Gamma < 1$ an inverse one.

## 6.3 Theory

So why do the particles move to the anti-nodes for accelerations below 1 $g$? The explanation - as we will show - lies in the fact that the horizontal

force on the particles, averaged over a complete vibration cycle, points in the direction of the anti-nodes if $\Gamma < 1$. In our analysis we ignore the influence of the ambient air, which is a good approximation for glass spheres of 1 mm diameter. We also ignore the bending of the plate under its own weight and that of the particles; this is a more restrictive assumption, and we will come back to it later.

For $\Gamma < 1$ the particles will not detach from the plate and the vertical position of the particles is given by the same Eq. (6.1) as for the plate, except that $x$ and $y$ are now functions of time. For simplicity, we only consider the $x$-direction, so the vertical position of a particle is:

$$z(x,t) = a\sin(\omega t)\sin\frac{k\pi x(t)}{L_x},\ \ k = 1,2,3,..., \tag{6.2}$$

where we have dropped the subscripts in $\omega_{kl}$ for notational convenience. The up-and-down motion of the plate affects the particle's effective weight $W^*$:

$$\begin{aligned} W(x,t) &= -m\left(g + \ddot{z}(x,t)\right) \\ &\approx -m\left(g - \omega^2\sin(\omega t)\sin\frac{k\pi x(t)}{L_x}\right), \end{aligned} \tag{6.3}$$

with $m$ the mass of the particle, and the minus sign indicates that $W$ is a force pointing in the negative $z$-direction. For $\Gamma < 1$, its magnitude $|W|$ is always between 0 and $2mg$. It can be split in a component perpendicular to the plate $W_\perp$, which is counteracted by the normal force $F_n$ on the particle, and a parallel component $W_\parallel$ which gives the particle an acceleration along the plate's surface.

The forces $W_\perp$, $F_n$, and $W_\parallel$ are shown in Fig. 6.3 at two different instances. In Fig. 6.3(a), the plate is accelerating upwards at the location of the particle, so $|W|$ exceeds $mg$. In Fig. 6.3(b), it is accelerating downward, so now $|W|$ is less than $mg$. As a result, the component parallel to the plate ($W_\parallel$) is larger in Fig. 6.3(a) than in Fig. 6.3(b), and hence the net acceleration over one complete cycle is directed to the anti-nodes. This is the origin of the inverse Chladni patterns.

Let us analyze this mechanism in some more detail. The horizontal component of the force that works on the particle is approximately equal

*We neglect the terms in $\ddot{z}$ with amplitudes $(2ka\pi/L_x)\dot{x}$, $(2ka\pi^2/L_x^2)\dot{x}^2$, and $(k\pi/L_x)\ddot{x}$. For $k = 2$ all these terms are much smaller than $g$.

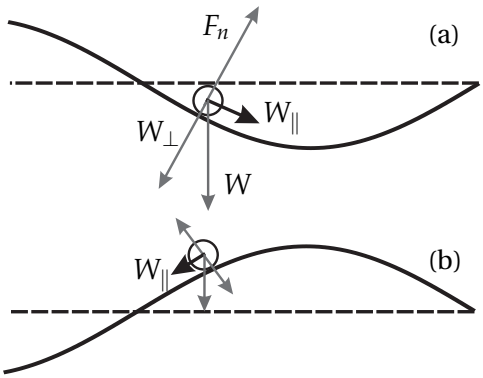


*Figure 6.3: The effective weight $W$ of a particle on the resonating plate and the normal force $F_n$ at two moments during a vibration cycle; the amplitude of the plate has been exaggerated for clarity. The component $W_\perp$ and the normal force $F_n$ balance each other, while the component $W_\parallel$ gives the particle an acceleration along the plate's surface. It is larger in (a) than in (b) and thus the acceleration averaged over a complete vibration cycle is directed towards the anti-nodes.*

to $W$ times the local slope of the plate:

$$\begin{aligned} F_{\mathrm{hor}}(x,t) &\approx W(x,t)\frac{\mathrm{d}z(x,t)}{\mathrm{d}x} \\ &= W(x,t)\frac{k\pi a}{L_x}\sin(\omega t)\cos\frac{k\pi x(t)}{L_x}, \end{aligned} \tag{6.4}$$

and this gives the particle both a translational and rotational acceleration. The translational acceleration is:

$$\ddot{x}(x,t) = \frac{5F_{\mathrm{hor}}(x,t)}{7\,m}, \tag{6.5}$$

where the factor $5/7$ originates from the angular inertia of the particle. To calculate the average horizontal acceleration over a complete cycle, we must integrate Eq. (6.5) from $t = 0$ to $2\pi/\omega$. Since the change in the $x$-position of a particle during one cycle is very small we may treat $x(t)$ as a constant, which gives:

$$\begin{aligned} \langle\ddot{x}\rangle(x,t) &= \frac{\omega}{2\pi}\int_0^{\frac{2\pi}{\omega}} \ddot{x}(x,t)dt \\ &\approx \frac{5k\pi a^2\omega^2}{14L_x}\sin\frac{k\pi x(t)}{L_x}\cos\frac{k\pi x(t)}{L_x} \\ &= \frac{5k\pi a^2\omega^2}{28L_x}\sin\frac{2k\pi x(t)}{L_x}. \end{aligned} \tag{6.6}$$

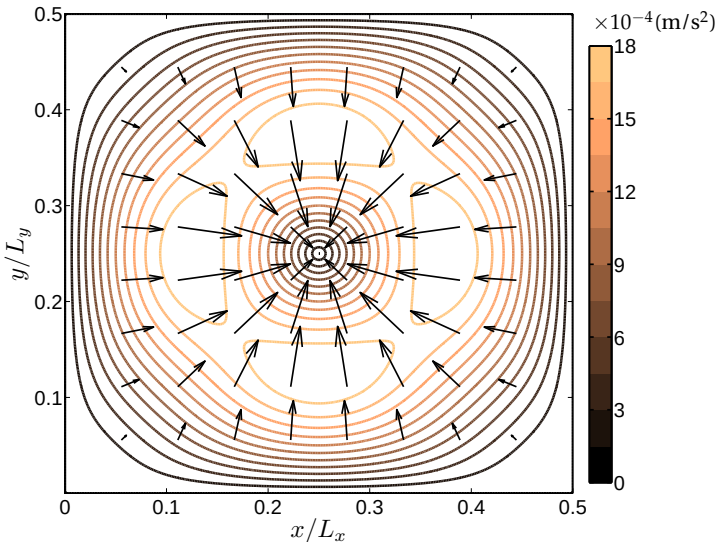


*Figure 6.4: Horizontal acceleration field, averaged over a vibration cycle, experienced by particles on a resonating plate in the* $2 \times 2$ *mode for* $\Gamma = 0.91$*; only one quarter of the plate is shown. The colored contour lines show the magnitude of the acceleration, also indicated by the length of the arrows. The overall acceleration points to the anti-node, explaining the formation of the inverse Chladni pattern in Fig. 6.2(b). Note the striking similarity with the averaged horizontal gas velocities above a resonating plate (see Fig. 5.4(b)), which can lead to air-induced inverse Chladni patterns.*

Note that the term involving $g$ vanishes in the integration, reflecting the fact that the time-averaged contribution of gravity to the horizontal acceleration is zero.

With $\Gamma = a\omega^2/g$, Eq. (6.6) may also be written as

$$\langle \ddot{x} \rangle(x,t) \;=\; \frac{5k\pi g^2\Gamma^2}{28L_x\omega^2}\,\sin\frac{2k\pi x(t)}{L_x}\,, \tag{6.7}$$

where $\Gamma$ is understood to be smaller than 1.

The horizontal acceleration in both the $x$- and $y$-direction can be determined analogously, and Fig. 6.4 shows the average horizontal acceleration as a function of the position $(x,y)$ for one quarter of the vibrating plate in the $2 \times 2$ mode, in top view. The acceleration field is directed to the anti-nodes, and its magnitude (indicated by the length of the arrows, and by the contour lines) is maximal somewhere midway between the nodes and anti-nodes. At the nodes and anti-nodes themselves the

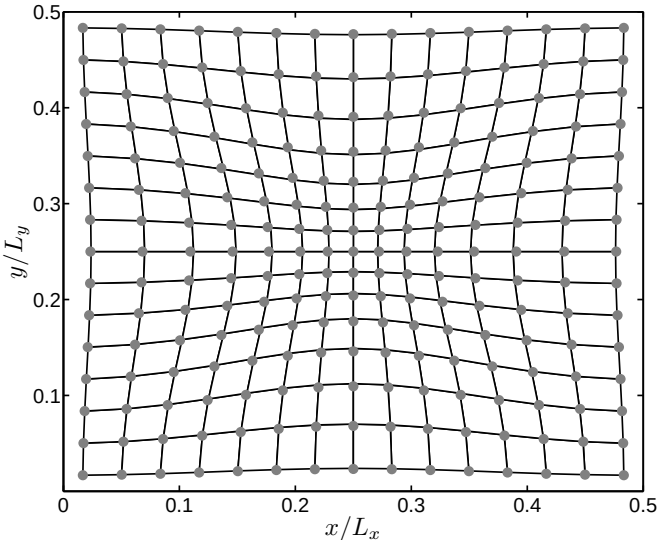


*Figure 6.5: Position of* 225 *particles after* 5 *seconds of vibration (starting out from a uniform distribution) on the upper right quarter of a resonating plate in the* $2 \times 2$ *mode at* $\Gamma = 0.91$. *The grid line crossings represent the predicted positions according to the theoretical expression Eq. (6.6), the dots are the positions obtained by numerical simulation.*

horizontal acceleration is zero. That is why the migration of particles beginning at the nodes (as in Fig. 6.2(b)) starts slowly, then speeds up, and finally comes to rest again at the anti-nodes.

Close inspection of Fig. 6.4 shows that the arrows are not pointing straight towards the anti-node (except on the diagonals): They are curving gently towards the four diagonal lines, bending around the four "islands" of maximal acceleration. This explains the observed diagonal streamlines in Fig. 6.2(b).

In order to quantitatively compare theory and numerical simulation, we carried out a simulation for 900 evenly distributed particles, with initial velocities equal to the local velocity of the plate ($\Gamma = 0.91$, just as in Figs. 6.2b and 6.4). Thanks to the limited number of particles and their uniform initial distribution, they do not collide with each other during the first 7 seconds; this is important for the comparison, since the analysis given above does not take into account any collisions. The solid dots in Fig. 6.5 are the particle positions after 5 seconds of simulation, whereas the line crossings represent the theoretically predicted positions according to Eq. (6.6). The correspondence is seen to be very good.

## 6.4 Experimental considerations

Our simulations and theoretical analysis show that inverse Chladni patterns for coarse particles (not affected by the air currents around the resonating plate) are physically feasible. Nevertheless, they never seem to occur spontaneously, not even on plates that are smooth enough to discard the rolling resistance of the particles. Why is this so?

The problem stems from the fact that the plate must be perfectly horizontal to cope with the tiny amplitudes imposed by the condition $\Gamma < 1$. At the outer rims of the plate this is just a question of accurate alignment, but the horizontality is also affected by the bending of the plate under its own weight and that of the particles. Under normal circumstances, the deflection of the middle of the plate due to its own weight will be considerably larger than the largest admissible vibration amplitude $a$, so the particles will simply roll towards the center, overpowering any tendency to form inverse Chladni patterns.

The deflection for a square plate of dimensions $L \times L$, density $\rho$, and thickness $h$ can be calculated by Navier's method, see appendix A:

$$d_{\mathrm{bend}} \;=\; 0.00406\,\frac{g\rho h L^4}{D}\,, \tag{6.8}$$

where $D = Eh^3/12(1-\nu^2)$ is the stiffness of the plate, with $E$ the elastic modulus and $\nu$ Poisson's ratio. This is to be compared with the largest admissible vibration amplitude $a_{\max} = g/\omega_{kl}^2$ (from the condition $\Gamma < 1$), where the frequency of the $k \times l$ mode is given by $\omega_{kl} = (k^2 + l^2)\pi^2 L^{-2}(D/\rho h)^{1/2}$ (see appendix A), i.e.,

$$a_{\max} \;=\; \frac{1}{(k^2+l^2)^2\pi^4}\,\frac{g\rho h L^4}{D}\,. \tag{6.9}$$

Interestingly, the ratio $R = d_{\mathrm{bend}}/a_{\max} = 0.00406(k^2+l^2)^2\pi^4$ is independent of the material properties or plate dimensions: It only depends on the mode that is excited. For the $2 \times 2$ mode one finds $R = 25.3$, and even for the $1 \times 1$ mode the ratio is still 1.58[†].

Only if the deflection of the plate is artificially suppressed (e.g., by raising the air pressure below the plate by an amount $g\rho h$ N/m$^2$, the

[†]The $1 \times 1$ mode has only one anti-node, at the center of the plate, which is also the lowest point due to the bending of the plate under its own weight. So in this case the inverse-Chladni mechanism and gravity co-operate to direct the particles towards the central position. The dominant contribution comes from gravity.

plate's weight per square meter) may one hope to see inverse Chladni patterning for coarse particles.

And what if we have a resonating membrane (a drumhead) instead of a metal plate? For a membrane in vacuum, Eqs. (6.8)-(6.9) take the form (see appendix A) $d_{\rm bend} = 0.0737\, g\mu h L^2/T$ and $a_{\rm max} = g\mu h L^2/(k^2+l^2)\pi^2 T$, where $\mu$ denotes the mass of the membrane per unit area and $T$ the tensile force per unit length. Therefore, $R = 0.07376(k^2+l^2)\pi^2$ for a membrane in vacuum, giving 5.82 for the $2\times 2$ mode, and 1.45 for the $1\times 1$ mode, which is still too much.

In air, if the membrane is sufficiently thin, the frequency of the natural modes (and hence the ratio $R$) is significantly lowered because the added mass density of the air $\rho_{\rm add}$ is not negligible with respect to the density of the membrane $\mu h$. The added mass density of air can be calculated to be [3]

$$\rho_{\rm add} = \frac{\rho_{\rm air}}{\sqrt{k_{kl}^2 - \omega^2 \rho_{\rm air}/B}}\,, \tag{6.10}$$

with $k_{kl} = 2\pi\sqrt{k^2+l^2}/L$ the wavenumber of the $k\times l$ mode, $B$ the bulk modulus, and $\rho_{\rm air}$ the density of the surrounding air. With Eq. (6.10), the ratio $R$ then takes the form $R = 0.0737(k^2+l^2)\pi^2/(1+m_{\rm air}/\rho)$. This can indeed be smaller than unity for very thin membranes[‡]. However, the deflection of the membrane is not only due to its own weight but also to the weight of the particles: $R$ will increase as soon as we add the particles (unless they are exceptionally light; in that case, however, the effect of the ambient air cannot be neglected). So, also for membranes, inverse Chladni patterning of coarse particles can only be expected to occur if one specifically optimizes the experimental setup.

Finally, one could think that a liquid surface, being perfectly horizontal, might provide the right conditions for inverse Chladni patterning. Indeed, particles on a resonating water surface *do* cluster in Chladni patterns, either normal or inverse ones, but in this case the distinction is due to capillarity effects, not to a variation of $\Gamma$; so the physics of the effect is different. Hydrophilic particles gather at the nodes of the water surface (forming a normal Chladni pattern), whereas hydrophobic particles go to the anti-nodes [4].

[‡]For instance, $R$ will be smaller than 1 for the $2\times 2$ mode if one takes a rectangular mylar membrane with side length $L = 0.62$ m and thickness $h = 10\ \mu$m.

## 6.5 Conclusion

We have shown, by numerical simulations and theory, that particles on a resonating plate can form inverse Chladni patterns if the dimensionless acceleration $\Gamma$ is smaller than 1. On a standard Chladni plate, however, the formation of these patterns is overwhelmed by the bending of the plate under its own weight. Only if this bending is suppressed should one be able to observe inverse Chladni patterning of coarse particles in experiment.

## Appendix A: Natural frequency and deflection of a stressed plate

The partial differential equation for the vertical displacement $w$ of a thin membrane is [1]:

$$T\nabla^2 w + p = \rho h \frac{\partial^2 w}{\partial t^2} \,, \tag{6.11}$$

With $T$ the tensile force per unit length and $p$ the vertical load on the plate. The partial differential equation for the displacement $w$ of a plate is [1]:

$$-D\nabla^4 w + p = \rho h \frac{\partial^2 w}{\partial t^2} \,, \tag{6.12}$$

with

$$D = \frac{Eh^3}{12(1-\nu^2)} \,. \tag{6.13}$$

These equations can be combined into the partial differential equation for the displacement $w$ of a stressed plate:

$$T\nabla^2 w - D\nabla^4 w + p = \rho h \frac{\partial^2 w}{\partial t^2} \,. \tag{6.14}$$

### Deflection due to the weight of the plate

We can approximate the uniform load on the plate $p = \rho g h$ by a summation of sine functions [2]:

$$p(x,y) = \sum_{m=1}^{\infty} \sum_{n=1}^{\infty} a_{mn} \sin(\alpha_m x) \sin(\beta_n y) \,. \tag{6.15}$$

with

$$\alpha_m = \frac{m\pi}{a}\ ,\ \ \beta_n = \frac{n\pi}{b}\ ,\ \text{and}\ a_{mn} = \frac{16\rho g h}{\pi^2 mn},\ . \tag{6.16}$$

if $m$ and $n$ are odd integers and $a_{mn} = 0$ when $m$ and $n$ are even. For the vertical deflection of the plate $w$, we take:

$$w(x,y) = \sum_{m=1}^{\infty}\sum_{n=1}^{\infty} C_{mn}\sin(\alpha_m x)\sin(\beta_n y)\ . \tag{6.17}$$

Substituting Eqs. 6.15 and 6.17 in Eq. 6.14 and setting the time deravitive to zero, we obtain:

$$\sum_{m=1}^{\infty}\sum_{n=1}^{\infty}(-TC_{mn}(\alpha_m^2+\beta_n^2) - DC_{mn}(\alpha_m^2+\beta_n^2)^2 + a_{mn}) = 0\ . \tag{6.18}$$

Solving this equation for $C_{mn}$ gives:

$$C_{mn} = \sum_{m=1}^{\infty}\sum_{n=1}^{\infty}\frac{a_{mn}}{T(\alpha_m^2+\beta_n^2)+D(\alpha_m^2+\beta_n^2)^2}\ . \tag{6.19}$$

For $a = b = L$, and $x = y = L/2$ the equation for de maximum deflection of the plate, $w_{\max} = d_{\text{bend}}$ yields:

$$d_{\text{bend}} = \sum_{m=1}^{\infty}\sum_{n=1}^{\infty}\frac{(-1)^{\frac{m+n}{2}-1}16\rho g h}{\pi^2 mn(T((\frac{m\pi}{L})^2+(\frac{n\pi}{L})^2)+D((\frac{m\pi}{L})^2+(\frac{n\pi}{L})^2)^2)}\ . \tag{6.20}$$

This is a rapidly converging series. If we take $T = 0$, $d_{\text{bend}}$ becomes:

$$d_{\text{bend}} = \alpha\frac{g\rho h L^4}{D}\ , \tag{6.21}$$

with $\alpha$ is 0.00406 (see also [1]). If we take $D = 0$, $d_{\text{bend}}$ becomes:

$$d_{\text{bend}} = \alpha\frac{g\rho h L^2}{T}\ , \tag{6.22}$$

with $\alpha$ is 0.0737.

## Natural frequency of the plate

If we write $w(x,y,t)$ as $AX(x)Y(y)T(t)$ and substitute this in in Eq. 6.14 we obtain:

$$T(Y\frac{\partial^2 X}{\partial x^2}+X\frac{\partial^2 Y}{\partial y^2}) - D(Y\frac{\partial^4 X}{\partial x^4}+\frac{\partial^2 X}{\partial x^2}\frac{\partial^2 Y}{\partial y^2}+X\frac{\partial^4 Y}{\partial y^4})T + p = \rho h XY\frac{\partial^2 T}{\partial t^2}\ . \tag{6.23}$$

Assuming $X = \sin(\alpha x)$, $Y = \sin(\beta y)$ and $T = \sin(\omega t)$, and ignoring $p$, we get:

$$(-T(\alpha^2+\beta^2) - D(\alpha^2+\beta^2)^2 + \omega^2\rho h)\sin(\alpha x)\sin(\beta y)\sin(\omega t) = 0\ . \quad (6.24)$$

With the appropriate boundary conditions for a simply supported plate, the solutions for this equation are (amongst others):

$$\alpha_k = \frac{k\pi}{a}, \beta_l = \frac{l\pi}{b}\ , \quad (6.25)$$

and

$$\omega^2 = \frac{(T(\alpha_k^2+\beta_l^2) + D(\alpha_k^2+\beta_l^2)^2}{\rho h}\ . \quad (6.26)$$

With $a = b = L$, this reduces to:

$$\omega_{kl}^2 = \frac{T(k^2+l^2)\frac{\pi^2}{L^2} + D(k^2+l^2)^2\frac{\pi^4}{L^4}}{\rho h}\ . \quad (6.27)$$

If we take $T = 0$, $\omega$ becomes:

$$\omega_{kl} = (k^2+l^2)\frac{\pi^2}{L^2}\sqrt{\frac{D}{\rho h}}\ , \quad (6.28)$$

If we take $D = 0$, $\omega$ becomes:

$$\omega_{kl} = \sqrt{k^2+l^2}\frac{\pi}{L}\sqrt{\frac{T}{\rho h}}\ , \quad (6.29)$$

### Ratio between bending and vibration amplitude

In this section we will determine the ratio between the deflection due to the own weight of the plate and the deflection due to vibration. First, we take $T = 0$. The maximum deflection of a simply supported square plate due to vibration while $\Gamma < 1$ is:

$$a_{\max} = g/\omega_{kl}^2 = \frac{gL^4\rho h}{(k^2+l^2)^2\pi^4 D}\ , \quad (6.30)$$

so the ratio in the $2\times 2$ vibration mode ($k = l = 2$) is:

$$R = \frac{d_{\text{bend}}}{a_{\max}} = \frac{\alpha\frac{g\rho hL^4}{D}}{\frac{gL^4\rho h}{64\pi^4 D}} = 64\alpha\pi^4 \approx 25.3\ , \quad (6.31)$$

i.e., the deflection due to the mass of the plate is 25.3 times larger than the deflection due to vibrations.

We now take $D = 0$ i.e., the plate can be considered as a membrane. The maximum deflection of a membrane due to vibration while $\Gamma < 1$ is:

$$a_{\max} = g/\omega_{kl}^2 = \frac{gL^2\rho h}{(k^2+l^2)\pi^2 T}\,, \tag{6.32}$$

so the ratio in the $2 \times 2$ vibration mode ($k = l = 2$) is:

$$R = \frac{d_{\text{bend}}}{a_{\max}} = \frac{\alpha\frac{g\rho h L^2}{T}}{\frac{gL^2\rho h}{8\pi^2 T}} = 8\alpha\pi^2 \approx 5.82\,, \tag{6.33}$$

i.e., the deflection due to the mass of the membrane is 6 times larger than the deflection due to vibrations.

We can conclude that the deflection of the plate due to its own weight will always be 6 to 25 times larger than the deflection due to vibrations, even when a tensile stress is applied on the plate.

## References

[1] L. Meirovitch, *Analytical methods in vibrations* (Macmillan, New York, 1967).

[2] S.T. Timoshenko and S. Woinowsky-Krieger, *Theory of plates and shells* (McGraw-Hill, New York, 1959).

[3] S. Kukathasan and S. Pellegrino, *Vibration of Prestressed Membrane Structures in Air*, Proc. 43rd AIAA/ASME/ASCE/AHS/ASC Structures, Dynamics, and Materials Conference, Denver, AIAA **2002**, 1368 (2002).

[4] G. Falkovich, A. Weinberg, P. Denissenko, and S. Lukaschuk, *Surface tension: floater clustering in a standing wave*, Nature **435**, 1045 (June 2005).

# 7

# Storage and discharge of a granular fluid[§]

*Experiments and computational simulations are carried out to study the behavior of a granular column in a silo whose walls are able to vibrate horizontally. The column is brought to a steady-fluidized-state and it behaves similar to a hydrostatic system. We study the dynamics of the granular discharge through an opening at the bottom of the silo in order to search for a Torricelli-like behavior. We show that the flow rate scales with the wall induced shear rate, and at high rates, the granular bed indeed discharges similar to a viscous fluid.*

## 7.1 Introduction

One of the most conspicuous laboratories in granular physics is a silo full of grains. If the column inside the silo is in repose, it behaves as a strange solid: the grain-grain interactions break up the symmetry imposed by gravity and a screening effect appears, redirecting most of the weight of the column onto the side walls of the silo (Janssen effect [2]). This, of course, is an annoying phenomenon for a farmer; not only due to the impossibility of knowing the real mass the silo holds, but because the walls might not sustain the normal forces applied by the grains. If we now discharge the silo through a hole made at its bottom, the material flows, but it behaves as a strange fluid. Even if the diameter of the aperture is larger than the size of the grains, clogging structures appear interrupting the discharge (jamming effect [3, 4]). Due to the confluence of these

[§]Published as: Hector Pacheco-Martinez, Henk Jan van Gerner, and J. C. Ruiz-Suárez, *Storage and discharge of a granular fluid*, Phys. Rev. E **77**, 021303 (2008). The numerical work described in this chapter is to be considered part of this thesis. The experiments are work of Hector Pacheco-Martinez *et al.* and are only included for clarity reasons.

two phenomena, and the importance they have in industrial silos and hoppers, granular storage and discharge have been studied profusely over the decades.

The Janssen effect states that the mass measured at the bottom of the silo is not the real mass $M$ one pours into it, but an apparent one that follows the relation $M_{\rm app} = M_{\rm s}(1 - e^{-M/M_{\rm s}})$; where $M_{\rm s}$ is the mass measured at the bottom of the silo when saturation is reached. This effect was observed by Janssen at the end of the 19th century, but it is still a matter of study nowadays. Indeed, well controlled experiments have been carried out recently in laboratory silos [3–5]. Also, it has been demonstrated that the Janssen law is valid even if the side walls move vertically [6].

Grain discharge from a silo was first studied by engineers (see the review of Nedderman *et al.* [7]). Within that community, in 1960 Beverloo and coworkers proposed, after some systematic experiments changing several variables, the formula used today to correlate the outflow rate $W$ with the diameter $D$ of the aperture [8]: $W = \zeta \rho_B g^{1/2}(D - kd)^{5/2}$, where $\zeta$ and $k$ are constants, $g$ is the acceleration of gravity, and $\rho_B$ the effective density of the granulate. While this expression is empirical, it can be also deduced from basic dimensional considerations [7].

Two important behaviors are observed during the discharge. Firstly, in order to obtain a continuous flow, the diameter of the outlet has to be greater than a critical diameter $D_c$ (if the grains are spherical, the value of $D_c$ lies between 4 and 5 times the diameter of a single grain $d$). Secondly, the discharge rate is constant and independent of the column height $H$ (usually called the head). This second phenomenon is puzzling, because it contrasts with the case of a normal liquid flowing out from a container, where the flux $W$ decreases as $H$ decreases (if the liquid has very low viscosity, $W$ varies according to Torricelli's law: $W$ is proportional to $H^{1/2}$).

Despite some unsolved concerns in the behavior of dense granular flows, the extended belief in the literature is that such flows are governed by the rapid formation of stress-bearing structures due to inter-particle interactions. Furthermore, since grains are inelastic, the rather fast collapse into such structures imposes a time scale. When this scale is shorter than the scale of the time imposed by the strain rate in the system (normally the case in gravity-driven flows), the grains move coherently [9].

Is the formation of such structures near the hole of a silo, and the velocity correlation of the grains, beneath the constant discharge rate in a silo? A plausible strategy to advance the understanding of this problem is to inject energy in the system. In fact, by shearing the column and fluidize

it, we could overcome the formation of arches and learn about the effect they have in the discharge dynamics. However, we have to inject energy to the core of the column on a time scale shorter than the one imposed by grain inelasticity. To our knowledge, only few works have studied the discharge rates in vibrating hoppers, silos, or hourglasses [10–13]. However, in all these cases, the containers were shaken either vertically or horizontally as whole units.

Our experimental setup is different. We constructed a novel silo able to fluidize the entire column in steady-state conditions with no convection. The aim of the present work is to study the discharge of such steady-state vibro-fluidized granular column. We complement our experimental study with 3D computer simulations.

## 7.2 Setup

The silo is a segmented container composed of eight independent acrylic panels, see Fig. 7.1. The panels, with dimensions $1 \times 20 \times 50$ cm, have at their corners 1 cm diameter steel bearings. These bearings have the function of supporting the weight of the panels, allowing as well the possibility of back-and-forth small movements. Each one of the bearings rest on metal pieces soldered onto a heavy metal structure. The panels are firmly attached to power speakers, these are also fixed to the structure and are connected in parallel, feed by a high-power amplifier (EG-4000) connected to a function generator (HP-33120A). Two panels, one on top of the other, form a wall. Therefore, the silo has 1 m of height and 400 $\mathrm{cm}^2$ of cross section. Neighboring walls move out of phase (while two opposite walls move in, the others move out). In doing this, we maintain the total volume of the granular column constant. The panels do not touch each other (the space left between them and the vertical beams of the structure is 1 mm). A similar wall-moving container has been used by us elsewhere to fluidize a granular bed and prove Archimedean buoyancy [14]. We use very light particles (polystyrene spheres of density 16 kg/$\mathrm{m}^3$) to fill the silo. The mean diameter of the spheres is 4.65 mm with a friction coefficient of $0.4 \pm 0.1$. The maximum peak-to-peak vibration amplitude of the walls is 3 mm. In order to avoid static charges, the spheres were treated with an antistatic spray, although some times few of them were attracted to the walls.

*Figure 7.1: Photograph of the real silo.*

## 7.3 Experiments

In our first experiment, particles were slowly poured into the silo. The bottom of it, an acrylic panel also separated from the lateral walls and the structure, was fixed to a balance. During the filling process, the function generator is turned off. In order to keep the walls firmly fixed, the 32 roll-bearings were glued onto the small bases they roll. In Fig. 7.2 we plot the mass $M_{\rm app}$ (measured with the balance) versus the real mass $M$ poured into the silo. We obtained the expected Janssen's effect. Next, we empty the silo and repeat the pouring process. This time, however, the walls are put to vibrate at a frequency of 20 Hz and amplitude of 1.5 mm (previously, the glue on the bearings was removed). The data are also plotted in Fig. 7.2. Instead of an exponential curve, a straight line $M_{\rm app} = M$ is obtained. This result indicates that Janssen's effect vanishes and the entire mass of the column is received by the bottom. Since this is

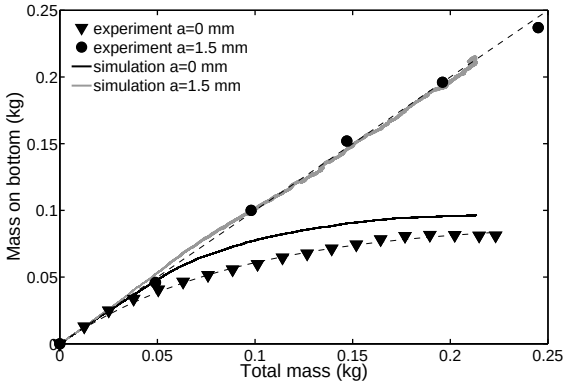


*Figure 7.2: Plot of the mass measured at the bottom of the silo as a function of the mass poured into it. The triangular points were taken using static walls. The circular points were obtained experimentally with vibrating walls. With static walls, the measured mass follows Janssen's law, which is indicated by the dashed curved black line. With vibrating walls, a hydrostatic behavior is obtained, which is indicated by the dashed straight black line. The dark gray line is obtained in a simulation with vibrating walls. The light gray line is obtained using static walls. Both the total mass and the mass on the bottom obtained in the simulation are multiplied by five for comparison with the experimental results.*

what occurs in standard liquids, the granular fluidized column behaves, apparently, similar to a hydrostatic system.

It is well known that Janssen's effect vanishes in silos with frictionless walls. Indeed, in such ideal conditions stress paths do not “anchor" at the walls and the bottom of the silo receives the entire weight of the column. But the system is statically inert in that case, not hydrostatic. In our vibrating silo the weight of the column is not only borne entirely by the bottom, but, in addition, the particles jiggle around their equilibrium positions. We carried out a simple experiment to grasp the nature of this steady dynamics. We introduced into the bed a hollow spherical intruder made of polystyrene (effective density of 6 kg/m3 and diameter 12 cm). We observe that the intruder rises to the surface. Since there is no convection [15], air drag [16], or inertia [17] (essentially because there is no vertical vibration applied to the silo), the only mechanism to segregate the intruder to the top is Archimedean buoyancy. Buoyancy is a physical effect due to the hydrostatic pressure acting on an intruder inside a fluid (there is more pressure on the lower side of the intruder than above it) and this is precisely the physical meaning of the straight line plotted in

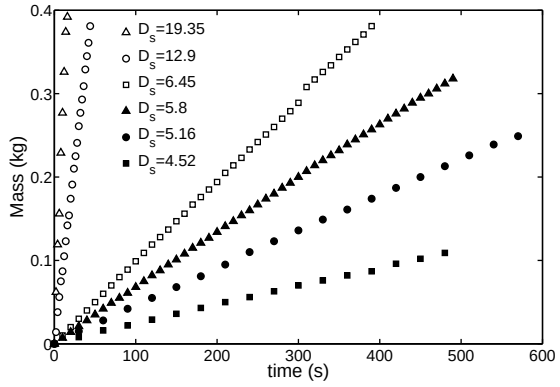


*Figure 7.3: A silo discharge experiment. The mass leaving the silo is plotted as a function of time, for different scaled outlet diameters ($f = 20$ Hz, $a = 1.5$ mm). The linear behavior means that the flow rate is constant.*

Fig. 7.2. The reader can find a thorough discussion on this subject in our previous work [14].

We now discharge the silo through a hole made at its bottom and measured the out flowing mass as a function of time. We do this for several holes, always with diameters larger than $D_c$ to avoid jamming. First, we discharge the silo with still walls. The obtained straight lines (see Fig. 7.3) confirm that the outflow is constant in time. Moreover, the slopes of these lines, as a function of $D$, conform to the power law found by Beverloo (see Fig. 7.4).

Finally, we discharge the silo while the walls vibrate. We have shown that this special shearing is able to continuously break the arches at the walls, producing hydrostatic-like conditions (at least from the point of view of Buoyancy). However, will it modify the way the silo discharges? Under the above shearing conditions (20 Hz and amplitude of 1.5 mm) the answer is that it does not. The results are identical to the ones plotted in Fig. 7.3.

An important difference is, nevertheless, observed: when the walls are still, a funnel on the free surface of the head is formed, more profound at the end of the discharge, indicating that the particles in the core of the column descend faster than particles near the walls. However, when the walls vibrate, the funnel on the surface does not form and we observe instead a descending flat head. This, of course, can be easily explained: due to the vibration, the friction near to the walls decreases, the particles descend faster and, therefore, the head remains flat.

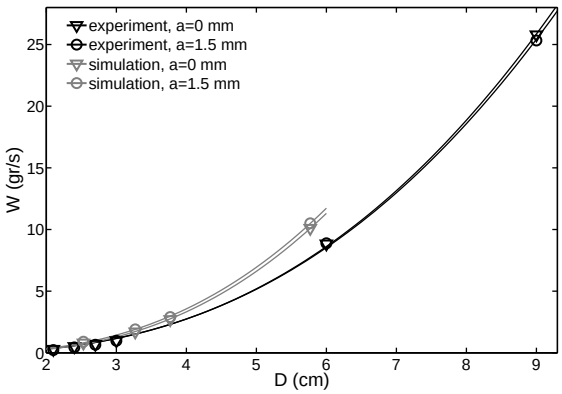


*Figure 7.4: Flow rates plotted as a function of the outlet diameter. The black markers indicate the results obtained from the experiments and the gray markers indicate the results obtained from the simulation, both for static and vibrating walls ($f = 20$ Hz, $a = 1.5$ mm). The solid lines are curves fitted with Beverloo's model. The parameters used are shown in the body of the figure, where $C = \zeta \rho_B g^{1/2}$.*

Summarizing, the Janssen's effect disappears when the walls vibrate, however, despite the column is fully fluidized, the discharge dynamics still satisfies Beverloo's scaling (although the free surface morphology of the head changes). Air drag, during a silo discharge, is an important issue. It has been shown that an adverse pressure gradient builds up at the bottom of the silo and acts on the particles close to the outlet [18]. However, since the silo is sectioned, there is no pressure gradient built along the column. Thus, air drag can not explain our findings. In order to explain the above experimental results, we explore the dynamics of the silo discharge with 3D computer simulations.

## 7.4 Numerical simulations

Some computational works have been carried out in the past to study the discharge of silos in two and three dimensions [19, 20]. Vibrating hoppers have been also investigated [11]. However, we perform simulations in 3D silos with the extra ingredient of having horizontally moving walls. For this, we use the Granular Dynamics code described in chapter 2. The particles interact with each other via a soft-sphere model which includes tangential friction. Due to the fact particles in the column are in contact

to each other all the time, friction is important to be considered. The system that we studied in the simulations contained 50000 particles with a density of 16 kg/$\mathrm{m}^3$ and an averaged diameter of 4.65 mm. A Gaussian size distribution with a standard deviation of 0.465 mm was applied to avoid excessive ordering of the particles in the silo. The dimensions of the silo were $0.1 \times 0.1 \times 0.5$ m ($W \times D \times H$).

First, the coefficient of restitution was set to the value of 0.9 for the normal direction and 0.33 for the tangential direction. The friction coefficient was set to 0.3. For the particle-wall interaction, the same collision parameters were used. The virtual silo was filled and we plotted the mass transferred to the bottom versus the mass poured inside (light gray line in Fig. 7.2). Both the mass on the bottom and total mass were multiplied by five. Although the light gray line has been scaled in order to compare with the real data, it is obvious that it corresponds to the Janssen's exponential curve. Such result is an indication that the computational code gives the expected arch-shielding behavior found in silos. Thereafter, we filled the silo while the walls were vibrating. As in the real experiment, the result is a straight line (dark gray line in Fig. 7.2), indicating that hydrostatic like conditions are obtained.

Next, we perform simulations to analyze the dynamics of the granular flow through openings made in the bottom of the silo for still walls and walls vibrating with a frequency of 20 Hz and amplitude of 1.5 mm. The results confirm our experimental observations: with or without moving walls, the discharge rates are constant and conform to Beverloo's law when plotted as a function of $D$, see Fig. 7.4.

In order to understand why the discharge rates are constants despite the column fluidization, we pay attention to the stress distribution during the discharge process. In Fig. 7.5(a) we plot the mass carried by the bottom and by the walls before and after the orifice is opened ($t = 15$ s). Before the discharge (orifice closed), the mass is borne entirely by the bottom, confirming once more the hydrostatic conditions. However, as soon as the hole is opened, the hydrostatic condition is lost and the walls receive part of the weight, reestablishing the Janssen's effect. This may explain why the rates of discharge are constant despite the hydrostatic regime of the column.

We can go beyond our experimental capabilities and investigate computationally what happens if larger shear rates are used. In Fig. 7.5(b) we show the results at a higher vibration strength (frequency 50 Hz and amplitude 3 mm). Here, the silo discharges differently: the walls never recover weight and the discharge is not constant, following a Torricelli-

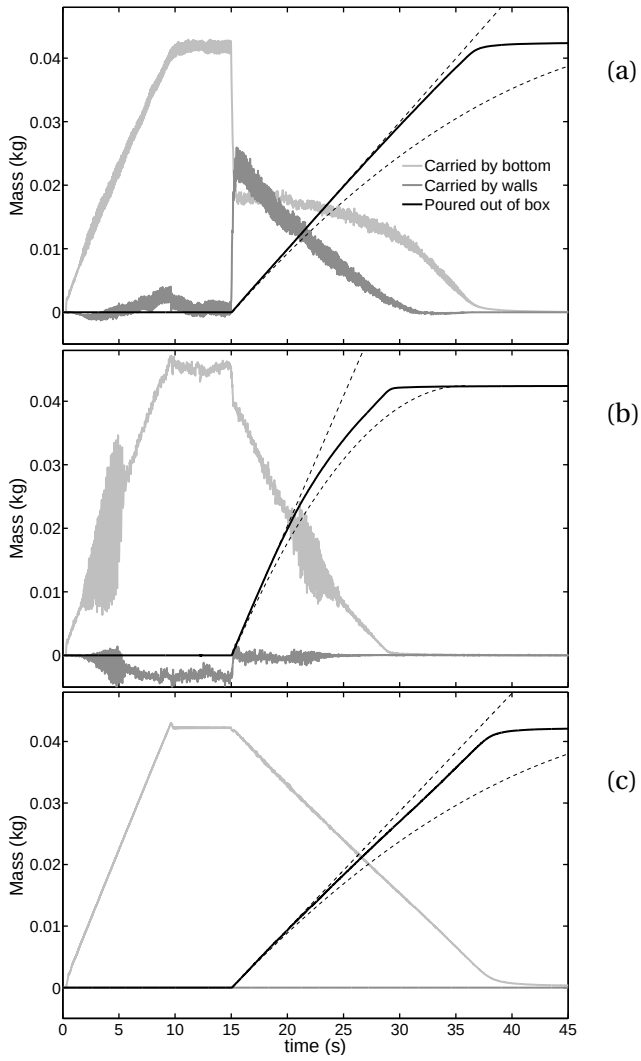


*Figure 7.5: (a) Mass carried by the bottom (light gray line) and walls (dark gray line) during the discharge. The mass leaving the silo is indicated with black lines. The dashed lines resembles Beverloo's and Torricelli's discharge. The walls are vibrating with a frequency of 20 Hz and an amplitude of 1.5 mm. (b) Discharge at a higher shaking strength (frequency 50 Hz, amplitude 3 mm). The discharge follows a Torricelli like behavior. (c) Discharge with no vibration and frictionless walls. The discharge deviates only slightly from a straight line.*

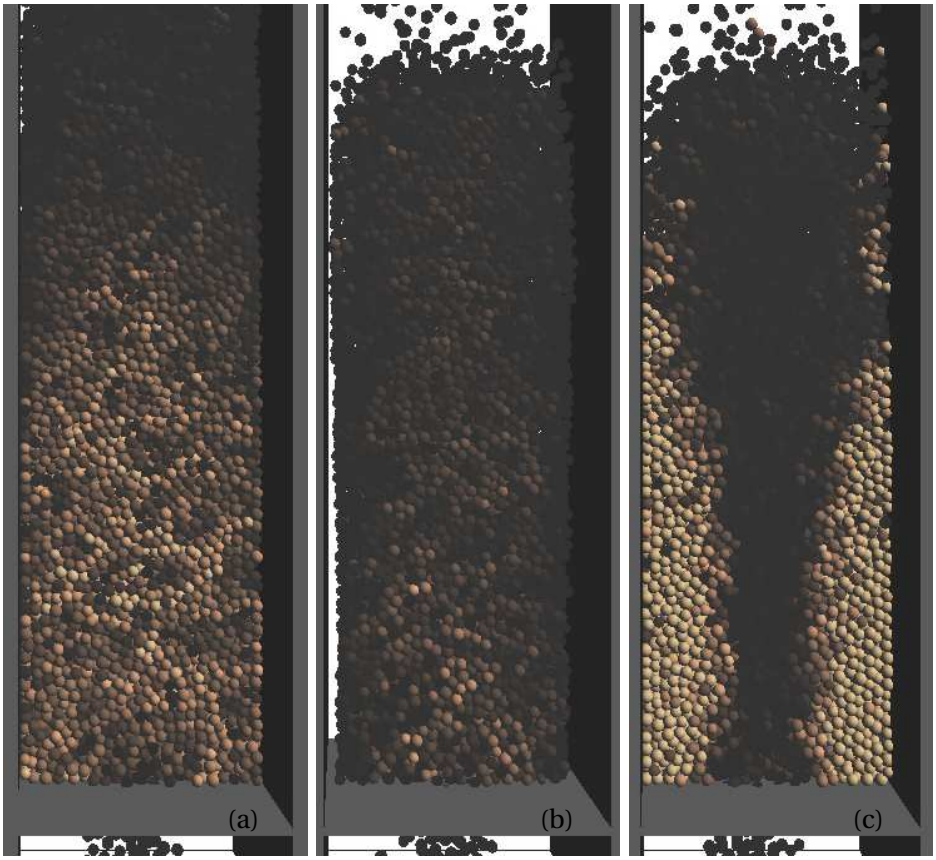


*Figure 7.6: (a) Cross section of the granular column with walls vibrating at a frequency of 20 Hz and amplitude of 3 mm. A light color indicates a high particle force whereas a dark color indicates a low force. Force chains can be identified. (b) and (c) Cross section of the granular column with walls vibrating at a frequency of 50 Hz and amplitude of 3 mm at two instances during a vibration cycle. In (b), the column is detached from the wall. The closure of the gap causes a shockwave through the column, as can be seen in (c). However, this shockwave does not influence the outflow rate since this rate scales with the shear rate. A movie of these simulations can be seen in [22].*

like behavior (see how the plot of the mass poured out of the silo bends). It could be argued that the complete absence of wall friction (due to vibration) is responsible for this behavior. However, in Fig. 7.5(c) we show simulations for a still silo with frictionless walls and clearly observe that the discharge deviates only slightly from a straight line. Fig. 7.6(a) shows a cross section of the granular column with walls vibrating at a frequency of

20 Hz and amplitude of 3 mm. The color in the beads indicates the force chains distribution. Although a rigorous analysis of force chains is beyond this study, it is illustrative to show how these chains form each vibration cycle. Figures 7.6(b) and (c) show cross sections of the granular column with walls vibrating at a frequency of 50 Hz and amplitude of 3 mm at two instants during a vibration cycle. In (b), the column is detached from the wall. This is caused by the large acceleration of the walls; when two walls move inward, the granular mass can either move outward or upward. When the pressure needed to accelerate the particles outwards is larger than the pressure of to the particles above, the particles can not follow the walls anymore but will move upward instead, and the column detaches from the wall. This is also the reason why with vibrating walls, a bulge is formed on the free surface of the granular mass. The closure of the gap causes a shockwave through the column, as can be seen in (c). However, this shockwave does not influence the outflow rate. A movie of these simulations can be seen here [22].

As the walls of the silo move in and out, the granular column is sheared with a shear rate approximately four times the velocity of the wall divided by the width of the silo. At a frequency of 20 Hz and amplitude of 1.5 mm, this wall induced shear rate is around 8 $\mathrm{s}^{-1}$. However, there is also a gravity induced shear rate due to the discharge of the particles. This gravity induced shear rate is approximately the outflow velocity divided by the radius of the aperture, around 30 $\mathrm{s}^{-1}$, i.e. higher than the wall induced shear rate. At a frequency of 50 Hz and amplitude 3 mm, however, the wall induced shear rate increases to 38 $\mathrm{s}^{-1}$. Is this shear rate increase what causes the Torricelli like behavior observed in Fig. 7.5(b)? Fig. 7.7(a) shows the averaged (over 15 cycles) flow rates as a function of the pressure on the bottom of the silo for different cases. We also carried out one simulation in a box with dimensions of $0.15 \times 0.15 \times 0.75$ m ($W \times D \times H$) (i.e., 1.5 times larger than the box used in the former simulation) and 2.25 times as many particles at a frequency of 50 Hz and an amplitude of 2 mm. The flow rate in this box is lower than the flow rate in the smaller box vibrating with the same frequency and amplitude. We observe that the only two sets of data showing Torricelli like behavior are the ones obtained at 50 Hz with amplitudes 2 and 3 mm. This is more evident after rescaling the outflow rate (by subtracting the constant outflow velocity with static walls and dividing by the walls induced shear rate, see Fig. 7.7(b)). Although the transition between low and high shear regimes is gradual, the change on the silo discharge produced by a high shear is very clear.

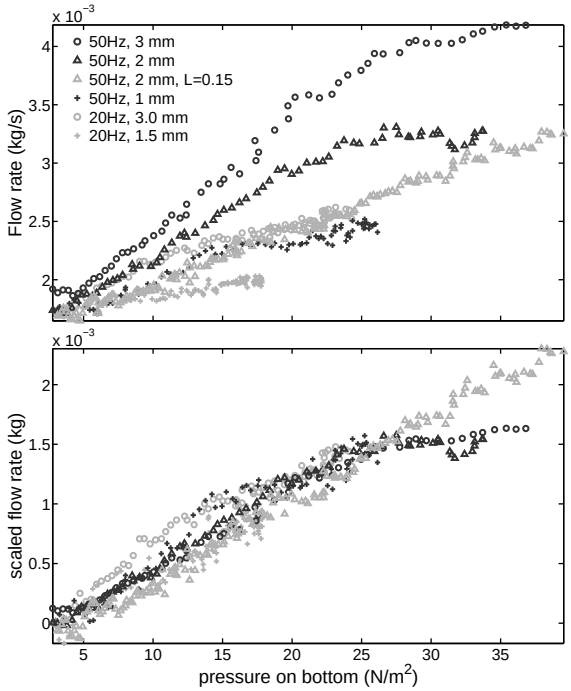


*Figure 7.7: (a) Flow rates plotted as a function of the pressure on the bottom. All the results are obtained in simulations using a box with a depth and width of 0.1 m, except the dark gray triangles, for which a box with a depth and width of 0.15 m was used. Note that, with the same vibration parameters, the flow rate in the large box is lower than the flow rate in the standard box. The restitution and friction coefficients are 0.9 and 0.3, respectively. (b) Scaled flow rates plotted as a function of the pressure on the bottom. The flow rates from (a) are scaled by subtracting the constant flow rate with static walls divided by the walls induced shear rate. The data collapses reasonably well for low and high shear rates, indicating that the flow rate scales with the wall induced shear rate.*

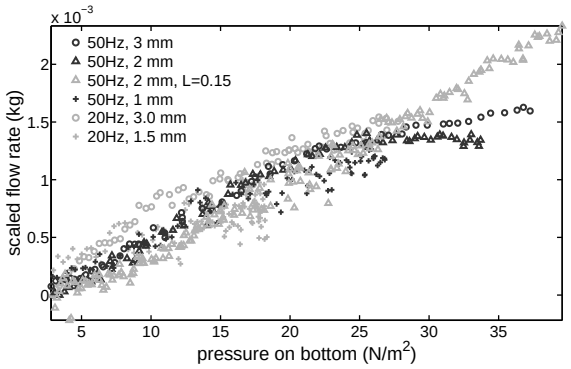


*Figure 7.8: Scaled flow rates plotted as a function of the pressure on the bottom. The restitution and friction coefficients are, respectively, 0.7 and 0.3.*

Finally, we investigate the effect produced on the discharges when both the restitution and friction coefficients are changed. Values as low as 0.70 for the first one, and as high as 0.50 for the second, were used. The discharge rates (averaged over 15 cycles) do not change much and keep scaling reasonably well (Figs. 7.8 and 7.9). The tangential restitution coefficient has also been changed, but no significant sensitivity has been found with this parameter.

## 7.5 Conclusion

We have carried out experimental and computational work to study the discharge of a fluidized granular column in a silo with moving walls. We have shown that, at intermediate shear rates, the column attains complete fluidization: the Janssen's screening effect disappears, the pressure becomes linear, and a clear buoyancy effect on light intruders is observed. However, despite the fluidized condition of the column, upon discharge, the screening is recovered (the hydrostatic like condition is lost) and the discharge rate of the silo is constant. Higher shear rates are necessary to fully suppress screening and observe Torricelli-like discharge rates.

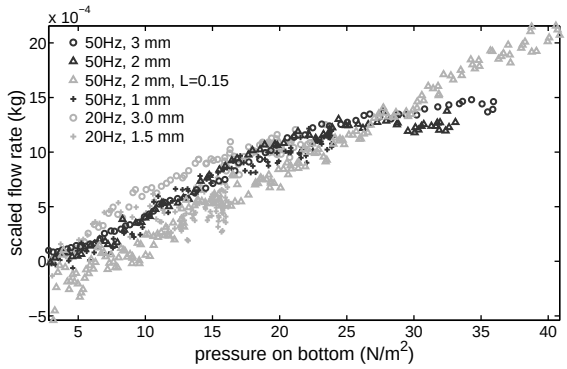


*Figure 7.9: Scaled flow rates plotted as a function of the pressure on the bottom. The restitution and friction coefficients are, respectively, 0.9 and 0.5.*

# References

[1] Hector Pacheco-Martinez, Henk Jan van Gerner, and J. C. Ruiz-Suárez, *Storage and discharge of a granular fluid*, Phys. Rev. E **77**, 021303 (2008)

[2] H. A. Janssen, *Versuche uber Getreidedruck in Silozellen*, Z. Ver Dtsch. Ing. **39**, 1045 (1895).

[3] I. Zuriguel, L.A. Pugnaloni, A. Garcimartin, and D. Maza, *Jamming during the discharge of grains from a silo described as a percolating transition*, Phys. Rev. E **68**, 030301(R) (2003).

[4] I. Zuriguel, A. Garcimartin, D. Maza, L.A. Pugnaloni, and J. M. Pastor, *Jamming during the discharge of granular matter from a silo*, Phys. Rev. E **71**, 051303 (2005).

[5] L. Vanel, P. Claudin, J. P. Bouchaud, M. E. Cates, E. Clément, and J. P. Wittmer, *Stresses in Silos: Comparison Between Theoretical Models and New Experiments*, Phys. Rev. Lett. **84**, 1439 (2000).

[6] Y. Bertho, F. Giorgiutti-Dauphine, and J. P. Hulin, *Dynamical Janssen Effect on Granular Packing with Moving Walls*, Phys. Rev. Lett. **90**, 144301 (2003).

[7] R. M. Nedderman, U. Tuzun, S. B. Savage, and G. T. Houlsby, *The flow of granular materials, I. Discharge rates from hoppers*, Chem. Eng. Sci. **37**, 1597 (1982).

[8] W.A. Beverloo, H.A. Leniger, and J. Van de Velde, *The flow of granular material through orifices*, Chem. Eng. Sci. **15**, 260 (1961).

[9] D. Ertas and T. C. Halsey, *Granular gravitational collapse and chute flow*, Europhys. Lett. **60**, 931 (2002).

[10] M. L. Hunt, R. C. Weathers, A. T. Lee, C. E. Brennen, and C. R. Wassgren, it Effects of horizontal vibration on hopper flows of granular materials, Phys. Fluids **11**, 68 (1999).

[11] C. R. Wassgren, M. L. Hunt, P. J. Freese, J. Palamara, and C. E. Brennen, it Effects of vertical vibration on hopper flows of granular material, Phys. Fluids **14**, 3439 (2002).

[12] K. Chen, M. B. Stone, R. Barry, M. Lohr, W. McConville, K. Klein, B. L. Sheu, A. J. Morss, T. Scheidemantel, and P. Schiffer, *Flux through a hole from a shaken granular medium*, Phys. Rev. E **74**, 011306 (2006).

[13] C. T. Veje and P. Dimon, *The dynamics of granular flow in an hourglass*, Granular Matter **3**, 151 (2004).

[14] D. A. Huerta, V. Sosa, M. C. Vargas, and J. C. Ruiz-Suarez,*Archimedes' principle in fluidized granular systems*, Phys. Rev. E **72**, 031307 (2005).

[15] J. B. Knight, H. M. Jaeger, and S. R. Nagel, *Vibration-induced size separation in granular media: The convection connection*, Phys. Rev. Lett. **70**, 3728 (1993).

[16] M. E. Mobius, X. Cheng, G. S. Karczmar, S. R. Nagel, and H. M Jaeger, *Intruders in the Dust: Air-Driven Granular Size Separation*, Phys. Rev. Lett. **93**, 198001 (2004).

[17] Y. Nahmad-Molinari, G. Canul-Chay, and J. C. Ruiz-Suarez, *Inertia in the Brazil nut problem*, Phys. Rev. E **68**, 041301 (2003).

[18] B. J. Crewdson, A. L. Ormond, and R. M. Nedderman, *Air-impeded discharge of fine particles from a hopper*, Powder Technol. **21**, 245 (1977).

[19] D. Hirshfeld, Y. Radzyner and D. C. Rapaport, *Molecular dynamics studies of granular flow through an aperture*, Phys. Rev. E **56**, 4404 (1997).

[20] D. Hirshfeld, D. C. Rapaport, *Granular flow from a silo: Discrete-particle simulations in three dimensions*, Eur. Phys. J. E **4**, 193 (2001).

[21] M.A. van der Hoef, M. Ye, M. van Sint Annaland, A.T. Andrews IV, S. Sundaresan, and J.A.M. Kuipers, *Multi-Scale Modeling of Gas-Fluidized Beds*, Adv. Chem. Eng. **31**, 65 (2006).

[22] See EPAPS Document No. E-PLEEE8-77-116802 for a video of the simulations with walls vibrating at 20 and 50 Hz. For more information on EPAPs, see http://www.aip.org/pubservs/epaps.html.

# 8

# General conclusion and outlook

The main theme of this thesis has been the influence of the interstitial air on the behavior of granular matter, which for relatively small particles can be very pronounced. We have focused on two examples that illustrate this in a particularly clear manner:

- *Faraday Heaping* - The formation of Faraday heaps on a vibrating plate is caused by a subtle interplay between the Stokesian forces (drag, air pressure) and the Newtonian forces (from collisions and gravity). The former drive the particles toward the center of the heap while the latter drive the particles outward. The slope angle of a stable heap is determined by the balance between the opposite particle fluxes from the Stokesian and Newtonian forces. Also the coarsening of a landscape of many small heaps into one large heap was shown to be a result of these two types of forces.
- *Chladni patterning* - When particles are sprinkled on a resonating plate, the Newtonian forces will drive relatively large particles to the nodal lines, giving rise to the famous Chladni patterns, whereas very fine particles are driven to the anti-nodes by the Stokesian forces. We have made a detailed study of the air currents that drive these fine particles. We also found a novel phenomenon: When the acceleration of the resonating plate is below $g$, particles will always move to the anti-nodes, irrespective of their size or weight, since in this case both the Stokesian *and* the Newtonian forces are directed toward the anti-nodes.

The numerical code has also been used to investigate the discharge of a granular fluid through an orifice of a container. We found that when the walls of the container are vibrated very strongly, the granular bed discharges similar to a normal fluid i.e., the outflow velocity grows with the height of the column.

Apart from the aforementioned examples, there are also many other phenomena where the interstitial air plays an important role and which could be investigated by the numerical model described in this thesis. Two phenomena of particular interest for future research are:

*The granular jet* - A large intruder impacting on a bed of fine sand particles results in a surprisingly vigorous jet which shoots up from the surface of the sand [1]. Recently, it was shown in experiments that the height of the jet and the penetration depth of the intruder strongly depend on the ambient air pressure [2, 3].

*The Brazil nut effect* - When a bed of granular particles containing a large intruder (the "Brazil nut") is shaken, the intruder ends up on the surface. It has been shown experimentally that the rise velocity of the intruder depends on the presence of air [4, 5]. The interstitial air can even cause an intruder to sink that would otherwise rise [6].

In both these proposed examples, the interaction of the large intruder with the air can be calculated by the immersed boundary correction method, while the interaction of the small particles with the air is handled via (empirical) drag relations. The typical number of particles in a granular jet experiment ($\approx 10^9$) is however about 500 times larger than what is currently feasible in our numerical simulations. This problem could be solved by implementing an axisymmetric version of the numerical code, which is relative straightforward. Another remedy would be to use larger particles together with an increased viscosity in the simulation, in order to maintain the same ratio between the air drag and gravity forces as in the experiments. Recently, a parallelized version of the numerical model has been implemented within our research group, which will enable us to investigate larger systems in less time.

In the phenomena discussed above, the Newtonian and Stokesian forces compete for dominance. Other forces - such as electrostatic forces [7], capillary forces in the presence of a liquid [8] and, for much smaller particles, Van der Waals forces [9, 10] - do not seem to play a crucial role. In the experiments described in this thesis, we actually have done our best to minimize the influence of these force by applying an anti-electrostatic spray on the particles and drying them before use. The next step in granular research however, would be to take also these forces into account, experimentally *and* in the numerical model [7, 11]. The few studies that have been performed in this direction (for instance coarsening in electrostatically driven granular media [7]) show that this is a very promising field for future work.

# References

[1] D. Lohse, R. Bergmann, R. Mikkelsen, C. Zeilstra, D. van der Meer, M. Versluis, K. van der Weele, M. van der Hoef, and H. Kuipers, *Impact on Soft Sand: Void Collapse and Jet Formation*, Phys. Rev. Lett. **93**, 198003 (2004).

[2] J. R. Royer, E. I. Corwin, P. J. Eng, and H. M. Jaeger, *Gas-Mediated Impact Dynamics in Fine-Grained Granular Materials*, Phys. Rev. Lett. **99**, 038003 (2007).

[3] G. Caballero, R. Bergmann, D. van der Meer, A. Prosperetti, and D. Lohse, *Role of Air in Granular Jet Formation*, Phys. Rev. Lett. **99**, 018001 (2007).

[4] M.E. Möbius, B.E. Lauderdale, S.R. Nagel, H.M. Jaeger, *Size separation of granular particles*, Nature **414**, p. 270 (2001).

[5] M.A. Naylor, M.R. Swift, and P.J. King, *Air-driven Brazil nut effect*, Phys. Rev. E **68**, 012301 (2003).

[6] M.E. Möbius, X. Cheng, P. Eshuis, G. S. Karczmar, S.R. Nagel, and H. M. Jaeger, *Effect of air on granular size separation in a vibrated granular bed*, Phys. Rev. E **72**, 011304 (2005).

[7] I.S. Aranson, D. Blair, V.A. Kalatsky, G.W. Crabtree, W.-K. Kwok, V.M. Vinokur, and U. Welp, *Electrostatically Driven Granular Media: Phase Transitions and Coarsening*, Phys. Rev. Lett. **84**, 3306 (2000).

[8] S. Herminghaus, *Dynamics of wet granular matter*, Adv. Phys. **54**, 221 (2005).

[9] J.D. van der Waals, *Over de continuiteit van den gas- en vloeistoftoestand*, Ph.D. Thesis, Leiden University (1873).

[10] H.C. Hamaker, *The London-van der Waals attraction between spherical particles*, Physica (Amsterdam) **4**, 1058 (1937).

[11] M. Schulz, B.M. Schulz, and S. Herminghaus, *Shear-induced solid-fluid transition in a wet granular medium*, Phys. Rev. E **67**, 052301 (2003).

# Summary

Granular materials can be encountered everywhere: In everyday life for example as sand, sugar, and rice, or in natural processes such as avalanching and desert formation. Also in industry granular materials are abundant, since most raw materials are supplied in the form of grains, and a thorough understanding of granular matter is essential in order to efficiently handle these materials. Most papers on the subject have dealt almost exclusively with systems in which the effect of the ambient air is ignored, assuming that the motion of the particles is governed by gravity and mechanical contact forces only. While this is a valid approximation when the particles are large (diameter $\gtrsim$ 1 mm), for smaller particles the air actually has a pronounced influence and must be taken into account. In this thesis we focus on particles of intermediate size, where the "Stokesian" forces (drag, air pressure) and the "Newtonian" forces (from collisions and gravity) compete for dominance.

Numerical simulations can play an important role in studying the interplay between the grains and the interstitial air, since they can provide data that is not always accessible in experiments and the different parameters are easier to control. In this thesis, a numerical model to calculate the motion of all individual particles in the granular material is used, together with a model for the calculation of the interstitial air. The interaction between small particles and the air is handled via (empirical) drag relations. The interaction of the air with large objects, such as a wall or a large sphere, is implemented via the cell cut method and the immersed boundary method.

The numerical model is used to simulate the motion of particles on a vibrating *rigid* plate, generating the famous Faraday heaps known from experiment. A detailed analysis shows that the particles are dragged towards the center of the heap by the airflow through the bed (i.e., the Stokesian forces) during the phase when the gap between bed and vibrating bottom is growing, and avalanche down on the surface (due the Newtonian forces) after the heap comes down on the vibrating plate again. The heap angle is determined by the balance of the constructive Stokesian and destructive Newtonian forces. Importantly, the simulations also explain the experimentally observed coarsening of a number of small heaps into larger heaps.

The insight obtained by the simulations is used to develop a mathematical description for the coarsening behavior, which captures the essential features of this complicated process in two differential equations. The results of the mathematical description are in excellent agreement

not only with simulations, but also with experiments performed in our lab. We deduce from the mathematical description that the average life time of a $N-$heap state scales as $N^{-3}$ in one dimension, and as $N^{-2}$ in two dimensions.

Next, we turn to another prime example of the interplay of granular matter with the ambient air: A classic way of visualizing two-dimensional standing waves is by sprinkling coarse particles (sand) on a horizontal plate and bringing it into resonance by e.g. a violin bow. Relative large particles will move to the nodal lines, giving rise to the famous Chladni patterns (a standard high school demonstration experiment), whereas very fine particles will move to the anti-nodes. This was already noted by Chladni himself, who observed that tiny hair shavings from his violin bow were carried to the anti-nodes. The motion of the particles on the vibrating *flexible* plate is simulated, and we are able to reproduce both the standard and inverse Chladni patterns. It is shown that the fine particles move to the anti-nodes due to air currents induced by the vibrating plate.

Air currents are however not the only mechanism leading to inverse patterns: We show - theoretically and numerically - that when the acceleration of the resonating plate is below $g$, particles will always move to the anti-nodes, irrespective of their size or weight. We also explain why this effect has hitherto escaped detection in standard Chladni experiments. Summarizing, for very fine particles, the Stokesian forces dominate and inverse Chladni patterns are formed, while for coarse particles, the Newtonian forces dominate and can create either regular or inverse patterns, depending on the shaking strength.

Finally, the discharge of a granular fluid through an orifice, such as one finds for instance in a grain silo, is investigated. With static walls, the outflow velocity is known to be independent of the height of the granular column. It was believed that this was due to the fact that part of the granular mass is carried by the walls instead of the bottom plate of the silo. We show however that even when the walls are vibrated horizontally in a experiment, and the weight is fully carried by the bottom plate, the outflow velocity remains independent of the height of the granular column. Only when the walls are vibrated very strongly, the granular bed indeed discharges similar to a normal fluid i.e., the outflow velocity grows with the height of the column.

In conclusion, we have shown that for particles of intermediate size, the Stokesian and the Newtonian forces compete for dominance, which leads to interesting phenomena like Faraday heaping and Chladni patterning. The numerical model described in this thesis can also be used to

simulate other phenomena where the interstitial air plays an important role (such as the granular jet or the Brazil nut effect) and, with appropriate modifications, to study systems where also electrostatic or capillary forces join the Newtonian and Stokesian forces.

# Samenvatting

Granulaire materie is overal: we komen het tegen in ons dagelijks leven – in de vorm van zand, suiker of rijst – en in natuurlijke processen zoals lawines en woestijnvorming. Ook in de industrie speelt granulaire materie een belangrijke rol, aangezien veel grondstoffen worden aangeleverd in granulaire vorm. Voor een efficiënte verwerking van deze grondstoffen is een diepgaand begrip van granulaire materie onontbeerlijk. In het merendeel van de studies die tot dusverre zijn verschenen, wordt de invloed van de omringende lucht op de deeltjes verwaarloosd en beperkt men zich tot de zwaartekracht en de contactkrachten tussen de deeltjes onderling. Dit is een redelijke benadering indien de deeltjes voldoende groot zijn (diameter $\gtrsim$ 1 mm), maar voor kleinere deeltjes is de invloed van de lucht beslist niet verwaarloosbaar. In dit proefschrift richten we ons op deze kleinere deeltjes, waarvoor zowel de "Newtoniaanse" krachten (geleverd door botsingen en zwaartekracht) en de "Stokesiaanse" krachten (geleverd door de lucht) een belangrijke rol spelen. Zoals de titel van het proefschrift reeds aangeeft, concentreren we ons met name op systemen waarin de Newtoniaanse en Stokesiaanse krachten elkaar tegenwerken. Dit geeft niet alleen een interessante strijd om de hegemonie te zien, maar stelt ons bovendien in staat om de diverse effecten die bijdragen aan de beweging van de deeltjes goed van elkaar te onderscheiden.

Numerieke simulaties spelen een belangrijke rol in de bestudering van granulaire materie. Ze leveren informatie die niet eenvoudig (of vaak zelfs helemaal niet) verkregen kan worden via experimenten, zoals bijvoorbeeld de precieze positie en snelheid van elk deeltje. Bovendien zijn de verschillende parameters – zoals de mate van inelasticiteit van de botsingen of de luchtdruk – in te stellen op iedere gewenste waarde, hetgeen in experimenten uiteraard veel problematischer is. In dit proefschrift gebruiken we een numeriek model dat de beweging van alle individuele deeltjes berekent in samenspel met de stroming van de lucht. De interactie tussen kleine deeltjes en de lucht wordt berekend met behulp van (empirische) relaties voor de luchtweerstand. De interactie van de lucht met grotere voorwerpen – zoals een wand of een bal die zich te midden van de kleine deeltjes bevindt – wordt berekend via ofwel de 'cell cut' methode, ofwel de 'immersed boundary' methode.

Het eerste systeem dat we bestuderen is een granulair bed (met een dikte van enkele tientallen deeltjesdiameters) in een verticaal trillende bak. De amplitude en frequentie van de opgelegde trilling zijn zodanig gekozen dat het oorspronkelijk vlakke oppervlak van het bed spontaan

vervormt tot een landschap van kleine heuveltjes. Dit zijn de befaamde 'Faraday heaps', genoemd naar Michael Faraday die het verschijnsel in 1831 als eerste waarnam. Een nauwkeurige analyse met behulp van het numerieke model toont aan dat de deeltjes in het binnenste van het bed naar het centrum van de heaps worden gestuwd door de luchtstroming die ontstaat wanneer het bed loskomt van de trillende bodem. Als het bed vervolgens weer landt, vinden er kleine lawines langs de hellingen van de heuvels plaats. De hellingshoek van de heaps wordt bepaald door het evenwicht tussen de constructieve stuwing van de lucht (de Stokesiaanse krachten) en de destructieve lawines (de Newtoniaanse krachten).

In onze numerieke simulaties zien we ook dat de kleine heaps in de loop van de tijd naar elkaar toe bewegen, samensmelten en grotere heaps vormen, totdat uiteindelijk één enkele heap overblijft. Dit proces ('coarsening' geheten) was reeds bekend uit experimenten, maar tot nu toe slechts onvolledig begrepen. Dankzij het gedetailleerde beeld dat de simulaties ons verschaffen, zijn we in staat een wiskundig model voor het coarsening proces op te stellen, waarvan de resultaten uitstekend overeenkomen met experimenten uitgevoerd in ons laboratorium. Eén van de meest markante uitkomsten is dat de gemiddelde levensduur van een $N$-heap toestand schaalt als $N^{-3}$ in één dimensie (dat wil zeggen, indien het experiment uitgevoerd wordt in een langwerpige bak) en als $N^{-2}$ in twee dimensies (in een rechthoekige bak).

Een tweede voorbeeld waarin de Stokesiaanse en Newtoniaanse krachten in tegenovergestelde richting werken, is het klassieke experiment van Ernst Chladni uit 1787. Hierbij worden de trillingspatronen van een buigzame plaat zichtbaar gemaakt door er korreltjes op te strooien, zoals zand of maanzaad, en vervolgens de plaat te exciteren met bijvoorbeeld de strijkstok van een viool (zoals Chladni het zelf deed). Relatief grote deeltjes (waarvoor de Newtoniaanse krachten de boventoon voeren) verzamelen zich op de knooplijnen van de plaat, resulterend in de bekende Chladni-patronen. Kleinere deeltjes (die vatbaarder zijn voor de Stokesiaanse krachten) bewegen juist naar de buiken toe. Chladni had dit laatste ook reeds opgemerkt, zij het slechts als curiositeit, voor de minuscule haartjes afkomstig van zijn strijkstok. In onze numerieke simulaties zijn we erin geslaagd zowel de standaard- als de inverse patronen te reproduceren. Hierbij hebben we speciale aandacht besteed aan de luchtstromingen die worden opgewekt boven de resonerende plaat, en de wijze waarop deze aanleiding geven tot de vorming van de inverse Chladni-patronen.

De luchtstroming blijkt echter niet het enige mechanisme te zijn

dat tot de inverse patronen kan leiden: we tonen aan – theoretisch en numeriek – dat wanneer de versnelling van de plaat kleiner is dan de zwaartekrachtsversnelling $g$, de deeltjes altijd naar de buiken toe bewegen, ongeacht hun grootte of gewicht. Tevens verklaren we waarom dit fenomeen nooit is opgemerkt in de standaarduitvoering van het Chladni-experiment.

Tenslotte onderzoeken we de uitstroom van een granulaire vloeistof uit een container, zoals bijvoorbeeld een graansilo. Het is bekend dat de uitstroomsnelheid, indien de wanden van de container gewoon stilstaan, onafhankelijk is van de hoogte van de granulaire kolom. Algemeen werd aangenomen dat dit terug te voeren is op het feit dat een aanzienlijk deel van het gewicht van de kolom niet door de bodem van de silo gedragen wordt, maar door de wanden. Wij laten echter zien dat wanneer de wanden in horizontale trilling gebracht worden (waardoor het gewicht wel volledig door de bodem wordt gedragen) de uitstroomsnelheid nog steeds onafhankelijk is van de hoogte van de granulaire kolom. Pas wanneer de opgelegde trilling van de wanden bijzonder heftig wordt, begint de granulaire materie zich als een gewone vloeistof te gedragen, dat wil zeggen, de uitstroomsnelheid wordt dan afhankelijk van de hoogte van de kolom.

In dit proefschrift hebben we laten zien dat deeltjes met een diameter kleiner dan 1.0 mm, waarvoor de Stokesiaanse en Newtoniaanse krachten strijden om de hegemonie, interessante verschijnselen vertonen zoals de formatie van Faraday heaps en inverse Chladni patronen. De numerieke code heeft bewezen een accurate beschrijving te geven van de invloed van de lucht op granulaire materie en is daarom bij uitstek geschikt voor het simuleren van tal van verschijnselen waarin de omringende lucht een rol speelt. Naast de reeds beschreven voorbeelden valt hierbij te denken aan onder meer het 'Brazil nut effect' of de 'granulaire jet'. Het is te voorzien dat dezelfde code, met enkele aanpassingen, in de toekomst ook nuttig ingezet zal kunnen worden bij het bestuderen van systemen waarvoor naast de Newtoniaanse en Stokesiaanse krachten, ook de elektrostatische, capillaire en Van der Waals krachten een rol van betekenis spelen.

# Dankwoord

Vier jaar lijkt een lange tijd voor het schrijven van een proefschrift, maar deze jaren zijn werkelijk voorbij gevlogen. Ik heb erg veel plezier gehad, zowel van het onderzoek als van de gezelligheid in de twee groepen waarin ik heb gepromoveerd. Veel mensen hebben hier aan bijgedragen (aan het onderzoek of gezelligheid, maar vaak ook aan allebei) en een aantal mensen wil ik met name noemen.

Detlef en Hans, allereerst wil ik jullie bedanken voor de gelegenheid die jullie mij hebben gegeven om bij de Physics of Fluids (PoF) groep en de Fundamentals of Chemical Reaction Engineering (FCRE) groep te promoveren. Het was erg inspirerend om in deze groepen te werken en ik heb erg veel bewondering voor jullie kennis en inzicht.

Ko, Martin en Devaraj, betere begeleiders kan een promovendus zich niet wensen. Ko, ook na je vertrek naar Griekenland in 2006 hebben we nog veel samengewerkt en daar ben ik erg blij mee. Ik kon je altijd bellen, ook 's avonds of in het weekend, en vooral in de laatste maanden van mijn promotie heb ik daar vaak gebruik van gemaakt. Martin, bij jou ben ik toch wel het vaakst binnengewandeld, zowel voor de gezelligheid als nieuwe inspiratie en motivatie. Devaraj, je theoretisch inzicht is erg groot en vooral bij het tot stand komen van het coarsening model was deze onmisbaar.

Ik heb mijn promotie uitgevoerd in twee groepen en ik wil dan ook iedereen in deze twee groepen bedanken voor de leuke tijd. Ik heb genoten van de vele groepsuitjes, flesjesavonden, lunchwandelingen, borrels etc. In het bijzonder wil ik mijn (ex-)kamergenoten Ramon, Sander, Marlies, Hanneke, Alvaro en Laura bedanken voor de leuke tijd en vele gesprekken. Eigenlijk hadden we het over van alles: soms over persoonlijke of serieuze zaken, maar vaak ook over redelijk nutteloze onderwerpen waarvan ik tot vier jaar geleden dacht dat deze alleen mij interesseren. Ik zal jullie gezelschap zeker missen. Peter, bedankt voor het wielrennen, het Noaberschap en ik vond het erg leuk dat ik je paranymf mocht zijn.

Joanita en Nicole, bedankt voor jullie hulp met administratieve zaken. Gert-Wim, Martin en Gerrit, bedankt voor het maken van de diverse experimentele opstellingen. Bas, je hebt heel wat werk gehad om mijn laptop aan de praat te houden, maar gelukkig is door mijn computer (en die van Hanneke) snel duidelijk geworden dat dit merk niet de beste keus is.

Gabriel, I had a great time working with you. Thanks to you, we have beautiful experiments of the Faraday heaps. I'm still very sorry that I had

to miss your wedding in Mexico.

I would like to thank the co-authors of Chapter 7, Carlos Ruiz and Hector Adrian Pacheco. Carlos, your visit to the University of Twente and your talk “Fluidized Granular Matter: Archimedes but not Torricelli” led to our collaboration, an article in PRE, and off course, Chapter 7 in this thesis.

Mijn Paranimfen Erik-Jan en Marlies wil ik nog in het bijzonder noemen. Erik-Jan, sinds onze studietijd ben jij een van mijn beste vrienden. Je was eigenlijk vanzelfsprekend de ceremoniemeester bij mijn bruiloft en nu dus ook bij deze promotie. Marlies, ik vond het erg leuk om jou als kamergenoot te hebben. De gezelligheid in ons kantoor was niet altijd bevorderlijk voor de productiviteit, maar gelukkig is mijn proefschrift toch nog afgekomen.

Verder wil ik mijn familie bedanken, die me op de achtergrond altijd heeft gesteund. Pap en mam, door jullie heb ik mij zelf kunnen ontwikkelen en ben ik geworden wie ik ben. Hiervoor ben ik jullie erg dankbaar.

Als laatste wil ik mijn gezin bedanken. Ingrid, ik ben je erg dankbaar dat je het goed vond om naar het verre oosten te verhuizen, maar vooral voor alle steun, vertrouwen en liefde die ik van jou gekregen heb. De indrukwekkendste gebeurtenissen van de afgelopen 4 jaar zijn toch wel de geboortes van onze twee schitterende dochters, Nathalie en Mireille. Lieve Nathalie en Mireille, jullie hebben niet een directe bijdrage aan mijn proefschrift geleverd en waarschijnlijk had ik zonder jullie meer tijd aan conferenties en onderzoek besteed, maar jullie maken me erg gelukkig en dat is denk ik ook belangrijk voor het goed afronden van een promotie. Ik heb genoten de afgelopen vier jaar en nu kijk ik uit naar onze toekomst in Zwolle!

*Henk Jan van Gerner*
*Maart 2009*

# About the author

Henk Jan van Gerner was born on July 2nd, 1977 in Harderwijk, The Netherlands. He graduated from high school 'Christelijk College Nassau Veluwe' in Harderwijk in 1995, and started that same year studying Mechanical Engineering at the University of Twente in Enschede. His studies included a six-month traineeship at Urenco Nederland in 2000. In 2001, he graduated on a numerical study of condensing rotating flow in the Engineering Fluid Dynamics group.

After his study, he worked at TNO CMC (Center for Maritime Constructions) in Delft. In January 2005 he returned to the University of Twente as a PhD student in the Physics of Fluids group and the Fundamentals of Chemical Reaction Engineering group (both belonging to the Faculty of Science and Technology), to work on the project 'Newton vs Stokes: Competing forces in granular matter'. The results of the PhD research are described in this thesis. As from March 2009, he works at NLR (National Aerospace Laboratory) in Flevoland, The Netherlands.